UNIVERSITÀ DELLA CALABRIA

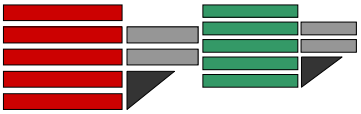

Dipartimento di FISICA

Facoltà di Scienze Matematiche Fisiche e Naturali

Dottorato di Ricerca in Fisica
XVII Ciclo
(Settore Disciplinare FIS/04)

The ATLAS Experiment: Ageing Studies on the Drift Tubes of the Muon Spectrometer and Observability of MSSM Heavy Higgses via a Sparticle Decay Mode

Dott.*ssa* Cristina Adorisio

Supervisor:
Prof. **Giancarlo Susinno**

PhD Coordinator:
Prof. **Gennaro Chiarello**

Anno Accademico 2005

Contents

Introduction

"Do not worry about your
difficulties in mathematics;
I can assure you that
mine are still greater".
Albert Einstein

This Ph.D. thesis summarized the work performed in INFN Cosenza group within the ATLAS Muon Collaboration. This work is a representative cross section of the different aspects to the preparation of a modern day high energy physics experiment. An important part is dedicated to the testing of specialized detector elements. And the experiment's discovery potential for signatures of new theoretical proposal is evaluated.

The thesis is divided into three parts. The first part, made up of the first three chapters, is an introduction about the theoretical and the experimental background of the two main work I have performed during the doctoral period. The second part, the fourth chapter, is about the main work I have dealt with, the ageing problem of the Monitored Drift Tube detectors, which make up the Muon Spectrometer. And the last third part, the fifth chapter, is about the study of an MSSM Higgs bosons decay mode into sparticles.

In **Chapter 1** the Standard Model theory is reviewed, its successes and also its faults are briefly discussed and the Supersymmetric theory is introduced as the possible solution to the Standard Model problems. The Minimal Supersymmetric Standard Model (MSSM) is then introduced as the minimal supersymmetric extension of the SM.

In **Chapter 2** I will give a brief description of the Large Hadron Collider project, which is actually under construction at CERN ('Centre Européen pour la Recherche Nucléaire'). An overview of the physics and of the experiments at the LHC is reported. The ATLAS detector is also overviewed and its physics programme is briefly discussed.

Chapter 3 deals with the Monitored Drift Tubes, which make up the Muon Spectrometer. Firstly the Muon Spectrometer system is described. Then the principle of operation of the MDT is discussed. Finally the ATLAS background conditions are taken into account as the main reason to perform ageing studies on the drift tube chambers.

Recently, some preliminary studies have shown that exists the possibility of a premature ageing, due to presence of pollutants in the MDT gas system. An ageing test, performed in 2001-2003, had shown a loss in the performance of a MDT chamber, operated under high irradiation conditions with a prototype of the ATLAS gas recirculation system. In **Chapter 4** the results of this test are briefly reported as a starting point for the ageing test performed in 2004-2005 in a more systematic way to investigate this ageing problem. The goal of the test was to check the behavior of the MDT chambers after an irradiation similar to a few years of operation at LHC, and to define the requirements for the ATLAS gas system components.

Chapter 5 deals with the study of the decay of the heavy neutral MSSM Higgs bosons into a pair of next-to-lightest neutralinos. At first it is introduced the region of the MSSM parameter space in which the study is performed. Then the analysis strategy is worked out looking to the generated Higgs signal characteristics and studying the backgrounds. The Higgs Signal observability for a little region of the MSSM parameter space is reported.

Part I

THEORETICAL AND EXPERIMENTAL BACKGROUND

Chapter 1

The Standard Model and Beyond It

This chapter aims to give a short introduction to the present understanding of particle physics, with a brief review of the status of the Standard Model (SM). Then the Minimal Supersymmetric extension of the Standard Model (MSSM) will be introduced and it will be explained how the MSSM can solve many of the defects of the Standard Model.

1.1 The Successes and Failures of the Standard Model

The Standard Model is the current theory of fundamental particles and how they interact. In the last half century an immense amount of theoretical and experimental work has been carried out in order to reveal the ultimate constituents of matter and to establish an accurate description of their interaction. This effort has let to a fundamental theory based on symmetry principles, containing only a limited set of elementary particles. This theory is called ***Standard Model*** (SM). Its predictions are in agreement with all experimental data of the last decades, except for the now experimentally established non-zero values of some of the neutrino masses [1], [2].

The Standard Model is the quantum theory that includes the theory of strong interactions, the quantum cromodynamics QCD, and the unified theory of weak and electromagnetic interactions, the electroweak theory. At present, the Standard Model does not include the effects of gravitational interactions.

According to the present knowledge all matter in the Universe is made of two kinds of elementary spin-1/2 particles (*fermions*), quarks and leptons, interacting through fields. The matter particles consist of six types (or *flavours*) of leptons and six types (or *flavours*) of quarks.

All these elementary fermions can be grouped into three *families* or *generations* of two quarks and two leptons each. They can be represented as columns of a 2×3 matrix:

$$\begin{pmatrix} \nu_e & \nu_\mu & \nu_\tau \\ e & \mu & \tau \end{pmatrix}, \qquad \begin{pmatrix} u & c & t \\ d & s & b \end{pmatrix} \tag{1.1}$$

Neutrinos, in the top row of the lepton matrix, are electrically neutral and very light particles.

The three lepton have different masses and +1 charge.

The quarks in the top row of the second matrix have +2/3 charge, the other ones have -1/3 charge; their mass increase from the u to the t quark. The two members of every family differ by one unit of electric charge. The fermions are listed in table 1.1.

Leptons	mass	Quarks	mass
$\begin{pmatrix} \nu_e \\ e \end{pmatrix}$	< 3 eV/c^2 0.511 MeV/c^2	$\begin{pmatrix} u \\ d \end{pmatrix}$	$1.5 - 4.5$ MeV/c^2 $5 - 8.5$ MeV/c^2
$\begin{pmatrix} \nu_\mu \\ \mu \end{pmatrix}$	< 0.19 MeV/c^2 105.66 GeV/c^2	$\begin{pmatrix} c \\ s \end{pmatrix}$	$1 - 1.4$ GeV/c^2 $80 - 155$ MeV/c^2
$\begin{pmatrix} \nu_\tau \\ \tau \end{pmatrix}$	< 18.2 MeV/c^2 1.777 GeV/c^2	$\begin{pmatrix} t \\ b \end{pmatrix}$	174.3 GeV/c^2 $4.0 - 4.5$ GeV/c^2

Table 1.1: *Experimentally measured masses of fermions, as reported in the Review of Particle Physics (2004) [3].*

Besides electric charge, the quarks also possess another kind of charge called *colour charge*. This is relevant for their strong interaction, which binds them together inside nuclear particles (hadrons). All stable matter is built from the first generation of massive fermions (u, d, e).

Four types of interaction field have been distinguished in Nature:

• the **electromagnetic interaction** between electrically charged particles, described by quantum electrodynamics QED in very good agreement with experiments. The mediator of this interaction is a massless particle, the *photon*;

• the **weak interaction**, mediated by the three massive boson W^+, W^- and Z^0, acts on all the constituents of matter. The W- and Z-bosons have a mass of 80.2 GeV and 91.2 GeV respectively;

• the **strong interaction** takes place between quarks which make up hadrons. The mediators are 8 massless gluons. In the theory of the strong force, the QCD, there are six different types of strong charge, called *color*, three associated to quarks and the other three to the anti-quarks;

• the **gravitational interaction** couples to the mass of the particles. The gravitational forces is normally negligible in sub-atomic processes since the masses of the elementary particles are very far below the scale where gravity would became appreciable.

The particles associated with those fields are spin-1 particles which mediate forces called *gauge bosons* (with the exception of gravity which is mediated by a spin-2 graviton). The gauge bosons are listed in table 1.2.

So, the quanta of the electromagnetic interaction between electrically charged particles are

boson	interaction	mass	q
Vector Boson			
W^+	Weak	80.423 ± 0.039 GeV/c^2	+1
W^-	Weak	80.423 ± 0.039 GeV/c^2	-1
Z^0	Weak	91.1876 ± 0.0021 GeV/c^2	0
γ	QED	0	0
g	QCD	0	0
Scalar Boson			
H	Yukawa	> 114.4 GeV/c^2 95% CL	0

Table 1.2: *Experimentally measured masses of SM bosons, as reported in the Review of Particle Physics (2004) [3]. The last columns report the quantum numbers of these particles.*

the massless photons (γ); since they are massless, the range of electromagnetic interaction is infinite. The quanta of the weak interaction fields between fermion are charged $W^{\pm}$ bosons and the neutral Z boson; they are massive ($\sim 100\ GeV$) and therefore the weak interaction is short ranged (R $\sim 10^{-17} cm$). The quanta of the strong interaction field which acts between colour-charged quarks are the gluons (g) and have zero mass; thus, like photon, they might be expected to have infinite range, however gluons, unlike photons, themselves carry a colour-charge and interact among each other; this leads to a phenomenon called *confinement* which restricts the strong force to nuclear distance (R $\sim 10^{-13} cm$).

1.1.1 The Electroweak Theory

In 1960's the electromagnetic and the weak interaction were combined into a single theory which is know as GSW model, after its founders Glashow, Salam and Weinberg, or as *electroweak unification* [4], [5]. That the two interaction cannot be treated as separate $U(1)$ and $SU(2)$ gauge theories can be understood from the fact that the two leptons in the $SU(2)$ doublet, the electron and the neutrino, carry different electrical charge. In the electroweak sector of the Standard Model left-handed particles are arranged in $SU(2)$ doublets while right-handed particles are $SU(2)$ singlets. The weak interaction acts only on the left handed doublets; the electromagnetic interaction acts on both the left- and right-handed components. The first generation leptons can thus be written as:

$$\begin{pmatrix} \nu_{eL} \\ e_L \end{pmatrix}, \quad e_R \tag{1.2}$$

with quantum numbers $(T_3, Y) = (\pm\frac{1}{2}, -\frac{1}{2})$ and $(0, -1)$. T_3 is the third component of the *weak isospin* and Y is the weak *hypercharge*. The right-handed component of the neutrino does not exist in the Standard Model. The left- and right-handed components of the first

generation of quarks can be written as:

$$\left(\begin{array}{c} u_L \\ d_L \end{array} \right), \quad u_R, \quad d_R \tag{1.3}$$

with quantum numbers $(T_3, Y) = (\pm\frac{1}{2}, \frac{1}{6})$, $(0, \frac{2}{3})$ and $(0, -\frac{1}{3})$.

From a mathematical point of view it is a locally gauge-invariant theory with the symmetry group $SU(2)_L \times U(1)_Y$ (L stands for *left-handed* and Y for *hypercharge*). The electromagnetic interaction is formed by combining $U(1)_Y$ with a component from $SU(2)_L$, so that the electromagnetic charge is $Q = Y + T_3$.

To reproduce experimental results on weak decays and to allow CP (Charge and Parity) violation within Standard Model, the quarks have to be mixed by a mixing matrix (Cabibbo, Kobayashi, Maskawa CKM matrix) defined by:

$$\left(\begin{array}{c} d' \\ s' \\ b' \end{array} \right) = V_{CKM} \left(\begin{array}{c} d \\ s \\ b \end{array} \right) = \left(\begin{array}{ccc} V_{ud} & V_{us} & V_{ub} \\ V_{cd} & V_{cs} & V_{cb} \\ V_{td} & V_{ts} & V_{tb} \end{array} \right) \left(\begin{array}{c} d \\ s \\ b \end{array} \right) \tag{1.4}$$

The Standard Model incorporates the Electroweak Theory of Glashow, Salam and Weinberg with the model of the fundamental strong force, the Quantum CromoDynamics (QCD). The complete gauge group of the Standard Model is $SU(3)_c \times SU(2)_L \times U(1)_Y$ (where the index c stands for *colour*). Although the Electroweak theory is truly a common description of electromagnetic and weak phenomena, QCD does not derive naturally from the same theory and hence it is an add-on.

1.1.2 Electroweak Symmetry Breaking

The Standard Model does not account for massive bosons and fermions as observed in Nature. The GSW model predicts the existence of four massless gauge bosons, which is in disagreement with the large Z ans W bosons masses found experimentally.

In order to allow massive particles it is necessary to break the electroweak symmetry in such a way that all successful symmetry predictions are still preserved. Moreover, in the gauge boson sector, the $W^{\pm}$ and Z bosons must acquire large masses while the photon must remain massless. This can be solved by a mechanism know as ***spontaneous symmetry breaking*** [6].

In spontaneously broken theories the Lagrangian describing the dynamics of the theory is still invariant under the gauge transformation but the ground state (*vacuum*) no longer possesses the gauge symmetry. In the Standard Model an external agent (field) is needed to break the electroweak gauge symmetry in this way. This field is called the **Higgs field**. It is a scalar field (spin = 0) with the characteristic property that its ground state energy is non-zero, *i.e.* its vacuum expectation value (VEV) is not zero.

The equations of motion of the $W^{\pm}$, Z and γ are modified by the interaction with the Higgs field as though the bosons have a mass:

$$m_W = \frac{1}{2} g v \quad , \quad m_Z = \frac{1}{2}\sqrt{g^2 + g'^2}\, v \quad , \quad m_\gamma = 0. \tag{1.5}$$

where g and g' are the $SU(2)_L$ and $U(1)_Y$ coupling constant. The values of v, g and g' can be derived from measured quantities such as the Fermi weak coupling constant G_F, the electric charge e and $\sin^2(\theta_W)$ (with θ_W the Weinberg angle). The thus obtained values of m_W and m_Z are very close (within the one-loop uncertainties) to the measured values of 80.5 GeV and 91.2 GeV, respectively. The Higgs mechanism therefore provides a remarkably simple and successful solution to the electroweak symmetry breaking problem.

Like the gauge bosons, also the fermion masses result from an interaction of the fermions with the Higgs field. However the fermion-Higgs interaction is not a direct consequence of the gauge principle. It must be more or less introduced arbitrarily using the so-called *Yukawa coupling constants*, which are free parameters of the theory.

The physical particle associated with the Higgs field after the spontaneous symmetry breaking is called the ***Higgs boson***. Its mass is given by

$$m_H = \sqrt{2\lambda}v \tag{1.6}$$

where λ is still a free parameter. The Higgs mass can therefore not be predicted by theory. So far no experimental evidence of a Higgs particle has been found.

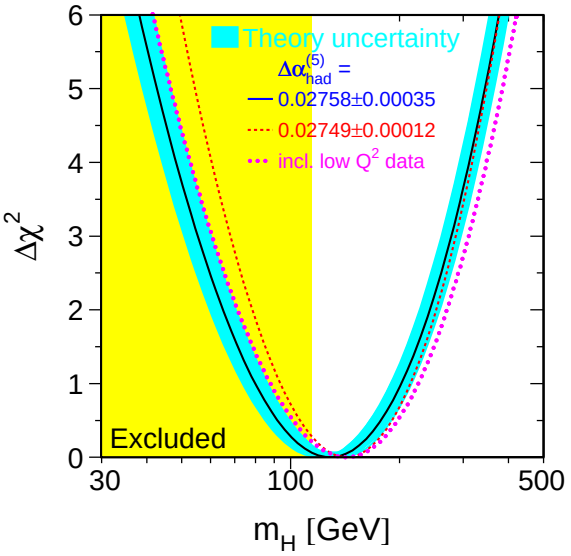

Figure 1.1: ***The Blue-Band [7].*** *Curve showing $\Delta\chi^2(m_H^2) = \chi^2_{min}(m_H^2) - \chi^2_{min}$ as a function of m_H. The line is the result of the fit using all 18 results. The associated band represents the estimate of the theoretical uncertainty due to missing higher-order corrections. The vertical shaded band shows the 95% confidence level exclusion limit on m_H of 114.4 GeV derived from the direct search of the Higgs boson at LEP-II [8]. The dashed curve is the result obtained using the theory-driven $\Delta\alpha^{(5)}_{had}(m_Z^2)$ determination. From [7].*

Figure 1.1 reports the famous *Blue-Band* plot showing the $\Delta\chi^2_{min}(M_H^2)$ distribution de-

rived from a combined fit of all the world experimental date to the SM exploiting the best knowledge of precision theoretical calculations. The plot illustrates the *indirect discovery* of the Higgs boson made via the study of *constraints* provided by theory and experiments [7]. Till the Higgs boson would be experimentally observed, the Standard Model will not be completely verified. This particle has to be searched in a mass range from 114 GeV/c^2, the limit of the direct searches at LEP-II [8], to 1 TeV/c^2, the theoretical limit imposed by the stability of the theory.

1.1.3 The Open Questions of the Standard Model

The conceptual success of the SM, like the electroweak unification, the prediction of neutral current interactions and of the properties of the weak bosons or the necessity of the charm quark, are only a part of its merits, most of which come from the overall agreement between the theory and the vast set of experimental data collected in electron-positron annihilations, hadronic collisions and neutrino interactions, often measured at an accuracy level better than one part per mille.
The present status of this good agreement is shown in Figure 1.2.

Although the Standard Model describes with a remarkable precision almost all known phenomena in high energy physics, most physicists are convinced that it is merely a low energy effective theory which is part of a larger framework that will solve the remaining shortcomings of the theory. Apart from not having observed the Higgs boson, a short list of the unsatisfactory issues and drawbacks of the Standard Model should include at least the following:

1. *Too many arbitrary parameters.* The SM contains at least 18 free parameter, 3 gauge couplings, 6 quark masses and 3 lepton masses, 4 Cabibbo-Kobayashi-Maskawa free matrix elements, 2 parameters characterizing the scalar sector of the theory. The common feeling of this fact is that a more fundamental theory should be invoked to naturally explain the pattern. Unification theories start from this point.

2. *Unification of gravity to the electroweak and strong interactions.* The gravitational interaction is not included in the SM, so the theory is incomplete. A worse problem is that a unification of spin-1 gauge fields and spin-2 graviton fields within a unique algebra has been proven to be theoretically almost impossible.

3. *The dark matter problem.* Many astrophysical observations point towards the existence of non-relativistic, neutral, non-baryonic dark matter [9]. Since neutrinos are not massive enough to explain the observations, a new candidate for this cold dark matter is needed.

4. *Neutrino masses and neutrino oscillations.* In the Standard Model neutrinos are massless. There is now compelling evidence that neutrinos have masses [1], [10] and [11],

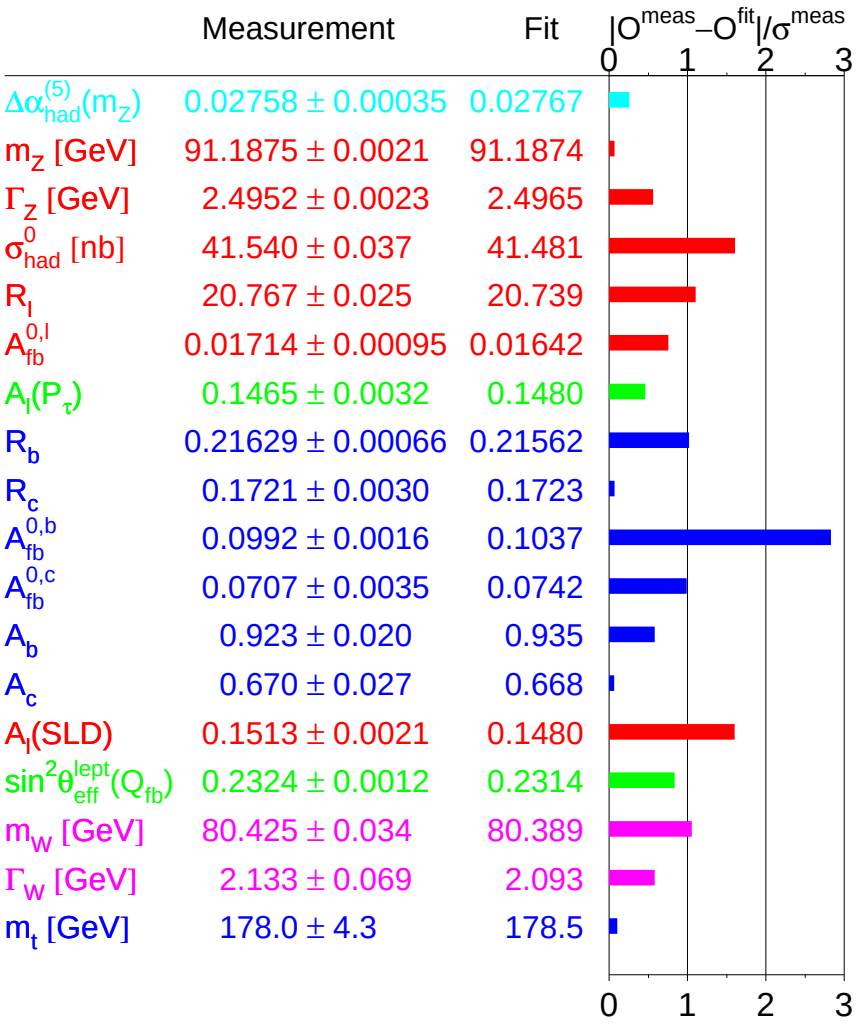

Figure 1.2: *The Precision Electroweak measurements. Comparison of the measurements with the expectation of the SM, calculated for the five input parameter values in the minimum of the global χ^2 of the fit. Also shown is the pull of each measurement, where pull is defined as the difference of measurement and expectation in units of the measurements uncertainty. The direct measurements of m_W and Γ_W reported here are preliminary. From [7].*

while in the minimal Standard Model (i.e. without including the right-handed neutrinos) these are vanishing at any order. All most popular extensions of the SM that can account for non-zero neutrino masses call for a higher energy scale.

5. *The unification of the gauge couplings.* The coupling strengths of the strong, weak and electromagnetic interactions should unify at some energy scale if one believes that the three elementary interactions result from a local gauge theory with a higher fundamental symmetry.

6. *The hierarchy problem.* The Standard Model is note the "Theory of Everything" since gravitational interaction is not included. The unification of gravity calls for a higher energy scale around 10^{19} GeV, at which energy the gravitational interaction becomes comparable to gauge forces. This is called *Planck mass* (M_P).

The Hierarchy Problem

There are three fundamental constants in physics: the speed of light c, Planck's constant h and Newton's constant G. Using these constants a mass can be formed, the *Planck mass*:

$$M_P = \sqrt{\frac{hc}{G}} \approx 10^{19} GeV. \tag{1.7}$$

This is a fundamental scale in nature, at this energy quantum gravitational effects become important. On the other hand, the mass scale of electroweak symmetry breaking is set by m_W, m_Z and m_h, which are around 100 GeV. the hierarchy problem is the big question why the typical energy scale associated with the electroweak symmetry breaking is so much (10^{15} times) smaller than the Planck energy. The question is why the Higgs boson is so much lighter than the Planck mass, although one would expect that the large (quadratically divergent) quantum contributions to the Higgs boson mass squared would inevitably make the mass huge, comparable to the Planck mass.

The physical Higgs mass squared is given by the "bare" Higgs mass squared plus the corrections from loop diagrams:

$$m_H^2 = (m_H^2)_0 + \Delta m_H^2. \tag{1.8}$$

The correction to m_H^2 from a loop containing a Dirac fermion (Figure 1.3-(a)) is given by [12]:

$$\Delta m_H^2|_F = \frac{|\lambda_F|^2}{16\pi^2}(-2\Lambda_{UV}^2 + 6m_F^2 \ln(\Lambda_{UV}/m_F) + ...) \tag{1.9}$$

where m_F is the fermion mass and λ_F is the strength with which the Higgs boson couples to the fermions; while ΛUV is an ultraviolet cutoff used to regulate the loop integral. In the case of coloured fermions the equation should be multiplied by 3.
The loop correction generates a quadratic divergence in ΛUV with negative sign. In the Standard Model the largest correction comes from the top quark with $|\lambda_t| \approx 1$. Λ_{UV} can be interpreted as the energy scale at which new physics enters to alter the high-energy behaviour of the theory. If no new physical phenomena occur between the electroweak scale and the

Plank scale, then $\Lambda_{UV} \approx m_P$ and the quantum correction is come 30 orders of magnitude larger than the aimed-for value of $m_H^2 \approx 100GeV^2$. Considering equation 1.8, this means that the bare Higgs mass $(m_H^2)_0$ should also be of the order of the Plank mass.

Similar to equation 1.9, corrections to m_H^2 can come from a loop containing a boson (Figure 1.3-(b)). In the case of a scalar with mass m_B the correction is given by:

$$\Delta m_H^2|_B = \frac{\lambda_B}{16\pi^2}(\Lambda_{UV}^2 - 2m_B^2 \ln(\Lambda_{UV}/m_B) + ...). \tag{1.10}$$

It is interesting to note that this correction also generates a quadratic divergence in Λ_{UV}, but its sign is opposite to that from a fermion loop.

From equations 1.9 and 1.10 it can be seen that if every fermion in the theory would be accompanied by two bosons with $\lambda_B = \lambda_F^2$, the quadratic ultraviolet divergences would cancel exactly. Only a residue involving the mass differences would remain. The cancellation of two large terms with a small residue resembles a symmetry that is softly broken. Such a symmetry would relate fermions to bosons and it is called *supersymmetry*. Other possible extensions of the Standard Model that solve, or at least shift, the hierarchy problem include *little Higgs model* and *extra dimension theories*, but they will not be further discussed here.

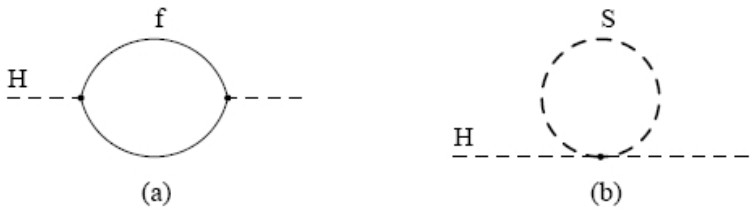

Figure 1.3: *Quantum corrections to the Higgs* $(mass)^2$ *coming from fermion (a) and boson (b) loops [12].*

Unification of Gauge Couplings

The success of the common description of the electric, magnetic and weak forces have led to the hope that the three elementary interactions (and maybe later also gravitation) will be unify as the result of a single simple symmetry group. This implies that the strength of the strong, weak and electromagnetic interactions should unify at some energy scale. In the Standard Model the coupling "constants" are indeed not constant but a function of the energy scale Q at which the interaction take place:

$$\alpha_i = \alpha_i(\frac{Q^2}{Q_0^2}), \qquad \alpha_i = \frac{g_i^2}{4\pi} \tag{1.11}$$

where Q_0 is a reference scale, $g_1 = \sqrt{5/3}g'$, $g_2 = g$ and $g_3 = g_s$, with g', g and g_s the usual $U(1) \times SU(2) \times SU(3)$ coupling constants. This energy dependence is described by the

renormalization group equations (RGE):

$$\frac{d}{dt}(1/\alpha_a(t)) = -\frac{b_a}{4\pi}, \quad with \quad t = \log\left(\frac{Q^2}{Q_0^2}\right) \quad and \quad a = (1,2,3), \tag{1.12}$$

showing that the inverse couplings evolve linearly with the scale parameter t. This relation is confirmed by experiments.

Unification requires that, at some energy scale, all couplings become equal, $\alpha_1 = \alpha_2 = \alpha_3 = \alpha_{GUT}$. In the SM the coefficients b_i are given by:

$$\begin{aligned} b_1 &= -\frac{1}{10}n_h - \frac{4}{3}n_g \\ b_2 &= -\frac{1}{6}n_h - \frac{4}{3}n_g + \frac{22}{3} \\ b_3 &= -\frac{4}{3}n_g + 11, \end{aligned} \tag{1.13}$$

where n_g is the number of quark and lepton generations and n_h is the number of Higgs doublet fields. With $n_g = 3$ and $n_h = 1$ these give numerically:

$$b_1 = \frac{41}{10}, \quad b_2 = -\frac{19}{6}, \quad b_3 = -7. \tag{1.14}$$

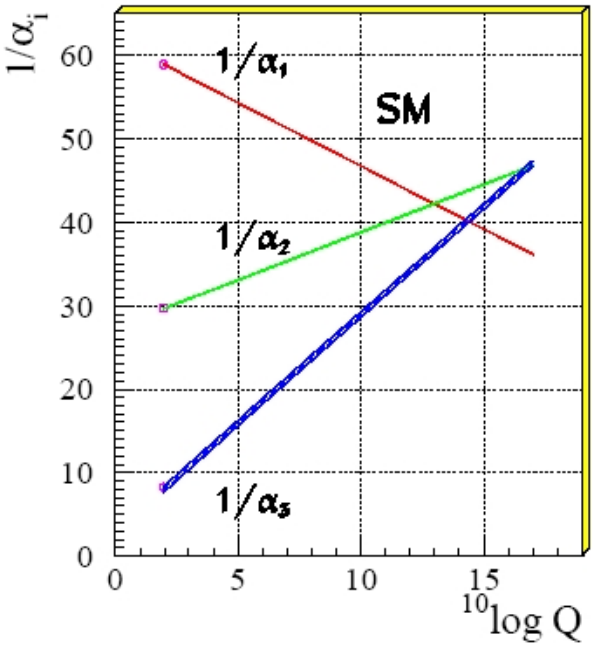

Figure 1.4: *Evolution with energy Q (in GeV) of the inverse of the three coupling constants, assuming the Standard Model. The thickness of the lines reflects the experimental uncertainty in the coupling constant determination.*

Figure 1.4 shows the evolution of the coupling constants assuming the Standard Model particle content. It is clear that coupling constant unification at a single point is not possible

and statistically excluded at a level of 12σ. Consequently true unification can only be obtained if new physics enters between the electroweak and Planck scale, modifying the slope of the evolution of the couplings.

1.2 Principles of SuperSymmetry

Supersymmetry (SUSY) is a symmetry which connects fermions (matter particles) and bosons (force carriers) each other. The supersymmetry operator Q generates such transformations:

$$Q|boson>=|fermion>, \qquad Q|fermion>=|boson> . \tag{1.15}$$

The operator Q and its hermitian conjugate Q satisfy the following commutation and anti-commutation relations:

$$\begin{aligned} \{Q, Q^\dagger\} &= P^\mu, \\ \{Q, Q\} &= \{Q^\dagger, Q^\dagger\} = 0, \\ [P^\mu, Q] &= [P^\mu, Q^\dagger] = 0, \end{aligned} \tag{1.16}$$

where P^μ is the space-time translations momentum generator. These define the *supersymmetry algebra*.

The single-particle states of a supersymmetric theory fall naturally into irreducible representations of the supersymmetry algebra. These representations are called *supermultiplets*. Each supermultiplets contains both fermion and boson states, which are commonly known as *superpartners* of each other; and the number of boson and fermion degrees of freedom in a supermultiplet must be equal ($n_B = n_F$). Since the $(mass)^2$ operator $-P^2$ commutes with the operators Q and $Q^\dagger$, particles in the same irreducible supermultiplet must have equal eigenvalues of $-P^2$, and therefore equal masses. The supersymmetry generators Q and $Q^\dagger$ also commute with the generators of gauge transformation. Therefore particles in the same supermultiplet must also be in the same representation of the gauge group, and so must have the same electric charges, weak isospin and color degree of freedom.

Trying to construct the simplest supermultiplets consistent with these constraints, a first possibility would be to pair a fermion with two real (or one complex) scalar bosons (both two degree of freedom), and this combination is called a *chiral* or *matter supermultiplet*; another possibility is to combine a massless vector boson (again two degrees of freedom) with a fermion; such a pairing is called *vector* or *gauge supermultiplet*. There are other combinations of particles possible, however it can be shown that these are always reducible to combinations of chiral and gauge multiplets if their interactions are to be renormalizable.
One might wonder whether any of the known particles in the Standard Model could be linked together in supermultiplets. Unfortunately none of the known fermions can be paired with any of the known bosons because their internal quantum numbers do not match. For example, quarks sit in triplet representations of colour whereas the known bosons are either singlets or octets of colour. Thus the only possibility seems to be the introduction of new supersymmetric

partners (*spartners*) for all SM particles. The Minimal Supersymmetric Standard Model (MSSM) contains the minimal extension of the Standard Model particle content.

1.3 The Minimal Supersymmetric Extension of the Standard Model

As it was just discussed, each of the fundamental particles must resides in either a chiral or a gauge supermultiplet and their superpartners must have a spin differing by 1/2 unit. None of the Standard Model bosons can be the superpartner of a Standard Model fermion or vice versa because their gauge quantum numbers are different. Therefore all superpartners must be "new" particle, that is particles did not yet discovered.

All Standard Model fermions fit naturally into chiral multiplets. Their scalar superpartners all carry the name of the original particle preceded by an "*s*", and the symbols are the same as for the corresponding fermion, but with a tilde used to denote the superpartner of the Standard Model particle; *e.g*: *squarks* ($\tilde{q}$) and *leptons* ($\tilde{l}$) in general, and *stops* ($\tilde{t}$) and *staus* ($\tilde{\tau}$) in particular. A summary of the Standard Model fermions and their scalar superpartners is given in table 1.3.

Name	Spin 0	Spin 1/2	SU(3)×SU(2)×U(1)
squarks, quarks	$(\tilde{u}_L,\ \tilde{d}_L)$	$(u_L,\ d_L)$	(3,2,1/6)
	$\tilde{u}_R$	u_R	(3,1,2/3)
	$\tilde{d}_R$	d_R	(3,1,-1/3)
sleptons, leptons	$(\tilde{\nu},\ \tilde{e}_L)$	$(\nu,\ e_L)$	(1,2,-1/2)
	$\tilde{e}_R$	e_R	(1,1,-1)

Table 1.3: *Fermions and their sfermions partner in the Minimal Supersymmetric extension of the Standard Model.*

The vector bosons of the Standard Model naturally reside in gauge supermultiplets. Fermionic superpartners of gauge bosons are named by adding "*-ino*" after the name of the Standard Model particle. The gluon g, carrier of the strong color interactions, has a spin-1/2 *gluino* partner $\tilde{g}$ and the electroweak gauge bosons W^+, W^0, W^- and B^0 have spin-1/2 superpartners $\tilde{W^+}$, $\tilde{W^0}$, $\tilde{W^-}$ and $\tilde{B^0}$, called *winos* and *binos*. Generically they are called *gauginos*. Alternatively the superpartners of the photon and Z^0 (linear combination of $\tilde{W^0}$ and $\tilde{B^0}$) may be called *photino* and *zino*. Table 1.4 summarizes the gauge supermultiplets of the MSSM.

Since it has spin-0, it seems that the Higgs boson must reside in a chiral supermultiplet. However it turns out that one supermultiplet is not sufficient. There are two reasons for this; first, because the structure of supersymmetric theories, only a $Y = +1/2$ Higgs chiral supermultiplet can have the Yukawa couplings necessary to give masses to charge $+2/3$ up-type quarks, and also only a $Y = -1/2$ Higgs chiral supermultiplet can have the Yukawa couplings necessary to give masses to charge $-1/3$ down-type quarks and to charged leptons.

Name	Spin 1/2	Spin 1	SU(3)×SU(2)×U(1)
gluino, gluon	$\tilde{g}$	g	(8,1,0)
winos, W bosons	$\tilde{W^{\pm}}$, $\tilde{W^0}$	$W^{\pm}$, W^0	(1,3,0)
bino, B boson	$\tilde{B^0}$	B^0	(1,1,0)

Table 1.4: *Gauge bosons and their gaugino partners in the Minimal Supersymmetric extension of the Standard Model.*

The second argument for having two Higgs doublets in the MSSM comes from the gauge anomaly cancellation requirement, so adding two doublets, one with $Y = +1/2$ and one with $Y = -1/2$, the cancellation of the anomalous terms in triangle loop diagrams involving chiral fermions was preserved. The Higgs field corresponding to the positive hypercharge will be called H_u, and the one corresponding to the negative hypercharge H_d. The weak isospin components of H_u with $T_3 = (+1/2, -1/2)$ have electric charges 1 and 0 respectively, and they are denoted (H_u^+, H_u^0). Similarly the $SU(2)$-doublet complex scalar H_d has $T_3 = (+1/2, -1/2)$ components (H_d^0, H_d^-). The neutral scalar that corresponds to the physical Standard Model Higgs boson is a linear combination of H_u^0 and H_d^0. According to the nomenclature introduced above, the fermionic partners of the Higgs bosons are called *higgsino*, and they are listed in table 1.5.

Name	Spin 0	Spin 1/2	SU(3)×SU(2)×U(1)
Higgs, higgsinos	(H_u^+, H_u^0)	$(\tilde{H_u^+}, \tilde{H_u^0})$	(1,2,+1/2)
	(H_d^0, H_d^-)	$(\tilde{H_d^0}, \tilde{H_d^-})$	(1,2,-1/2)

Table 1.5: *Higgs bosons and their higgsinos partners in the Minimal Supersymmetric extension of the Standard Model.*

The mixing of particle states significantly complicates the interpretation of the supersymmetric particle masses. The phenomenologically most important mixings happen between the superpartners of the gauge and Higgs bosons: after the electroweak symmetry breaking the charged winos $\tilde{W^{\pm}}$ and higgsinos $\tilde{H_u^+}$, $\tilde{H_d^-}$ have the same quantum numbers and will therefore mix. The mass eigenstates of this system, which are the physically observable particles, are called *charginos* and denoted as

$$\chi_1^+, \chi_1^-, \quad \chi_2^+, \chi_2^-. \tag{1.17}$$

By convention the $\chi_1^{\pm}$ is the lightest of the two states. Similarly, the neutral wino $\tilde{W^0}$, the bino $\tilde{B^0}$ and the neutral higgsinos $\tilde{H_u^0}$, $\tilde{H_d^0}$ will mix to form four states

$$\chi_1^0, \chi_2^0, \chi_3^0, \chi_4^0, \tag{1.18}$$

called *neutralinos*, again noted from the lightest to the heaviest (Table 1.6).

Apart from the gaugino/higgsino mixing, also the two scalar partners of each heavy quark

Name	Spin	Gauge Eigenstates	Mass Eigenstates
Neutralinos	1/2	$\tilde{B^0}$, $\tilde{W^0}$, $\tilde{H_u^0}$, $\tilde{H_d^0}$	χ_1^0, χ_2^0, χ_3^0, χ_4^0
Charginos	1/2	$\tilde{W^\pm}$, $\tilde{H_u^+}$, $\tilde{H_d^-}$	$\chi_1^\pm$, $\chi_2^\pm$.

Table 1.6: *Gauge and mass eigenstates for gauginos.*

or lepton mix together, as for example $\tilde{t}_L$ and $\tilde{t}_R$ mix and form the mass eigenstates $\tilde{t}_1$ and $\tilde{t}_2$.

1.3.1 R-parity

R parity is a multiplicative quantum number such that all particles of the Standard Model have R parity +1, while their SUSY partners have R parity -1. R parity is defined as:

$$R = (-1)^{3B+L+2S} \tag{1.19}$$

where L is the lepton number, B is the baryon number and S is the spin [13].

The assumption of R parity conservation has profound experimental consequences which go beyond the details of a specific model. Because R parity is a multiplicative quantum number, it implies that the number of SUSY partners in a given interaction is always conserved modulo 2.

1. SUSY partners can only be pair produced from Standard Model particles.

Furthermore, a SUSY particle will decay in a chain until the lightest SUSY particle is produced (such a decay is called a cascade decay). This lightest SUSY particle, called the LSP, must be absolutely stable when R parity is conserved.

2. A theory with R parity conservation will have a lightest SUSY particle (LSP) which is stable.

The LSP must be neutral since there are stringent cosmological bounds on light charged or colored particles which are stable. If R parity is violated then it is possible for some other particle (such as the gluino) to be the LSP. Hence the LSP is stable and neutral and is not seen in a detector (much like a neutrino) since it interacts only by the exchange of a heavy virtual SUSY particle.

3. The LSP will interact very weakly with ordinary matter.

So a generic signal for R parity conserving SUSY theories is missing transverse energy from the non-observed LSP. In theories without R parity conservation, there will not be a stable LSP, and the lightest SUSY particle will decay into ordinary particles (possibly within the detector). Missing transverse energy will no longer be a robust signature for SUSY particle production.

1.3.2 Benchmarks for Supersymmetry Searches

In the unconstrained version of the Minimal Supersymmetric extension of the Standard Model no particular Supersymmetry breaking mechanism is assumed, but rather a parameterization of all possible soft SUSY breaking terms is used. As said above, this leads to more than a hundred parameters (masses, mixing angles, phases) in this model in addition to the ones of the Standard Model. The currently most popular SUSY breaking mechanisms are:

- minimal SUperGRAvity, *mSUGRA* [14],
- Gauge-Mediated Supersymmetry Breaking, *GMSB* [15],
- Anomaly-Mediated Supersymmetry Breaking,*AMSB* [16].

In these scenarios SUSY breaking happens in a hidden sector. This "hidden sector" of particles have not direct coupling to the particles in the chiral supermultiplets in the "visible sector". Anyway the two sectors share some interactions and the symmetry breaking is communicated to the visible sector through some messenger interaction that couples to both. Phenomenologically viable models are classified in terms of how the SB takes place and how it is transmitted to our observable sector. In almost all of the models, SUSY is broken dynamically at a high scale and then this breaking is mediated to our low energy world. Thus the supersymmetry breaking is mediated to the visible sector in different ways: via gravitational interactions in the mSUGRA scenario, via gauge interactions in the GMSB scenario, and via the super-Weyl anomaly in the AMSB scenario. Assuming one of these SUSY breaking mechanisms leads to a drastic reduction of the number of parameters compared to the MSSM case.

For example in minimal supergravity models, mSUGRA, in which gravity is the sole messenger, it is assumed that the scenario can be parametrized at the GUT scale by four parameters and a sign:

- m_0, the universal scalar mass parameter,
- $m_{1/2}$, the universal gaugino mass parameter,
- A_0, the SUSY trilinear Higgs-sfermion-sfermion coupling,
- $\tan\beta$, the ratio of the Higgs fields vacuum expectation values,
- $sign(\mu)$, the sign of the higgsino mass parameter.

The parameters of the (minimal) GMSB scenario are the messenger mass $M_{\rm mes}$, the messenger index $N_{\rm mes}$, the universal soft SUSY breaking mass scale felt by the low-energy sector, Λ, as well as $\tan\beta$ and $\mathrm{sign}(\mu)$.

The (minimal) AMSB scenario has the parameters $m_{\rm aux}$, which sets the overall scale of the SUSY particle masses (given by the vacuum expectation value of the auxiliary field in the supergravity multiplet), $\tan\beta$, $\mathrm{sign}(\mu)$, and m_0, where the latter is a phenomenological parameter introduced in order to keep the squares of slepton masses positive.

The mass spectra of the SUSY particles in these scenarios are obtained via renormalization group running from the scale of the high-energy parameters of the SUSY-breaking scenario to the weak scale. The low-energy parameters obtained in this way are then used as input for calculating the predictions for the production cross sections and for the decay branching ratios of the SUSY particles.

1.4 Why Supersymmetry is the most attractive extension of the Standard Model

In this section it will be reported how the supersymmetry theories solve several defects of the Standard Model outlined in section 1.1.3.

1.4.1 The Supersymmetric Solution of the Hierarchy Problem

Supersymmetry proposes a natural solution to the Hierarchy problem, providing the masses of the superpartners are not to large.

In a supersymmetric theory each of the Standard Model quark and lepton doublets resides in a chiral supermultiplet so it is accompanied by two complex scalars with couplings $\lambda_B = |\lambda_F|^2$. Since bosonic and fermionic loops have opposite signs as can be see in equations 1.9 and 1.10, the quadratic divergences cancel and the residual one-loop correction to the Higgs $(mass)^2$ is given by:

$$\Delta m_H^2|_{tot} \simeq \frac{|\lambda_F|^2}{4\pi^2}\left(\frac{3}{2}m_F^2 - m_B^2\right)\ln\frac{\Lambda_{UV}}{m_F}. \tag{1.20}$$

Considering equation 1.8, this means that the bare Higgs mass must be:

$$(m_H^2)_0 = \mathcal{O}\left(\frac{\lambda_F^2}{\pi}\right)(m_B^2 - m_F^2), \tag{1.21}$$

which is of the order of m_H^2 and hence naturally small if the supersymmetric partner bosons B and fermions F have similar masses:

$$\left|m_B^2 - m_F^2\right| \lesssim 1TeV^2. \tag{1.22}$$

Cancellations of higher order loops are also guaranteed if supersymmetry is invoked. Relation 1.22 provides one of the best motivations for the occurrence of supersymmetry at relatively low energies.

1.4.2 Unification of Gauge Couplings

The second main motivation for supersymmetry is related to unification theory. In section 1.1.3 it was reported that the coupling strengths of the strong, weak and electromagnetic interactions do not unify at a single point in the Standard Model. Since the MSSM doubles

the particle content of the Standard Model, the slope of the evolution of the gauge couplings in equation 1.12 will be altered. In the MSSM the coefficients b_i are:

$$b_1 = \frac{3}{5}, \quad b_2 = 5, \quad b_3 = -3, \tag{1.23}$$

and with these numbers a perfect unification of the gauge couplings can be obtained if the sparticle masses are of the order of 1 TeV (Figure 1.5). In the plot in figure 1.5 the supersymmetric particles are assumed to effectively contribute to the running of the coupling constants only for energies above the typical SUSY mass scale, which causes the change in slope of the lines near 1 TeV.

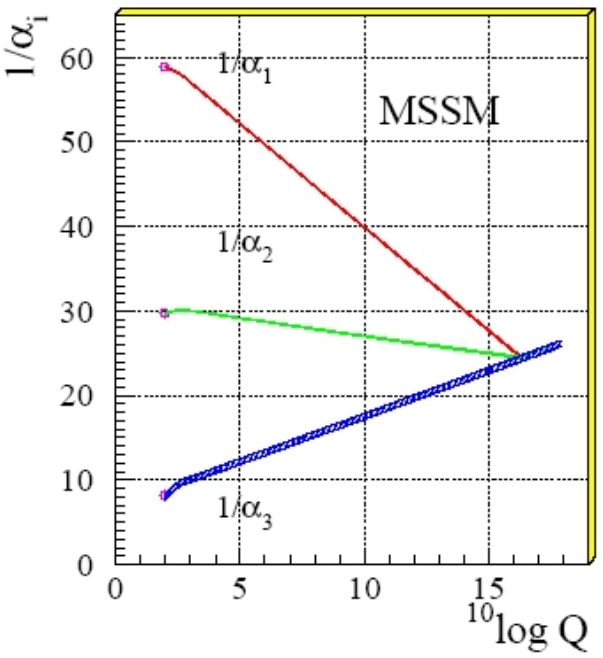

Figure 1.5: *Evolution with energy Q (in GeV) of the inverse of the three coupling constants, assuming the Minimal Supersymmetric extension of the Standard Model. The mass of the sparticles is assumed to be 1 TeV. The thickness of the lines reflects the experimental uncertainty in the coupling constant determination.*

Imposing unification a fit yields the values for the break point M_{SUSY} and the unification point M_{GUT} [17]:

$$\begin{aligned} M_{SUSY} &= 10^{3.4\pm0.9\pm0.4} GeV, \\ M_{GUT} &= 10^{15.8\pm1.9\pm1.0}. \end{aligned} \tag{1.24}$$

The first error originates from the uncertainty in the coupling constants, the second one from the uncertainty in the mass splitting between the supersymmetric particles. The errors in M_{SUSY} show that unification is not very sensitive to the exact value of the SUSY masses as a range of 100 $GeV \leq M_{SUSY} \leq 10$ TeV can be accommodated.

1.4.3 The Supersymmetric Dark Matter

Many astrophysical measurements point to the existence of nonrelativistic, neutral, nonbaryonic dark matter in the Universe [9]. All attempts to explain the observations using

Standard Model particles have failed, because the SM candidate, the neutrino, is too light.

In the R-parity conserving MSSM the lightest supersymmetric particle (LSP) is always stable; so this LSP is a good candidate for the cold dark matter in the Universe. There are strong constraints on the nature of such a candidate: it must be electrically and colour neutral, since otherwise it should have bound with normal matter forming anomalously heavy isotopes that would have been detected.

The present lifetime of the Universe is about 10^10 years, which implies an upper limit on the expansion rate and, correspondingly, on the total relic abundance. The latest constraints on dark matter from the WMAP experiment [18] lead to (at 95% confidence level):

$$0.094 \leq \Sigma_\chi h^2 \leq 0.129. \tag{1.25}$$

There are a number plausible supersymmetric dark matter candidates [19], but the most favoured is the LSP neutralino, χ_1^0. The attractive feature of LSP neutralino is that it has a relic density in accordance with 1.25 over large domains of the MSSM parameter space.

1.5 Summary

In this chapter the main features of the Standard Model are very briefly reviewed, with a focus on the electroweak symmetry breaking. Some defects of the Standard Model are also discussed, such as the hierarchy problem, the non-unification of gauge couplings, the dark matter problem and the fact that the gravity cannot be accommodated within the theory.

The principles of Supersymmetry, a symmetry which relates fermions and bosons, are explained and it is shown how a Minimal Supersymmetric extension of the Standard Model provides a satisfactory solution to most of these problems.

The particle content of the Minimal Supersymmetric Standard Model is discussed. In MSSM every Standard Model particle has a supersymmetric partner that differs from it with half a unit in spin. The introduction of $R-$parity, a discrete symmetry, has a consequence that supersymmetric particles are only produced in pairs and that there exists a stable lightest supersymmetric particle, the LSP.

Since in a fully supersymmetric theory the masses of the superpartners should be equal to the masses of their Standard model counterparts, which is clearly not the case, supersymmetry must necessarily be a broken symmetry. Whereas the introduction of Supersymmetry only added one extra free parameter to the Standard Model, supersymmetry breaking leads to a theory with 105 additional free parameter. In order to reduce this number, several SUSY breaking mechanisms have been developed.

The Higgs sector of the MSSM is introduced. Contrary to the Standard Model, the Higgs sector contains five physical Higgs bosons: two CP-even neutral scalars, h and H, one CP-odd neutral scalar, A, and a pair of charged Higgs bosons, $H^\pm$. At tree level, their masses and couplings are determined by only two parameters, m_A and $\tan\beta$. Also the phenomenologically important aspects of neutralino, chargino, squark and slepton mixing are reported.

Bibliography

[1] *Y. Fukada et al. (SuperKamiokande Collaboration)*, ***Tau Neutrinos Favored over Sterile Neutrinos in Atmospheric Muon Neutrino Oscillations***, Phys. Rev. Lett. 85, 3999, 2000.

[2] *M. Ambrosio et al. (MACRO Collaboration)*, ***Matter Effects in Upward-going Muons and Sterile Neutrino Oscillations***, Phys. Lett. B 517, 59-66, 2001.

[3] *Particle Data Group*, ***Review of Particle Physics***, Phys. Lett. B 592, 1, 2004.

[4] *S. Glashow*, ***Six-Fermion Weak Interactions***, Phys. Rev. 133, B130-B131, 1964.

[5] *S. Weinberg*, ***A Model of Leptons***, Phys. Rev. Lett. 19, 1264, 1967.

[6] *P. Higgs*, ***Broken Symmetries and the Masses of Gauge Bosons***, Phys. Rev. Lett. 13, 508, 1964.

[7] *The ALEPH, DELPHI, L3, OPAL, SLD Collaboorations; the LEP Electroweak Working Group; the SLD Electroweak and Heavy Flavour Group*, ***Precision Electroweak Measurements on the Z Resonance.***, CERN hep-ex/0509008, 2005.

[8] *The ALEPH, DELPHI, L3, OPAL Collaborations; The LEP working Group for Higgs Boson Searches*, ***Search for the Standard Model Higgs Boson at LEP***, CERN hep-ex/0306033, Phys. Lett. B565, 61-75, 2003.

[9] *E. Kolb and M. Turner*, ***The Early Universe***, Addison-Wesley, New York, 1989.

[10] *H. Pas*, ***Neutrino Masses and Particle Physics Beyond the Standard Model***, hep-ph/0209018, Annalen Phys. 11 551, 2002.

[11] *N. Schmitz*, ***The Discovery of Neutrino Masses***, hep-ex/0211041, 2002.

[12] *S. Martin*, ***A Supersymmetry Primer***, hep-ph/9709356, 1998.

[13] *J. Ellis*, ***Beyond the Standard Model for Hillwalkers***, CERN Yellow-Report 99-04, Proceeding of 1998 European School of High Energy Physics, St Andrews, Scotland, 1999.

[14] *H. P. Nilles*, ***Dynamically Broken Supergravity and the Hierarchy Problem***, Phys. Lett. B 115, 193, 1982.

[15] *G. F. Giudice, R. Rattazzi*, ***Theories with Gauge-Mediated Supersymmetry Breaking***, hep-ph/9801271, Phys. Rep. 322, 419, 1998.

[16] *L. Randall, R. Sundrum*, ***Out of This World Supersymmetry Breaking***, hep-th/9810155, Nucl. Phys. B 557 79-118.

[17] *D. I. Kazakov*, ***Beyond the Standard Model (in Search of Supersymmetry)***, hep-ph/0012288, Proceeding of 2000 European School of High-Energy Physics, Caramulo, Portugal, 2001.

[18] *D. N. Spergel et al.*, ***First Year Wilkinson Microwave Anisotropy Probe (WMAP) Observations: Determination of Cosmological Parameters***, astro-ph/0302209, 2003.

[19] *A. Bottino and N. Fornengo*, ***Dark Matter and its Particle Candidates***, hep-ph/9904469, 1999.

Chapter 2

The LHC Project and the ATLAS Experiment

This chapter gives an introduction to the **L**arge **H**adron **C**ollider (LHC). The next generation of high-energy physics research facilities has to operate in the TeV scale range in order to address important new issues of elementary particle physics. The LHC project will allow to explore particle physics up to energy values which dominated the early Universe, just $10^{-12}s$ after the "Big Bang" when the temperature was about $10^{16}K$. In this chapter the physics potential of the collider and its impact on the design of the ATLAS experiment are discussed, and an overview of the full ATLAS detector is given as reported in the Technical Design Report [1].

2.1 The Large Hadron Collider

The Large Hadron Collider project [2] was approved by CERN ('Centre Européen pour la Recherche Nucléaire') Council in December 1994. The LHC accelerator is presently being installed in the existing LEP (electron-positron collider) tunnel (Figure 2.1). It will accelerate protons to an unprecedented energy of 7 TeV, providing proton-proton collision at a centre-of-mass energy $\sqrt{s} = 14\ TeV$ and heavy-ion collisions with a centre-of-mass energy of 1148 TeV. This centre-of-mass energy presents a great challenge for accelerator technology. To supply the LHC with pre-accelerated protons, the existing CERN facilities have been upgraded. Protons will be accelerated through many steps by the already existing machines: a Linac will bring them up to 50 MeV, a Booster up to 1.4 GeV, the PS up to 25 GeV and the SPS up to 450 GeV. Finally, protons will be injected in the Large Hadron Collider where they will be accelerated up to 7 TeV. Figure 2.2 shows an overview of the CERN acceleration complex.

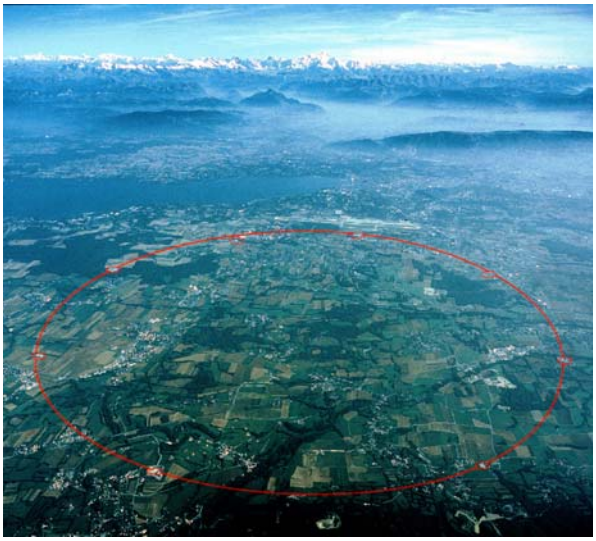

Figure 2.1: *Aerial view of the CERN site showing the path of the 27 kilometers tunnel housing the LHC collider. The tunnel was excavated in the 1980's to house the LEP collider. This was closed in 2000. Geneva airport is visible (lower right).*

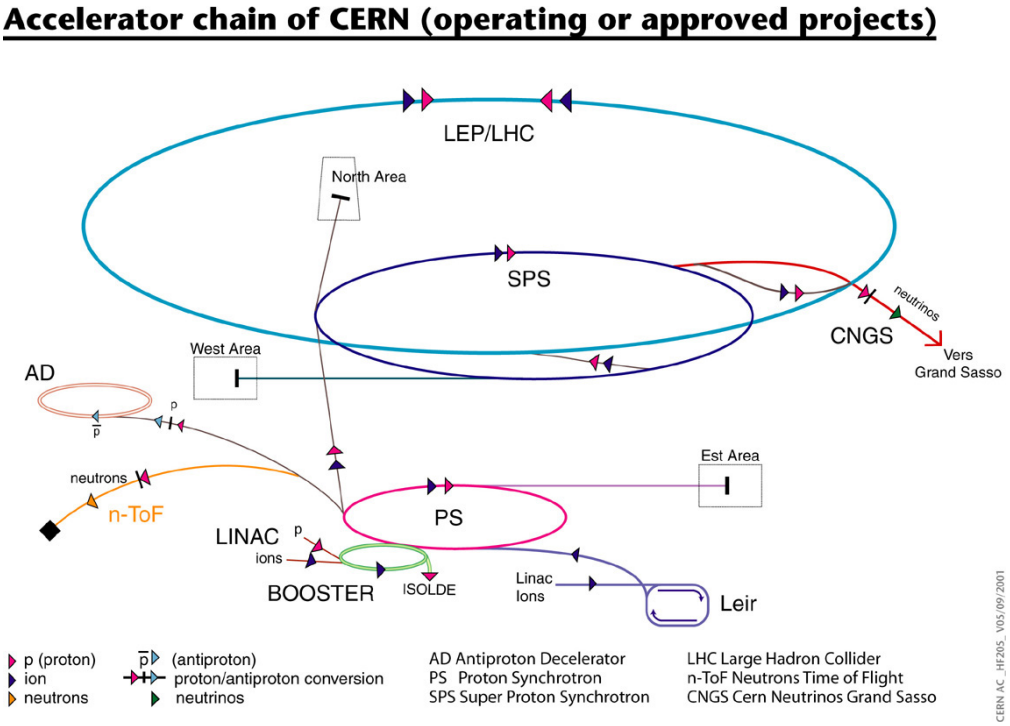

Figure 2.2: *An overview on the accelerator complex at CERN. Before being injected into the 27 km LHC storage ring, protons pass a series of pre acceleration stages. When the energy of 7 TeV has reached, the protons are brought to collision in the four interaction points, each of which equipped with a large experimental apparatus: ATLAS, CMS, LHCb and ALICE.*

The use of particle of the same type, contrary to LEP and Tevatron at Fermilab (proton-antiproton collider) offers important advantages with respect to the beam lifetime. However it requires two separate channels with opposite beam directions. The two channels, together with their superconducting dipole magnets will be inserted in a single cryostatic structure (Figure 2.3). Dipoles will operate at 1.9 K, where Helium becomes superfluid, and will provide a $\sim$ 9 T magnetic field. The boost will be provided by 400 MHz superconducting radiofrequency cavities. Table 2.1 summarizes the main LHC parameters.

Parameters	**Values - *pp* running mode**
Circumference	27 km
Number of magnet dipoles	1232
Dipolar magnetic field	8.386 T
Magnet temperature	1.9 K
Centre of mass energy	14 TeV
Beam energy	7 TeV/charge
Bunch spacing	25 ns
Bunches per ring	2835
Protons per bunch	10^{11}
Initial luminosity	$10^{33} cm^{-2} s^{-1}$
Design luminosity	$10^{34} cm^{-2} s^{-1}$

Table 2.1: *Main technical machine parameters of LHC.*

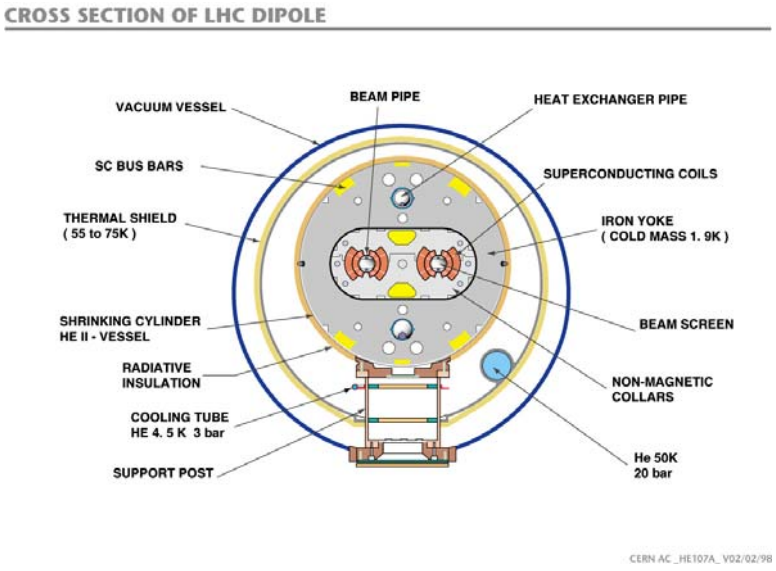

Figure 2.3: *A schematic cross section of the LHC dipole.*

2.1.1 Phenomenology of proton-proton collisions

Physics at a pp collider provides different features with respect to LEP. When elementary particles like e^+e^- collide, the interaction energy is fixed, providing clean experimental conditions. Light particles, however, are limited by the energy loss of the synchrotron radiation emission which at LEP amounted to $E_{loss} = 2.8\ GeV$ per turn. Hadron colliders are not limited by the same energy loss, because $E_{loss}^{proton} = 10^{-13} E_{loss}^{electron}$, but the experimental conditions are worse.

Protons are clustered into bunches and the nominal number of protons per bunch will be 10^{11}, colliding at a given interaction point every 25 ns. Bunches will have a very small transverse spread, $\sigma_x \sim \sigma_y \sim$15 μm, while they will be 7.5 cm long in the z direction at the collision points. The accelerator parameter related to the rate on interaction is the *Luminosity* ($\mathcal{L}$):

$$\mathcal{L} = f \frac{n_1 n_2}{4\pi\sigma_x\sigma_y} \tag{2.1}$$

where f is the revolution frequency, n_1 and n_2 are the number of protons per bunch for the two colliding beams respectively, σ_x and σ_y are the widths which characterize the Gaussian transverse beam profiles in the horizontal (bending) and vertical directions respectively. The number of interaction N_i, corresponding to the process i with a cross-section σ_i, depends on L and it is given by the relationship:

$$N_i = \sigma_i \int \mathcal{L} dt \tag{2.2}$$

This collider is foreseen to operate in two successive phases: during the first few years the luminosity will be $\sim 10^{33} cm^{-2} s{-}1$ (*low luminosity run*) and this period will be mainly dedicated to tune the performances of the detectors. Afterwords the luminosity will be increased to the design value of $\sim 10^{34} cm^{-2} s{-}1$ (*high luminosity phase*).

Inelastic processes dominate high-energy hadron collisions that are characterized by multiple production of secondary mesons and baryon-antibaryon pairs. Given the total inelastic proton-proton cross section of about 100 mb, the event rate R, defined as the number of events produced per second, is expected to be:

$$R = \sigma \cdot \mathcal{L} = 100mb \cdot 10^{34} cm^{-2} s^{-1} \simeq 10^9 s^{-1} \tag{2.3}$$

when running at high luminosity [3]. The feature of hadron-hadron collisions at high energy are dominated by the long-distance confining behaviour of the strong forces between the two incoming hadrons. In this case the momentum transfer of the interaction is small (soft collision) and therefore particle scattering at large angles is suppressed. The final state particles have large longitudinal momentum, but small transverse momentum p_T relative to the beam line ($\langle p_T \rangle \approx 500 MeV$). Most of the collision energy escapes in a very narrow cone around the beam pipe. Final states arising from these soft interactions are called *"minimum bias"* events. They represent the majority of the pp collisions, but they are not of big interest: actually it is virtually impossible, from such soft collisions, to gain any insight on the nature of the elementary quark and gluon constituents of the hadrons.

However it is possible, at extremely high collision energies, to select very rare events whose characteristics are determined largely by the short-distance behaviour of the quark-quark interaction. Since monochromatic proton beams can be seen as beams of partons (quarks and gluons) with a wide spectrum of energies, these events correspond to the occasional "head-on" or hard collision between two partons of the incoming protons. These interaction occur at small distances and therefore are characterized by large momentum transfers (hard scattering). In this case final state particles can be created. These are the more interesting physics events, but they are rare compared to soft interactions. For example, the production of a W boson through the annihilation of a quark-antiquark pair has a cross section of ~ 150 nb, that is 10^5 times smaller than the total inelastic pp cross section and the cross sections of one of the most interesting processes, like Higgs boson production, are 10^{11} times smaller, which underlines the strong importance of high luminosity and efficient background rejection techniques. The total cross section and the cross sections of some interesting hard processes are shown in figure 2.4.

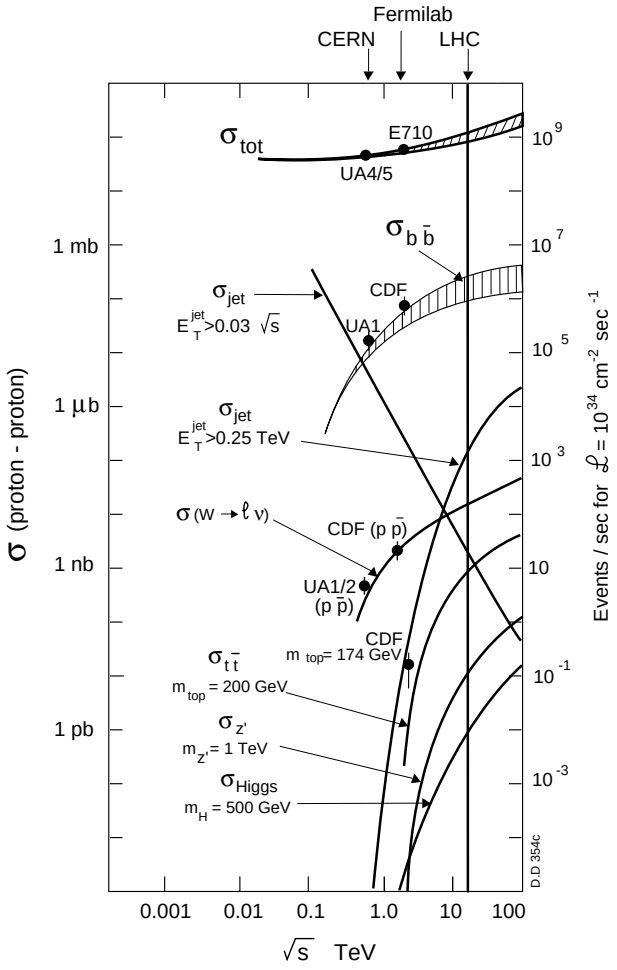

Figure 2.4: *The cross section for hard scattering processes versus centre-of-mass energy. The centre-of-mass energy of LHC is indicated at the top.*

In the hard scattering interactions of quarks and gluons at a hadron collider, the effective centre-of-mass energy of the process ($\sqrt{\hat{s}}$) is smaller than the centre-of-mass energy of the machine ($\sqrt{s} = 14\ TeV$) and is given by

$$\sqrt{\hat{s}} = \sqrt{x_a x_b s} \tag{2.4}$$

where x_a and x_b (*Björken variables*) are the proton momentum fraction carried by the two colliding partons. If $x_a \approx x_b \approx x$ then the above relation becomes

$$\sqrt{\hat{s}} = x\sqrt{s}. \tag{2.5}$$

Therefore in order to produce a particle of 100 GeV mass, two quarks, or gluons, which carry only 1% of the proton momentum are needed ($x \sim 0.01$), whereas a particle of 5 TeV mass can only be produced if two partons with $x \sim 0.35$ interact. The momentum distributions of quarks and gluons inside the proton are called *parton distribution functions*. *Up* and *down* quarks contribute to the quantum numbers of the proton (*valence quarks*) and therefore they carry a large fraction of the proton momentum. Protons contain also gluons and other quarks, which form the so-called *"sea"* and which exhibit much smaller momenta. They are mainly produced by the gluon radiation from valence quarks, and by subsequent gluon splitting into quark-antiquark pairs. The parton momentum distribution depends on the 4-momentum exchanged in the interaction(Q^2). At large Q^2 values the interaction probes the short-distance structure of the protons, hence it has access to the *sea*. So the observed parton distribution functions are shifted towards small x value. For small Q^2 values, on the other hand, only the valence quarks are visible and the parton distribution functions peak at large x values.

The cross section of a generic hard-scattering interaction is given by

$$\sigma = \sum_{a,b} \int f_a(x, Q^2) f_b(x, Q^2) \hat{\sigma_{ab}}(x_a, x_b) dx_a dx_b \tag{2.6}$$

The inelastic cross section at LHC is about 100 mb (at high luminosity run), so an average of 25 soft interactions occur simultaneously at each bunch crossing, providing an event rate of $10^9\ Hz$. It means that the ATLAS detector, for example, will be traversed by about 1000 charged particles every 25 ns, in the pseudo rapidity region $|\eta| < 2.5$. So a hard scattering event produced during a bunch crossing has to be sorted out from a huge amount of additional soft particles.

LHC detectors should moreover have a response time fast enough to avoid the overlap of a large number of bunch crossing. The typical response time should be in the range of $20 \div 50$ ns, which corresponds to integrating over $1 \div 2$ bunch crossing and therefore summing $25 \div 50$ soft events on average. A fine detector granularity is also required in order to minimize the probability for particles from pile-up events to cross the same detector element. Finally the LHC detectors must be radiation resistant, because of the high particle flux arising from pp collisions. This flux, integrated over 10 years of operations, amounts to $10^{17}\ neutrons/cm^2$ and ? $photons/cm^2$. Such huge particle fluxes can damage the detector elements and lead to a reduction of performances.

2.2 LHC Experiments

In order the full discovery potential of LHC two general-purpose proton-proton experiments, *ATLAS* and *CMS*, three specialized experiments, *LHCb*, *ALICE* and *TOTEM* are going to be installed at the beam crossing (Figure 2.1).

ALICE (**A** **L**arge **I**on **C**ollider **E**xperiment) is an experiment specialized to heavy ion physics in Pb-Pb collisions with centre-of-mass energies at the PeV scale [4]. Figure 2.5-*d* shows a three dimensional view of the ALICE detector.

ATLAS (**A** **T**oroidal **L**HC **A**pparatu**S**) is a general-purpose experiment for the physics of the proton-proton collisions [5]. The most characteristic features of the detector is its magnet system: the inner detector will be placed inside a solenoid , while large superconducting air-core toroids consisting of independent coils will be arranged outside the calorimeters to provide the magnet field for muon spectroscopy. ATLAS is the detector on which this thesis is focused so it will be explained in greater detail in the next sections. Figure 2.5-*a* shows a three dimensional view of the ATLAS detector.

CMS (**C**ompact **M**uon **S**olenoid) is the other general-purpose experiment at the LHC [6]. Its basic design differs from ATLAS mainly in the uniform solenoidal magnetic field, provided by a single, large, superconducting solenoidal magnet (14 m long and 3 m inner radius), which covers the whole detector including the muon chambers. The strong field of 4 T leads to a compact design for the Muon Spectrometer without compromising the momentum resolution up to pseudorapidities[1] of 2.5. The detector will be 14 m high, 20 m long and will have a weight of $\sim$1210 3 *tons*. Figure 2.5-*b* shows a three dimensional view of the CMS detector.

TOTEM (**TOT**al and **E**lastic **M**easurement) is an experiment dedicated to measure the total pp cross section with the luminosity independent method and to study elastic scattering and diffractive dissociation [7]. It was proposed later in 1997; having received favourable consideration from the Research Board, a Technical Proposal was prepared in 1999 in which the CMS experiment was identified as the optimal host experiment (Figure 2.6).

LHCb is an experiment dedicated to B physics [8]. The aim of the experiment is to fully investigate CP violation in the B_d and B_s systems, and to possibly reveal new physics beyond the Standard Model.

[1] Pseudorapidity defines the detector region in the polar angle variable; see definition in Par. 2.4.1, Equation 2.7.

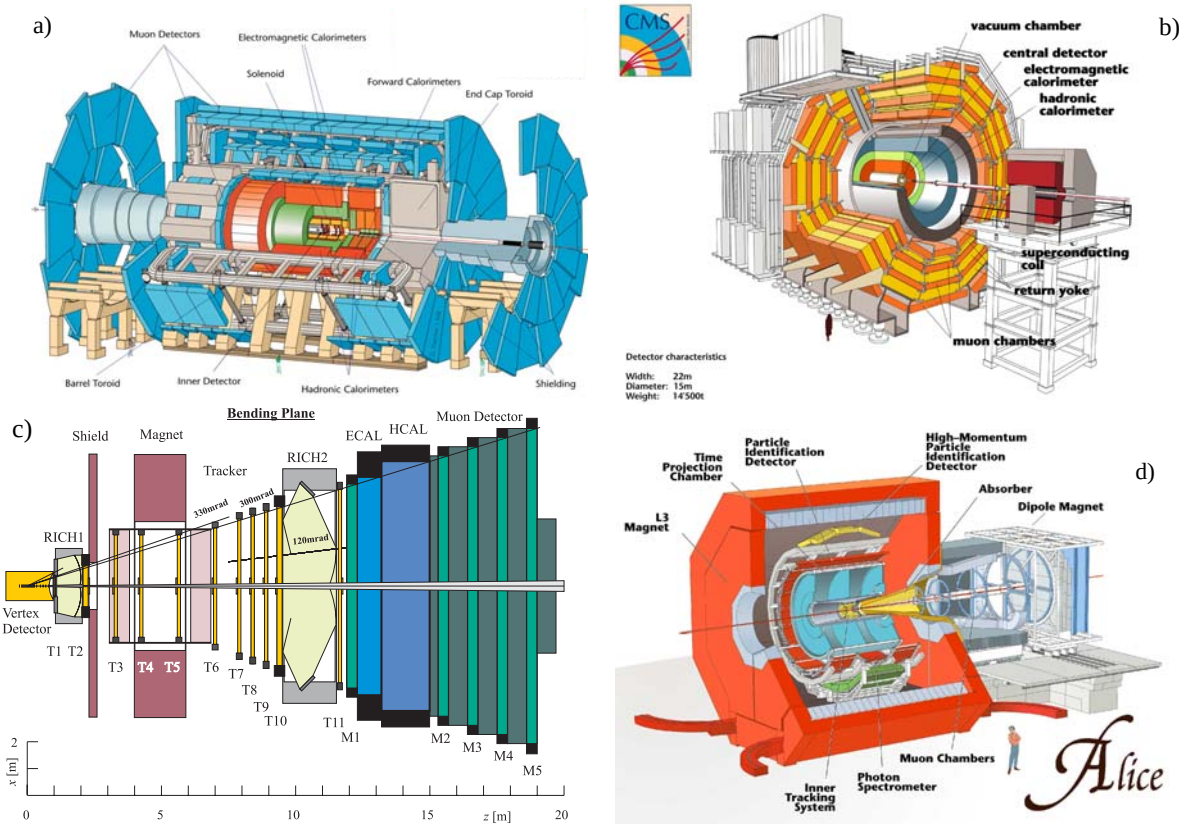

Figure 2.5: ***a)*** *Three dimensional view of the ATLAS experiment.* ***b)*** *Three dimensional view of the CMS experiment.* ***c)*** *Three dimensional view of the LHCb experiment.* ***d)*** *Three dimensional view of the ALICE experiment.*

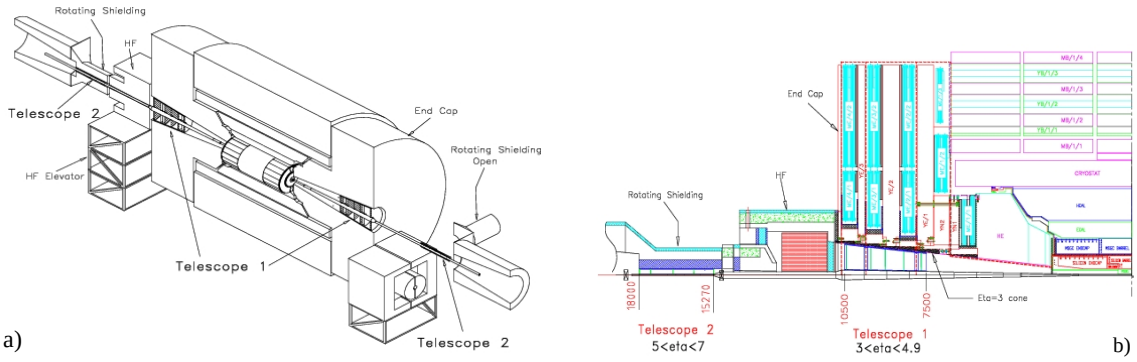

Figure 2.6: ***a)*** *Overall view of the CMS/TOTEM integration.* ***b)*** *Sketch of the CMS experimental apparatus showing the integration of the TOTEM telescopes.*

2.3 Physics at the LHC

The high energy and luminosity of the LHC offers a large range of physics opportunities, from the precise measurement of the properties of the known objects, to the exploration of the high energy frontier.

The main issue for the LHC is the search for the Standard Model (SM) Higgs boson or a family of Higgs bosons when considering The Minimal Supersymmetric extension of the Standard Model (MSSM). The new accelerator will allow the exploration of a mass range from $\sim$100 GeV, which is the current lower bound, up to TeV scale. Searches for Supersymmetry signals (detecting supersymmetric particles) or tests of alternative models are the second physics goal of LHC project, while the very large statistics of events will make possible also precision measurements on electroweak, heavy flavours and QCD physics. Nevertheless, limiting factors exist for physics at a pp collider, like for example event pile-up. The event rate at LHC is dominated by QCD jet production. Since the cross section of QCD processes grows faster with the centre-of-mass energy than the electroweak one, signal-to-background ratios are extremely low. For example the production cross section of jets with transverse momentum above 700 GeV is five orders of magnitude larger than the cross section for a Higgs boson of mass 150 GeV. Therefore it is obvious impossible to detect a Higgs boson decaying into jets at LHC, since such final states are overwhelmed by the much larger jet rate.

2.3.1 The ATLAS Physics Programme

The ATLAS physics programme, discussed in the Letter of Intent [9] and in the Technical Proposal [5] for the first time, have guided the detector optimization procedure.

• *Higgs boson search.* The most challenging signatures were used as benchmark processes for the setting of parameters that describe the detector performance. High-resolution measurements of electrons, photons and muons, excellent secondary vertex detection for τ-leptons and b-quarks, high-resolution calorimetry for jets and missing transverse energy are essential to explore the full range of possible Higgs boson masses.

• *Supersymmetry search.* Searches for SUSY set the benchmarks on the hermeticity and the missing transverse energy capability of the detector, as well as on b-tagging at high luminosity.

• *New heavy gauge bosons search.* Searches for new heavy gauge bosons provided benchmark requirements for high-resolution lepton measurements and charge identification in the p_T range as large as a few TeV.

• *Quark structure search.* Signatures characteristic for quark compositness set the requirements for the measurement of very high-p_T jets.

• *SM precision measurements.* The precision measurements of the W and top quark masses, gauge boson couplings, CP violation and determination of the Cabibbo-Kobayashi-Maskawa unitary triangle yielded benchmarks that address the need to precisely control the energy scale for jets and leptons, determine precisely secondary vertexes, reconstruct fully final states with relatively low-p_T particles and trigger on low-p_T leptons.

2.4 The ATLAS Detector: an Overview

The ATLAS detector, as most collision detectors, it is built in layers around the particle interaction point. Figure 2.7 shows a three dimension overview on the whole ATLAS detector. The detector will be a cylinder with a diameter of 22 m and a length of 44 m and will have a weight of $\sim 6 \cdot 10^3$ *tons*. The central part is commonly referred to as "*barrel*", the two outer circular sections as "*endcaps*".

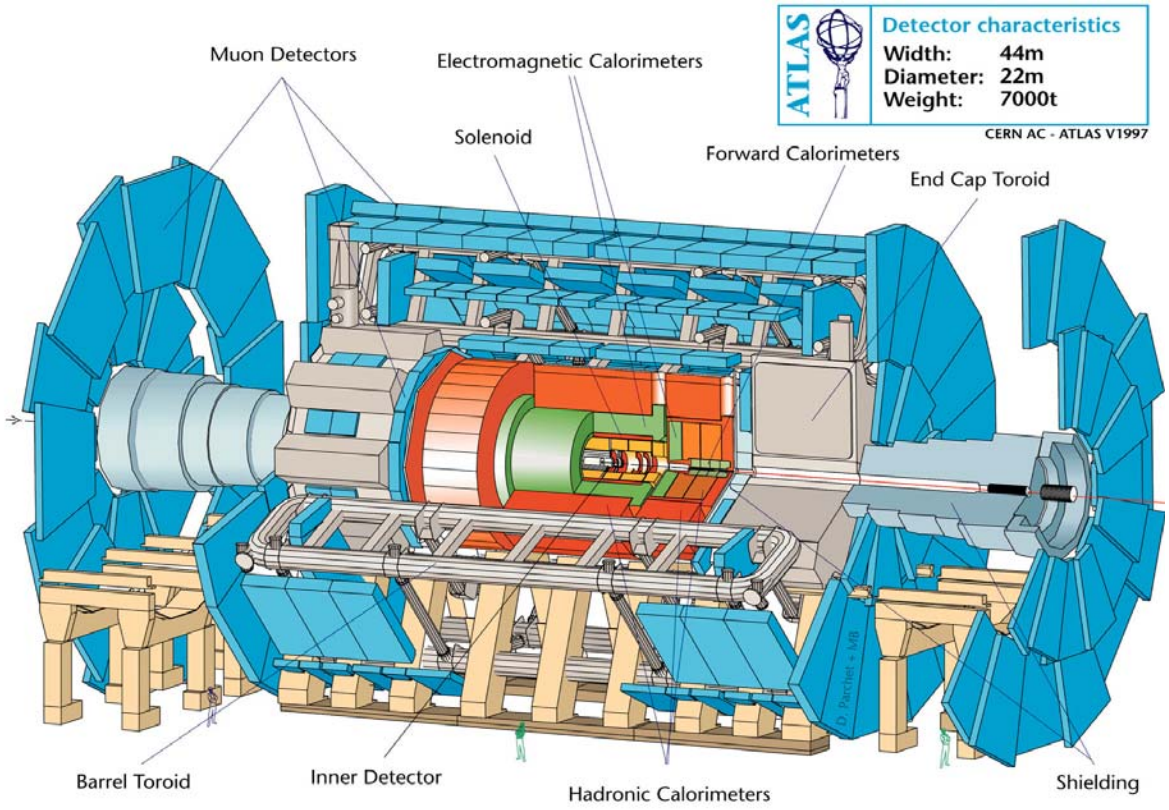

Figure 2.7: *Overall layout of the ATLAS detector.*

2.4.1 Names and conventions

The beam direction defines the z-axis, and the x-y plane is the plane transverse to the beam direction. The positive x-axis is defined as pointing from the interaction point to the centre of the LHC ring, and the positive y-axis is pointing upwards. The azimuthal angle ϕ is measured around the beam axis, and the polar angle θ is the angle from the beam axis. The pseudorapidity is defined as

$$\eta = -\ln tan(\theta/2). \tag{2.7}$$

The transverse momentum p_T and the transverse energy E_T, as well as the missing trans-

verse energy E_T^{miss} and other transverse variables, are defined in the x-y plane unless stated otherwise. The distance in the pseudorapidity-azimuthal angle space is defined as

$$\Delta R = \sqrt{\Delta^2\eta + \Delta^2\phi}. \tag{2.8}$$

Trajectories of charged particles can be described by five helix parameters in an ideal uniform magnetic field. The following helix parametrization in ATLAS, with all quantities measured at the point of closest approach to the nominal beam axis $x = 0$, $y = 0$. Parameters in x-y plane are:

$1/p_T$ - Reciprocal of the transverse momentum with respect to the beam axis.

ϕ - Azimuthal angle, where $\tan\phi = p_y/p_x$.

d_0 - Transverse impact parameter, defined as the transverse distance to the beam axis at the point of closest approach; signed according to the reconstructed angular momentum of the track about the axis.

Parameter in the R-z plane are:

$\cot\theta$ - Cotangent of the polar angle, where $\cot\theta = p_z/p_T$.

z_0 - Longitudinal impact parameter, defined as the z position of the track at the point of closest approach.

2.4.2 The Inner Detector

The Inner Detector [10] is the ATLAS subdetector located closest to the beam pipe and it it obtained in the Central Solenoid magnet which provides a central field of 2 T. Its main purposes are the reconstruction of very short-lived particles, the search for secondary vertexes and the determination of the exact position of the interaction point. The Inner Detector layout is shown in figure 2.8.

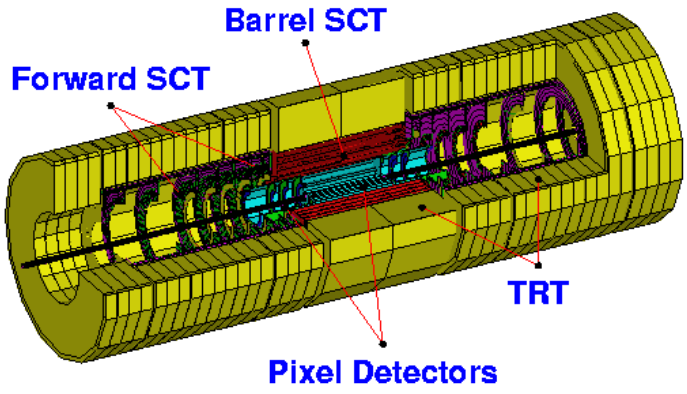

Figure 2.8: *A three dimensional view of the ATLAS Inner Detector.*

Mechanically the Inner Detector consists of three units: a barrel part extending over ± 80

cm, and two identical endcaps covering the rest of the cylindrical cavity. The Inner Detector combines high-resolution elements in the inner part, contained within a radius of 56 cm, with continuous tracking elements in the outer part, combining three different technologies: silicon pixel detectors closest to the beam pipe, surrounded by the SemiConductor Tracker (SCT) and the Transition Radiation Tracker (TRT) in the outer part. The general support and service region is located at the outermost radius. In the barrel region the high-precision detector layers are arranged on concentric cylinders around the beam axis. The pixel layers are segmented in $R\phi$ and z, while the SCT detectors uses small angle stereo strips to measure both coordinates. The barrel TRT straw tubes are parallel to the beam direction. All the endcap tracking elements are located in panes perpendicular to the beam axis. The strip detectors have one set of strips running radially and a set of stereo strips at an angle of 40 $mrad$. The continuous tracking consists of radial straws arranged into wheels. The combination of these technologies gives very robust pattern recognition.

Pixel Detector

The pixel detector [11] is designed to provide a very high-granularity, high-precision set of measurements as close to the interaction point as possible. The system provides three precision measurements over the full acceptance, and it mostly determines the impact parameter resolution and the ability of the Inner Detector to find short-lived particles such as B-mesons and τ leptons. The two-dimensional segmentation of the sensors gives space points without any of the ambiguities associated with crossed strip geometries, but it requires the use of advanced electronic techniques. In addition the electronic elements must be radiation hardened to withstand over 300 kGy of ionizing radiation and over $5{\cdot}10^{14}$ neutrons per cm^2 over ten years of operation. The system contains 140 million detector elements, each 50 μm in the $R\phi$ and 300 μm in z.

Semiconductor Tracker

The SCT system is designed to provide eight precision measurements per track in the intermediated radial range, contributing to the measurement of momentum, impact parameter and vertex position, as well as providing pattern recognition by the use of high granularity. The barrel SCT is made of eight layers of silicon microstrip detectors to provide precision points in the $R\phi$ and z coordinates, using small angle stereo to obtain the z measurement. The detector contains 61 m^2 of silicon strips, with a pitch of 80 μm, for a total of 6.2 million readout channels. The spatial resolution is 16 μm in $R\phi$ and 580 μm in z, per module containing one $R\phi$ and one stereo measurement. Tracks can be distinguished if separated by more than $\sim$ 200 μm.

Transition Radiation Tracker

The TRT system consists of 420,000 proportional drift tubes with a diameter of 4 mm. It is divided into a barrel part and several forward wheels. The detector is operated with

$Xe : CF_4 : CO_2$ gas mixture. The TRT is based on the use of straw detectors, which can be operate at very high rates expected at the LHC. Straw tubes are small diameter ionization detectors which use the principle of gas amplification near a thin anode wire to produce a visible signal from a small primary ionization. The TRT contributes significantly to the electron pion separation capability of ATLAS at low energies, in fact the intensity of transition radiation produced by a particle crossing the boundary between two materials with different refractive indexes depends on its velocity, and thus it is different for particles of different rest mass. At the same time TRT provides additional track information for charged particle.

2.4.3 The Calorimeters

The ATLAS calorimetry ([12],[13] and [14]) consists of an electromagnetic calorimeter covering the pseudorapidity region $|\eta| < 3.2$, a hadronic barrel calorimeter covering $|\eta| < 1.7$, hadronic endcap calorimeters covering $1.5 < |\eta| < 3.2$, and forward calorimeters covering $3.1 < |\eta| < 4.9$. A three-dimensional view of the calorimeters are shown in figure 2.9. Electrons and photons are fully absorbed by the inner electromagnetic calorimeter; the hadron showers penetrate further are almost completely absorbed by the following layers of the hadronic calorimeters.

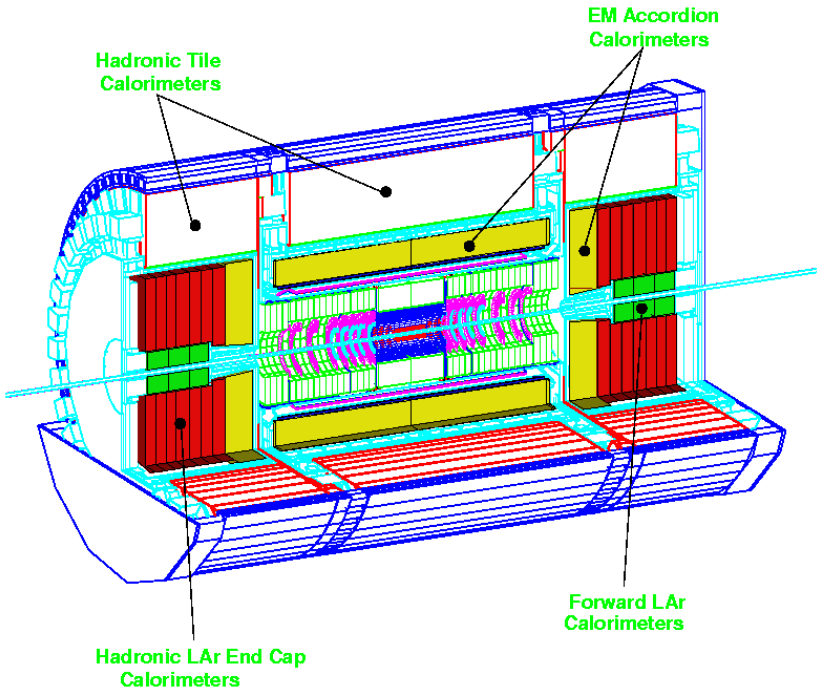

Figure 2.9: *A three dimensional view of the ATLAS Calorimeters.*

The Electromagnetic Calorimeter

The electromagnetic calorimeter is a lead/liquid-argon (LAr) detector with accordion-shaped Kapton electrodes and lead absorber plates over its full coverage. The accordion geometry provides complete ϕ symmetry. Over the pseudorapidity range $|\eta| < 1.8$, it is preceded by a presampler detector, installed immediately behind the cryostat cold wall, and used to correct for the energy lost in the material (Inner Detector, cryostats, coil) upstream of the calorimeter.

The barrel electromagnetic calorimeter is contained in a barrel cryostat, which surrounds the Inner Detector cavity. The solenoid which supplies the 2 T magnetic field to the Inner Detector is integrated into the vacuum of the barrel cryostat and is placed in front of the electromagnetic calorimeter. Two end-cap cryostats house the end-cap EM and hadronic calorimeters, as well as the integrated forward calorimeter. The barrel and extended barrel tile calorimeters support the LAr cryostats and also act as the main solenoid flux return.

The lead thickness in the absorber plates has been optimized as a function of η in terms of energy resolution. The LAr gap has a constant thickness of 2.1 mm in the barrel. In the end-cap, the shape of the Kapton electrodes and lead converter plates is more complicated, because the amplitude of the accordion waves increases with radius. The absorbers have constant thickness, and therefore the LAr gap also increases with radius. The total thickness of the electromagnetic calorimeter is > 24 radiation lengths (X_0) in the barrel and $> 26\%$ X_0 in the end-caps.

Over the region devoted to precision physics ($|\eta| < 2.5$), the electromagnetic calorimeter is segmented into three longitudinal sections. The strip section, which has a constant thickness of $\sim 6\ X_0$ (upstream material included) as a function of η, is equipped with narrow strips with a pitch of $\sim 4\ mm$ in the η direction. This section acts as a 'preshower' detector, enhancing particle identification and providing a precise position measurement in η. The middle section is transversally segmented into square towers of size $\Delta\phi \times \Delta\eta = 0.025 \times 0.025$. The total calorimeter thickness up to the end of the second section is $\sim 24\ X_0$, tapered with increasing rapidity. The back section has a granularity of 0.05 in η and a thickness varying between 2 X_0 and 12 X_0. For $|\eta| > 2.5$, i.e. for the end-cap inner wheel, the calorimeter is segmented in two longitudinal sections and has a coarser lateral granularity than for the rest of the acceptance. The calorimeter cells point towards the interaction region over the complete η-coverage. The total number of channels is ~ 190000.

The Hadronic Calorimeter

The hadronic barrel calorimeter is a cylinder divided into three sections: the central barrel and two identical extended barrels. It is based on a sampling technique with plastic scintillator plates (tiles) embedded in an iron absorber [reference]. At larger pseudorapidities, where higher radiation resistance is needed, the intrinsically radiation-hard LAr technology is used for all the calorimeters: the hadronic endcap calorimeter, a copper LAr detector with parallel-plate geometry, and the forward calorimeter, a dense LAr calorimeter with rod-shaped electrodes in a tungsten matrix.

An important parameter in the design of the hadronic calorimeter is its thickness: it

has to provide good containment for hadronic showers and reduce punch-through into the muon system to a minimum. The total thickness is 11 interaction lengths (λ) at η =0, including about 1.5 λ from the outer support, which has been shown both by measurements and simulation to be sufficient to reduce the punch-through well below the irreducible level of prompt or decay muons. Close to 10 λ of active calorimeter are adequate to provide good resolution for high energy jets. Together with the large η -coverage, this will also guarantee a good E_T^{miss} measurement, which is important for many physics signatures and in particular for SUSY particle searches.

The large hadronic barrel calorimeter, Tile Calorimeter, is a sampling calorimeter using iron as the absorber and scintillating tiles as the active material. The tiles are placed radially and staggered in depth. The structure is periodic along z. The tiles are 3 mm thick and the total thickness of the iron plates in one period is 14 mm. Two sides of the scintillating tiles are read out by wavelength shifting fibers into two separate photomultipliers. The tile calorimeter is composed of one barrel and two extended barrels. Radially the tile calorimeter extends from an inner radius of 2.28 m to an outer radius of 4.25 m. It is longitudinally segmented in three layers, approximately 1.4, 4.0 and 1.8 interaction lengths thick at η =0. Azimuthally, the barrel and extended barrels are divided into 64 modules. In η, the readout cells, built by grouping fibers into a photomultipliers, are 'pseudo-projective' towards the interaction region. The resulting granularity is $\Delta\eta \times \Delta\phi$ =0.1 $\times$ 0.1 (0.2 $\times$ 0.1 in the last layer). The total number of channels is about 10000. The calorimeter is placed behind the electromagnetic calorimeter ($\approx$ 1.2 λ) and the solenoid coil. The total thickness at the outer edge of the tile-instrumented region is 9.2 λ at η =0.

2.4.4 The Muon Spectrometer

High-momentum final-state muons are the most promising and robust signatures of physics at the Large Hadron Collider. To exploit this potential,a high-resolution muon spectrometer with stand-alone triggering and momentum measurement capability over a wide range of transverse momentum, pseudorapidity, and azimuthal angle has been designed.

The Muon Spectrometer [15] is based on the magnetic deflection of muon tracks in the large superconducting air-core toroid magnets, it is instrumented with separate trigger and high-precision tracking chambers. Over the range $|\eta| < 1.0$, magnetic bending is provided by the large barrel toroid. For $1.4 < |\eta| < 2.7$, muon tracks are bent by two smaller endcap magnets inserted into both ends of the barrel toroid. Over $1.0 < |\eta| < 1.4$, usually referred to as the transition region, magnetic deflection is provided by a combination of barrel and endcap fields. This magnetic configuration provides a field that is mostly orthogonal to the muon trajectories, while minimizing the degradation of resolution due to the multiple scattering.

The Muon Spectrometer forms the outer shell of the ATLAS detector and occupies by far the largest part of its volume (Figure 2.10). It is located on the outside of the calorimeter modules and it covers the space between approximately 4.5 m and 11 m in radius and 7 m and 23 m longitudinally on both sides of the interaction point. The total volume is approximately 16000 m^3. In the barrel the muon chambers are arranged in three concentric cylinders around the beam axis. The endcap chambers form four disks on each side of the interaction point,

concentric around the beam axis.

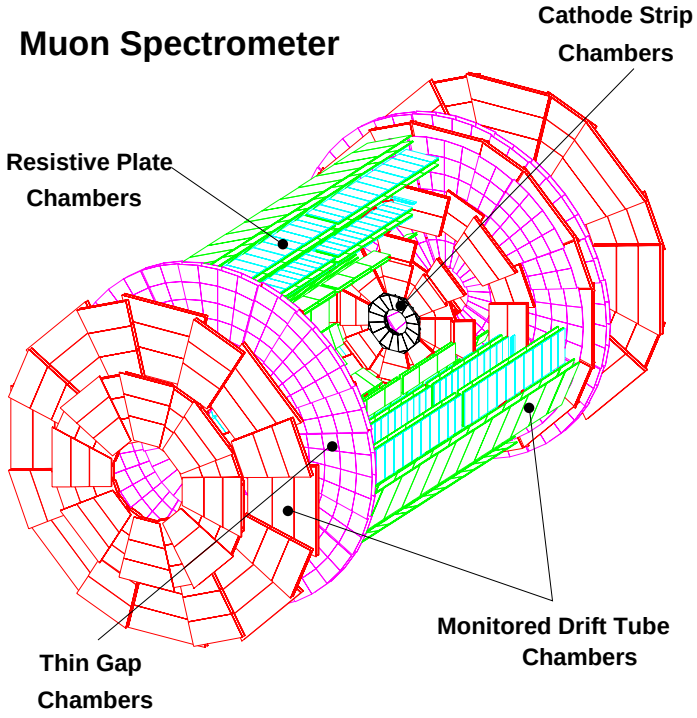

Figure 2.10: *A three dimensional view of the ATLAS muon system, indicating where the different chamber technologies are used.*

The two separate system with distinct functionality used are:

- *Trigger:* Resistive Plate Chambers (RPC) in the barrel region and Thin Gap Chambers (TGC) for the endcap covering the spectrometer acceptance up to $|\eta| = 2.4$ (Figure 2.19). Both types of chambers generate fast signals with a time resolution of a few nanoseconds which are used for level-1 triggering and bunch crossing identification. And they have a spatial resolution of 5-20 mm, it is used in the pattern recognition algorithm and provides the only measurement of the track coordinate in the non bending plane.
- *Precision measurement:* Monitored Drift Tube chambers (MDT) for 99.5 % of the area and Cathode Strip Chambers (CSC) for the remaining (Figure 2.12), a very small forward area where particle fluxes are highest. Although small in physical size, this area covers a large range in pseudorapidity ($2.0 < |\eta| < 2.7$). The precision chambers measure the track coordinates in the bending plane with high precision. For the MDTs no information on the non bending coordinate and on the bunch crossing time is available. The CSCs, however, do measure both quantities.

An optical alignment system have been designed to meet the stringent requirements on the mechanical accuracy and the survey of the precision chambers.

A brief overview of the different muon spectrometer chambers and of the alignment system is given now, except for the MDT, whose details are given in the next chapter (Chp. 3).

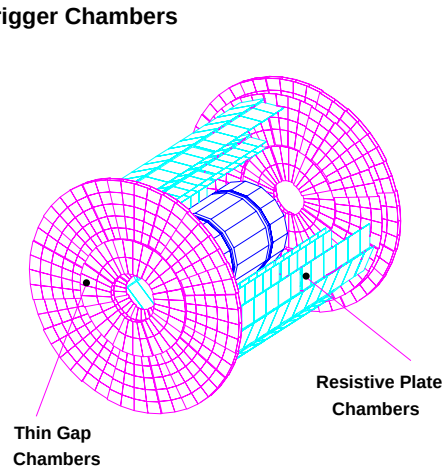

Figure 2.11: *A three dimensional view of the trigger chambers of the muon system.*

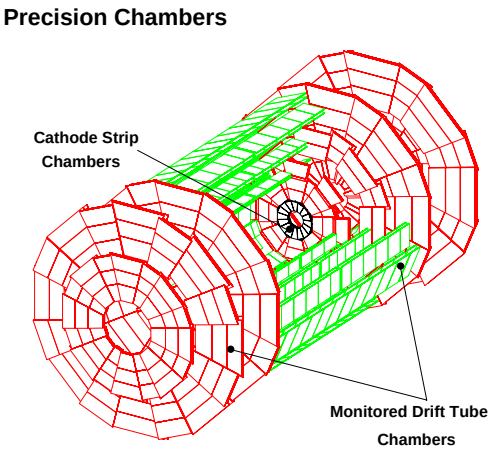

Figure 2.12: *A three dimensional view of the precision chambers of the muon system.*

Resistive Plate Chambers

The RPC is a gaseous detector providing a typical space-time resolution of 1 $cm \cdot 1\ ns$ with digital readout. The basic RPC unit is a narrow gas gap formed by two parallel resistive Bakelite plates, separated by insulating spacers. The primary ionization electrons are multiplied into avalanches by a high, uniform electric field of typically 4.5 kV/mm. The gas mixture is based on tetrafluoroethane ($C_2H_2F_4$) with some small admixture of SF_6, a non-flammable and environmentally safe gas that allows for a relatively low operating voltage. The signal is read out via capacitive coupling by metal strips on both sides of the detector. A trigger chamber is made from two rectangular detector layers, each one read out by two orthogonal series of pick-up strips: the 'η strips' are parallel to the MDT wires and provide the bending view of the trigger detector; the 'ϕ strips', orthogonal to the MDT wires, provide the second-coordinate measurement which is also required for the offline pattern recognition.

The RPC use no wires and therefore have a simple mechanical structure and are straightforward to manufacture. Each chamber is made from two detector layers and four readout strip panels. To preserve the excellent intrinsic time resolution of the RPCs, the readout strips are optimized for good transmission properties and they are terminated at both ends to avoid signal reflections.

Thin Gap Chambers

The TGCs are similar in design to multiwire proportional chambers, with the difference that the anode wire pitch is larger than the cathode-anode distance. Signals from the anode wires,

arranged parallel to the MDT wires, provide the trigger information together with readout strips arranged orthogonal to the wires. These readout strips are also used to measure the second coordinate. The TGCs operated with a highly quenching gas mixture of 55 % CO_2 and 45 % n-pentane ($n-C_5H_{12}$); the total gas volume is 16 m^3 and this gas mixture is highly inflammable and so it requires adequate safety precautions. The TGCs are constructed in doublets and in triplets of chambers.

The electric field configuration and the small wire distance provide for a short drift time and thus a good time resolution. Ageing properties of the chambers have been investigated in detail and were found to be fully adequate for the expected operating conditions at the LHC.

Cathode Strip Chambers

The CSCs are multiwire proportional chambers with cathode strip readout and with a symmetric cell in which the anode-cathode spacing is equal to the anode wire pitch. The precision coordinate is obtained by measuring the charge induced on the segmented cathode by the avalanche formed on the anode wire. Good spatial resolution is achieved by segmentation of the readout cathode and by charge interpolation between neighbouring strips. The cathode strips for the precision measurement are orthogonal to the anode wires. Important characteristics are small electron drift times (30 ns), good time resolution (7 ns), good two-track resolution, and low neutron sensitivity. A measurement of the transverse coordinate is obtained from orthogonal strips, which are oriented parallel to the anode wires. The baseline CSC gas is a non-flammable mixture of 80 % Ar, 20 % CO_2, with a total volume of 1.1 m^3. The fact that this gas contains no hydrogen, combined with the small gap width, explains the low sensitivity to neutron backgrounds.

Alignment System

Due to the large size of the muon system, relative chamber movements with respect to each other of up to several millimeters can be expected when the toroid magnet is switched on or as a consequence of temperature variations.
The optimum performance of the muon spectrometer can only be reached if the relative positions of the chambers along the track of a muon is known to a precision better than the intrinsic chamber resolution. The chamber alignment is therefore of prime importance. Due to the large dimensions of the spectrometer no attempt is made to actively re-align the chambers to the required precision. Instead the relative positions of the chambers within projective towers of chambers are monitored by means of optical alignment systems and the position information is used to correct the measured track coordinates in the offline analysis.

All alignment systems are based on optical straightness monitors. Owing to geometrical constraints, different schemes (see Figure 2.13 and 2.14) are used to monitor chamber positions in the barrel, in the end-cap, and the deformations of large chambers ('in-plane alignment').

For reasons of cost, optical monitoring in the barrel is foreseen only for the large sectors of chambers. Chambers in the small sectors are aligned with particle tracks, exploiting the

overlap with chambers in the large sectors. Alignment with tracks will also serve to cross-calibrate the optical survey of the large sectors.

Very high accuracy is required only for the positioning of chambers within a projective tower. The accuracy required for the relative positioning of different towers to obtain adequate mass resolutions for multimuon final states is in the millimeter range. This accuracy is easily achieved by the initial positioning and survey of chambers at installation time. The relative alignment of muon spectrometer, calorimeters and inner detector will rely on high-momentum muon trajectories.

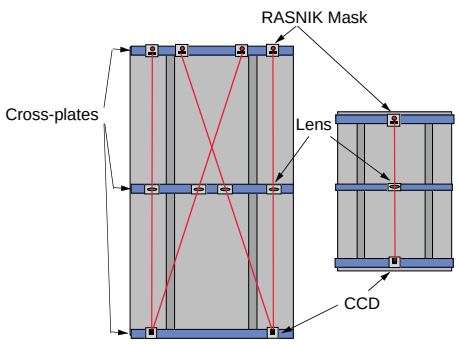

Figure 2.13: *Sketch of the in-plane alignment system with four light rays for a large MDT chamber (on the left) and one light ray for a small chamber (on the right).*

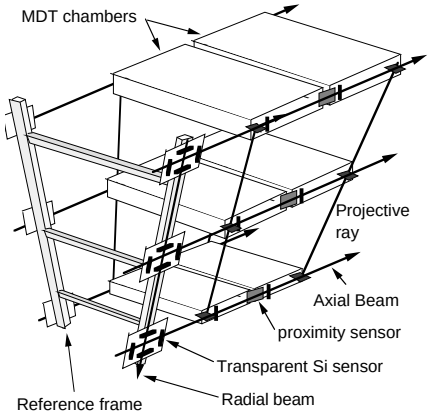

Figure 2.14: *Principle sketch of the axial alignment system.*

2.4.5 The Magnetic System

One of the prominent features of the ATLAS detector is its large magnetic system. The ATLAS superconducting magnet system [16] is an arrangement of a central solenoid (CS) providing the Inner Detector with magnetic field, surrounded by a system of three large air-core toroids (Figure 2.15) generating the magnetic field for the Muon Spectrometer.

The overall dimensions of the magnet system are 26 m in length and 20 m in diameter. The two endcap toroids (ECT) are inserted in the barrel toroid (BT) at each end and line up with the CS. They have a length of 5 m, an outer diameter of 10.7 m and an inner bore of 1.65 m. The CS extends over a length of 5.3 m and has a bore of 2.4 m. The unusual configuration and large size make the magnet system a considerable challenge requiring careful engineering.

The CS provides a central field of 2 T with a peak magnetic field of 2.6 T at the superconductor itself. The peak magnetic fields on the superconductors in the BT and ECT are 3.9 and 4.1 T respectively. The performance in terms of bending power is characterized by the field integral $\int Bdl$, where B is the azimuthal field component and the integral is taken on a

straight line trajectory between the inner and outer radius of the toroids. The BT provides 2 to 6 Tm and the ECT contributes with 4 to 8 Tm in the 0.0-1.3 and 1.6-2.7 pseudorapidity ranges respectively. The bending power is lower in the transition regions where the two magnets overlap ($1.3< |\eta| < 1.6$).

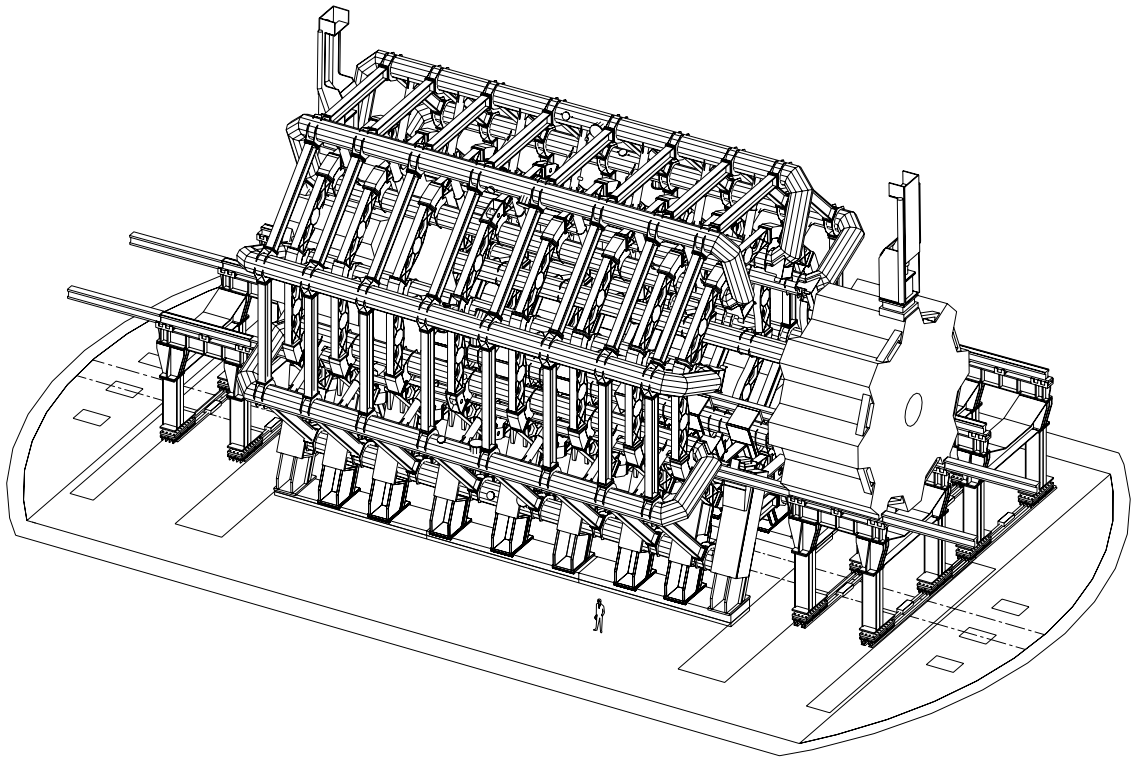

Figure 2.15: *A three dimensional view of the ATLAS Magnetic System.*

Each of the three toroids consists of eight coils assembled radially and symmetrically around the beam axis. The ECT coil system is rotated by 22.5° with respect to the BT coil system in order to provide radial overlap and to optimize the bending power in the interface regions of both coil systems (Figures 2.16 and 2.17).

The magnets are indirectly cooled by forced flow of helium at 4.5 K through tubes welded on the casing of the windings.

2.4.6 The Trigger Scheme and the Data Acquisition System

The ATLAS trigger and data-acquisition (DAQ) system is based on three levels of online event selection ([17],[18] and [19]). Each trigger level refines the decisions made at the previous level and, where necessary, applies additional selection criteria. Starting from an initial bunch-

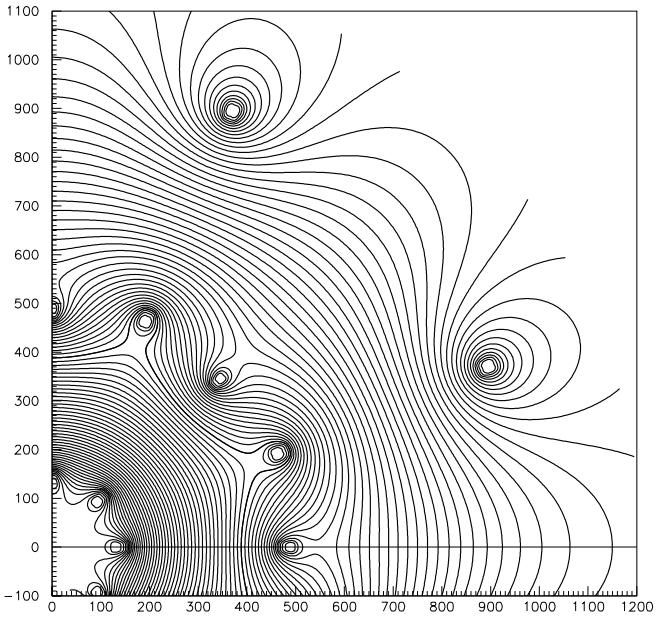

Figure 2.16: *Magnetic field map in the transition region. The field lines are shown in a plane perpendicular to the beam axis and located in the middle region of an endcap toroid. The interval separating consecutive lines is 0.1 Tm. Individual barrel and endcap coils are visible. The scales are in centimeters.*

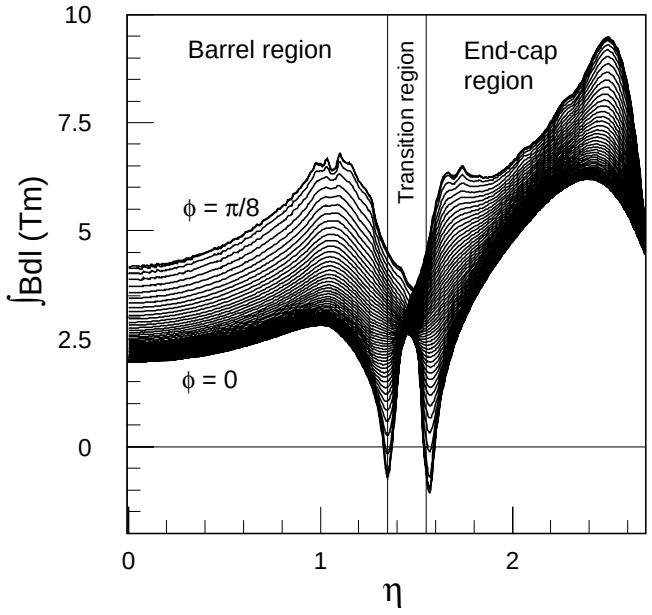

Figure 2.17: *Toroid bending power $\int Bdl$ of the azimuthal field component, integrated between the first and the last muon chamber, as a function of pseudorapidity. The curves correspond to azimuthal angles equally spaced between the barrel toroid and endcap toroid coil planes.*

crossing rate of 40 MHz (interaction rate of $\sim 10^9$ Hz at a luminosity of $10^{34} cm^{-2} s^{-1}$), the rate of selected events must be reduced to ~ 100 Hz for permanent storage. While this requires an overall rejection factor of 10^7 against 'minimum-bias' events, excellent efficiency must be retained for the rare new physics processes, such as Higgs boson decays, which will be searched for in ATLAS. Figure 4.15 shows a simplified functional view of the Trigger/DAQ system.

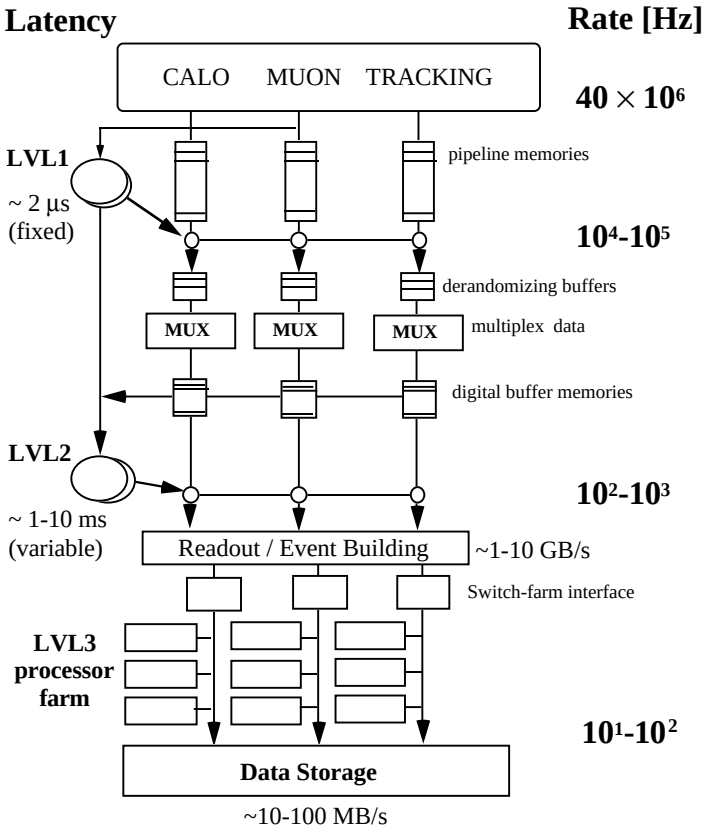

Figure 2.18: *Block diagram of the Trigger/DAQ system.*

The Level-1 Trigger

The level-1 (LVL1) trigger [17] makes an initial selection based on reduced-granularity information from a subset of detectors. High transverse-momentum (*high-p_T*) muons are identified using only the trigger chambers, RPCs in the barrel, and TGCs in the end-caps (Figure 2.19). The calorimeter selections are based on reduced-granularity information from all the calorimeters (EM and hadronic; barrel, end-cap and forward). Objects searched for by the calorimeter trigger are *high-p_T* electrons and photons, jets, and τ-leptons decaying into hadrons, as well as large missing and total transverse energies. The LVL1 trigger decision is based on combinations of objects required in coincidence or veto. Most of the physics requirements of ATLAS

can be met by using, at the LVL1 trigger level, fairly simple selection criteria of a rather inclusive nature. However, the trigger implementation is flexible and it can be programmed to select events using more complicated signatures.

The maximum rate at which the ATLAS front-end systems can accept LVL1 triggers is limited to 75 kHz (upgradable to 100 kHz). An essential requirement on the LVL1 trigger is that it should uniquely identify the bunch crossing of interest. Given the short (25 ns) bunch-crossing interval, this is a non-trivial consideration. In the case of the muon trigger, the physical size of the muon spectrometer implies times-of-flight comparable to the bunch-crossing period. For the calorimeter trigger, a serious challenge is that the pulse shape of the calorimeter signals extends over many bunch crossings.

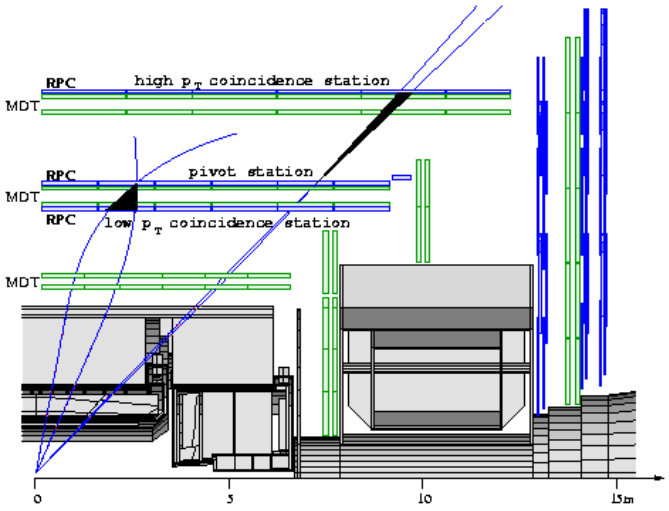

Figure 2.19: *Level-1 muon trigger scheme. A low-p_t trigger ($p_t > 6$ GeV) requires a coincidence of hits in two trigger chambers while for a high-p_t trigger ($p_t > 20$ GeV) hits in 3 planes are needed.*

It is important to keep the LVL1 latency (time taken to form and distribute the LVL1 trigger decision) to a minimum. During this time, information for all detector channels has to be conserved in 'pipeline' memories. Events selected by LVL1 are read out from the front-end electronics systems of the detectors into readout drivers (RODs) and then into readout buffers (ROBs). All the detector data for the bunch crossing selected by the LVL1 trigger are held in the ROBs, either until the event is rejected by the level-2 (LVL2) trigger (in which case the data are discarded), or, in case the event is accepted by LVL2, until the data have been successfully transferred by the DAQ system to storage associated with the Event Filter (EF), which makes the third level of event selection. The process of moving data from the ROBs to the EF is called event building. Whereas before event building each event is composed of many fragments, with one fragment in each ROB, after event building the full event is stored in a single memory accessible by an EF processor.

The Level-2 Trigger

The LVL2 trigger makes use of 'Region-of-Interest' (RoI) information provided by the LVL1 trigger. This includes information on the position and P_T of candidate objects, and energy

sums. The RoI data are sent by LVL1 to LVL2, for all events selected by the LVL1 trigger, using a dedicated data path. Using the RoI information, the LVL2 trigger selectively accesses data from the ROBs, moving only the data that are required in order to make the LVL2 decision. The LVL2 trigger has access to all of the event data, if necessary with the full precision and granularity. However, typically only data from a small fraction of the detector, corresponding to limited regions centered on the objects indicated by the LVL1 trigger, are needed by the LVL2 trigger. Hence, usually only a few per cent of the full event data are required thanks to this RoI mechanism. It is expected that LVL2 will reduce the rate to $\sim$ 1 kHz. The latency of the LVL2 trigger is variable from event to event and it is expected to be in the range 1-10 ms.

In the case of muon triggers, the rejection power at LVL2 comes from sharpening (and, where necessary, raising) the P_T threshold compared to LVL1, and from applying isolation requirements. Sharper P_T thresholds are obtained by using the precision muon chambers and the ID. The isolation requirements use the calorimeter information in a region around the muon candidate.

The High-Level Trigger

After LVL2, the last stage of the online selection is performed by the EF. It will employ offline algorithms and methods, adapted to the online environment, and use the most up to date calibration and alignment information and the magnetic field map. The EF will make the final selection of physics events which will be written to mass storage for subsequent full offline analysis. The output rate from LVL2 should then be reduced by an order of magnitude, giving $\sim 100\ Hz$, corresponding to an output data rate of $\sim 100\ MB/s$ if the full event data are to be recorded.

2.5 Summary

In this chapter the Large Hadron Collider (LHC) project was introduced and the ATLAS detector and its subsystems were described in some detail.

The LHC is a proton-proton collider at a centre-of-mass energy $\sqrt{s} = 14\ TeV$ with a design luminosity of $10^{34}\ cm^{-2}s^{-1}$. The collider will have a second period of runs with heavy-ion collisions with a centre-of-mass energy of 1148 TeV. Once in operation it will allow to explore new physics at the TeV scale and to perform detailed Standard Model studies.

At four interaction regions along the LHC ring, the protons bunches will collide against each other. Around these collision points, four experiments are being constructed, among which ATLAS (A Toroidal LHC ApparatuS), that is a general purpose 4π detector.

Bibliography

[1] *ATLAS Collaboration*, ***ATLAS Detector and Physics Performance Technical Design Report***, CERN/LHCC 99-14 and 99-15, 1994.

[2] *O. S. Brüning et al.*, ***LHC Design Report***, CERN-2004-003-V1/V2/V3, 2004.

[3] *F. Gianotti*, ***Collider Physics: LHC***, CERN Yellow-Report 2000-007, Proceeding of 1999 European School of High Energy Physics, Casta-Papiernicka, Slovak Republic, 2000.

[4] *ALICE Collaboration*, ***ALICE Technical Proposal***, CERN/LHCC 95-71, 1995.

[5] *ATLAS Collaboration*, ***ATLAS: Technical Proposal for a General-Purpose pp Experiment at the Large Hadron Collider at CERN***, CERN/LHCC 94-43, 1994.

[6] *CMS Collaboration*, ***CMS Technical Proposal***, CERN/LHCC 94-38, 1994.

[7] *TOTEM Collaboration*, ***TOTEM Technical Proposal***, CERN, 1999.

[8] *LHCb Collaboration*, ***LHCb Technical Proposal***, CERN/LHCC 98-4, 1998.

[9] *ATLAS Collaboration*, ***ATLAS Letter of Intent***, CERN/LHCC 92-4, 1992.

[10] *ATLAS Collaboration*, ***Inner Detector Technical Design Report***, CERN/LHCC 97-16 and 97-17, 1997.

[11] *ATLAS Collaboration*, ***Pixel Detector Technical Design Report***, CERN/LHCC 98-13, 1998.

[12] *ATLAS Collaboration*, ***Calorimeter Performance Technical Design Report***, CERN/LHCC 96-40, 1996.

[13] *ATLAS Collaboration*, ***Liquid Argon Calorimeter Technical Design Report***, CERN/LHCC 96-41, 1996.

[14] *ATLAS Collaboration*, ***Tile Calorimeter Technical Design Report***, CERN/LHCC 96-42, 1996.

[15] *ATLAS Collaboration*, ***Muon Spectrometer Technical Design Report***, CERN/LHCC 97-22, 1997.

[16] *ATLAS Collaboration*, ***Magnet System Technical Design Report***, CERN/LHCC 97-18, 1997.

[17] *ATLAS Collaboration*, ***First-Level Trigger Technical Design Report***, CERN/LHCC 98-14, 1998.

[18] *ATLAS Collaboration*, ***DAQ, EF, LVL2 and DCS Technical Progress Report***, CERN/LHCC 98-16, 1998.

[19] *ATLAS Collaboration*, ***Trigger Performance Status Report***, CERN/LHCC 98-15, 1998.

Chapter 3

The Atlas Monitored Drift Tubes

In this chapter some more information about the Muon Spectrometer are reported and the Monitored Drift Tube Chambers are presented [1]. The working principle of drift tubes is discussed. The background conditions expected at the LHC are also reported.

3.1 The MDT Chambers

The Monitored Drift Tube Chambers perform the precision coordinate measurement in the bending direction of the air-core toroidal magnet and therefore provide the muon momentum measurement. They cover almost the entire area of 5500 m^2 which is needed for a good momentum determination of the muons at $|\eta| < 2.7$. In the innermost plane of the two endcaps, where the background is highest, they are replaced by CSC (as described in Par. 2.4.4).

The muon spectrometer is designed to perform measurements with a momentum resolution $\Delta p/p < 1 \cdot 10^{-4} \times p/GeV$, for $p_T >$ 300 GeV; at smaller momenta the resolution is limited to a few percent by multiple scattering in the magnet and the detector structure, and by energy loss fluctuations in the calorimeters. To achieve this resolution by a three-point measurement, with the size and bending power of the ATLAS toroids, each point must be measured with an accuracy better than 50 μm. This sets the scale for the requirements on the intrinsic resolution, the mechanical precision, and the survey accuracy of the muon chambers. The coordinates of of a muon track in the plane of the layer and in the direction across the tubes are determined by registering the drift times of the ionization electrons in the gas; this results in a measurement of effectively one coordinate with 40 μm precision. To obtain such precision with a lightweight construction the chambers are assembled on their support or 'spacer' frame using precision mechanics during production. Their deformations are monitored by built-in optical systems once they have left the flat granite table on which they have been assembled. This explains the "Monitored" of the MDTs.

The chamber design must guarantee reliability and stability of construction and operation for the foreseen lifetime of the experiment in an high background environment.

3.1.1 Name and Convections

To facilitate the orientation within the Muon Spectrometer the following nomenclature is used:

• **Region**: two regions are distinguished, the barrel (B) at $|\eta| < 1$ and endcap (E) at $|\eta| > 1$. In the endcaps the chambers are subdivided into an inner and outer ring; the outer ring is labeled E (as external) and the inner ring is referred to as forward (F).

• **Station**: location of a chamber or a group of chambers; the stations names are: inner (I), extra (E), middle (M) and outer (O).

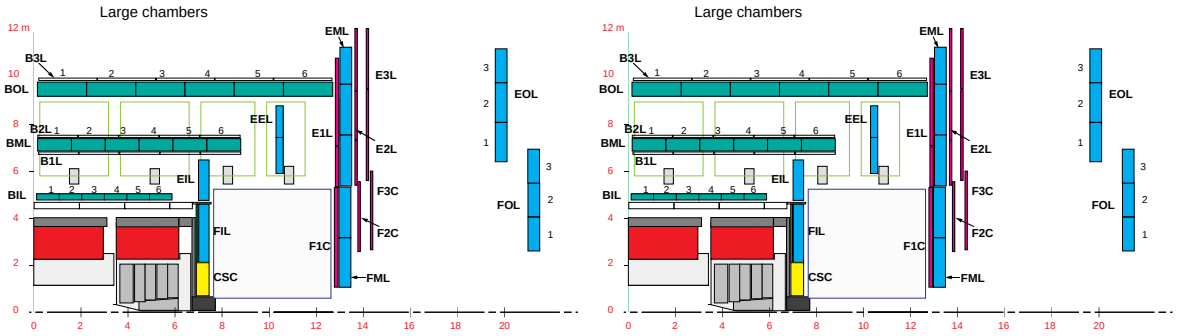

Figure 3.1: *Naming and counting scheme for chambers in even sectors (on the left) and in the odd sectors (on the right).*

• **Sector**: the system is subdivided into 16 sectors. Sector correspond to azimuthal regions defined by the barrel magnet structure: regions between barrel coils (odd sector numbers) and the regions covered by the barrel coils (even sector numbers). See figure 3.2.

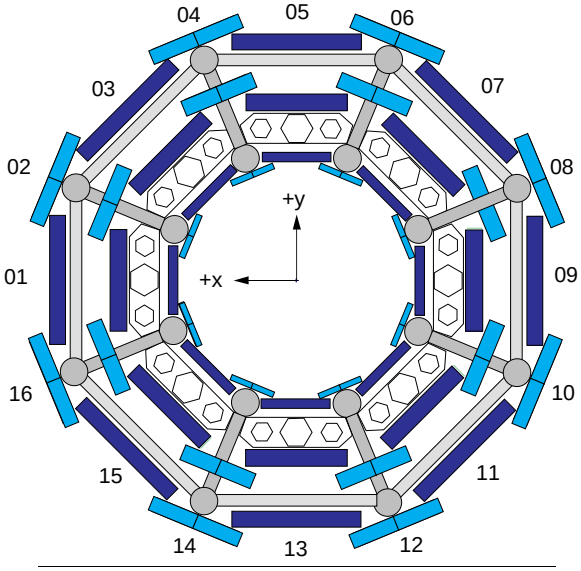

Figure 3.2: *Definition of sectors; view into +z direction.*

• **Side**: the two detector hemispheres (A and C) as defined in the global ATLAS coordinate system (see Par. 2.4.1) by the positive and negative z-direction.

• **Projective towers**: an ensemble of all chambers in a common solid angle as seen from the interaction point. This concept is used in the alignment, trigger and readout implementation.

3.1.2 Chamber Layout

The MDT Chamber usually consists of two multilayers (ML), numbered 1 and 2 with ML1 being the ML closest to the interaction point. The two multilayers are separated by a 'spacer' and support structure; a spacer structure is made of three cross-plate perpendicular to the tubes and located at the two ends and in the middle of the tubes. Each ML consists of three or four (for the inner chambers[1]) layers of drift tubes. In a few spacial areas chambers without spacer structure and of different design are used. The length (dimension in the z-direction) of a chamber is defined number of tubes per layer. The total width of a MDT chamber is given by the tube length plus the size of the electronics box. The electronics box or Faraday cage houses the front-end MDT electronics [2] which consists of printed circuit boards carrying the ASD chips and serving 24 tubes (this board is also called 'hedgehog board') and on top of the hedgehog board a 'mezzanine card' with the TDC (and ADC output also).

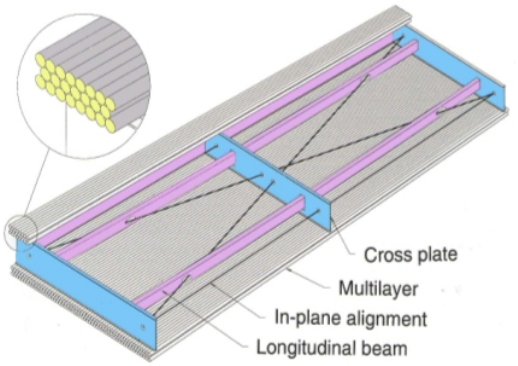

Figure 3.3: *Schematic view of a standard MDT barrel chamber. In each multilayer the MDTs are stacked in either four (inner station) or three (middle and outer stations) layers. The chambers in the endcap are trapezoidal in shape, but are of similar design otherwise.*

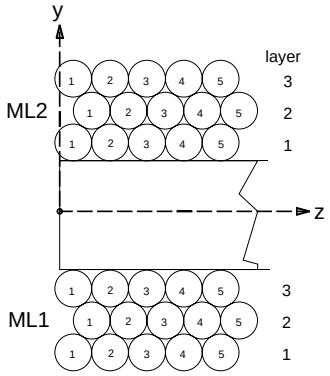

Figure 3.4: *Naming and numbering conventions within a MDT chamber.*

MDT chambers are labelled as XYZ; X denotes whether the chamber is located, in the barrel (B) or in the endcap (E); Y stands for the muon station: (I)nner, (M)iddle or (O)uter; while Z specifies whether a chamber spans the region between two toroid coils ((L)arge) or whether it is found in line with one of them ((S)mall).

[1]The innermost shell of MDT chambers is equipped with eight rather than six layers of tubes in order to improve pattern recognition.

3.1.3 Gas Distribution System

In the MDTs, as in any drift chamber, variations of the fundamental properties of the gas, such as pressure, temperature and composition, have important effects on the tracking precision. Drift velocity and gas gain are quite sensitive to the density. Also the attenuation of drifting electrons depends on the gas composition. Finally the lifetime of the tubes, limited by the gradual formation of insulating deposits on the anode and cathode surfaces, is sensitive to the presence of certain chemicals. So, the gas system is designed to guarantee a very high stability of the operating conditions, as well as a maximum control of pressure, temperature and composition of the gas.

The MDT gas system [3] has to supply approximately 380000 pressurized drift tubes, which are grouped into about 1200 chambers of different size, with the operational gas, which is a mixture of argon and carbon dioxide (93%-7%), with the addition of a small quantity of water vapor.
Mainly financial reasons forbid an operation of the full ATLAS MDT system in vented, one-pass mode. A daily gas refreshing rate of 10 % of the total detector volume per day has been chosen as the baseline. The gas circulation rate in the MDT detector will be 1 volume/day, based on the concept that any contamination, whether by irradiation effect on the gas, or by any leaks in the system, is thus diluted and its impact on the detector performance reduced. The gas will be circulated in a closed system and the main system components are:

- *Gas Mixer:* its basic function is to mix the three mixture components with high accuracy in the right proportions and to supply the mixture at the required flow rate to the gas circulation loop.

- *Circulation System:* the gas coming back from the chambers must be recompressed for feeding through the purifiers and it is reinjected by a high-speed turbine compressor from ATEKO [4]. In order to obtain a circulation rate of one volume per day, the gas will be circulated at 100 Nm^3/h. A filter is used after the compressor to prevent dust from proliferation into the gas circuit.

- *Gas Purifiers:* these modules consist of cartridges filled with metal catalyst (Copper or Nickel) on a porous carrier material (graphite or AlO_3). To avoid that the carrier absorbs water by physical adsorption, the purifier will be heated during running conditions.

- *Distribution System:* the gas arriving in the cavern is distributed to the chambers and recollected on the output. The entire distribution system consists of 15 sub-distribution systems, and each of the distribution sub-units supplies gas to a group of chambers and regulates their pressure with an accuracy of 0.1%.

3.1.4 The On-Chamber Gas System

The on-chamber gas distribution system supplies the gas from a single input directly to each tube and collect their output in a single output: this kind of distribution is called *fully parallel*. The input and the output lines of the gas ends into two volumes called gas bar. Each tube

is connected to these gas bar with the help of stainless steel tubelets which end in plastic "jumpers", as showed in figure 3.5. Each jumper fits over an MDT endplug.

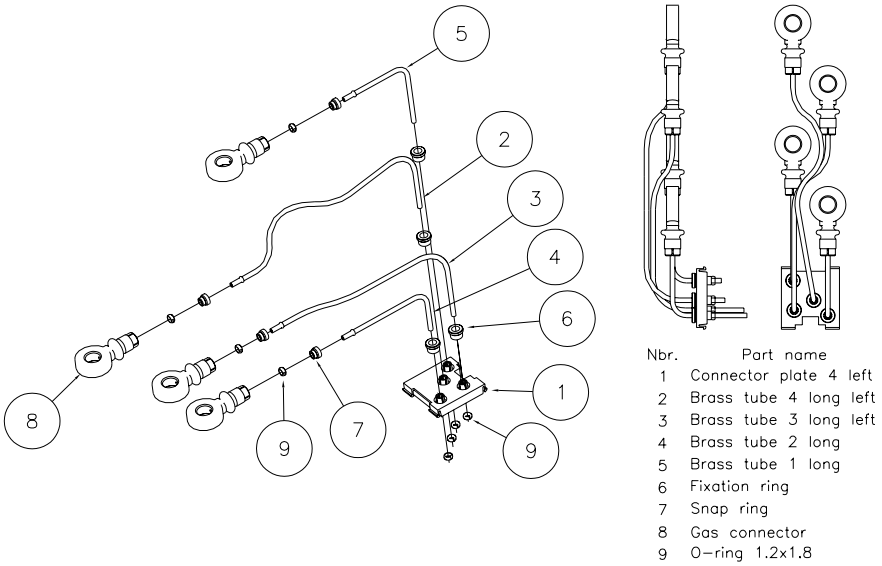

Figure 3.5: *Tubelets needed for the tube connection to the gas bar.*

The use of sealant compounds and of glue was avoided to minimize the risk of chamber ageing due to contaminations.
In table 3.1 the MDT gas system specifications are summarized.

Parameter	Value
Total Volume	754 m^3
Operating pressure	3 bar abs.
Number of chambers	682 (barrel) 512 (endcap)
Number of gas channel	112 (barrel) 162 (endcap)
Gas circulation	1 volume/day
$\Rightarrow$ Circulating flow	$\sim$ 100 Nm^3/h
Refreshing rate	10% of total volume/day
$\Rightarrow$ Fresh flow	$\sim$10 Nm^3/h
Leak rate	$\leq$ 0.1 Nm^3/h
Impurities	$\leq$ 100 *ppm* O_2
Water content	$\sim$ 500 *ppm* (max 1000 *ppm*)
Materials and components	oil-lubricant free, no silicon

Table 3.1: *The MDT gas system specifications.*

3.2 The Monitored Drift Tubes - MDTs

The basic detection elements of the MDT chambers are aluminium tubes of 30 mm diameter and 400 μm wall thickness, with a 50 μm diameter central $W - Re$ wire (Figure 3.6) and two endplugs which close off the MDT at both ends (Figure 3.7).

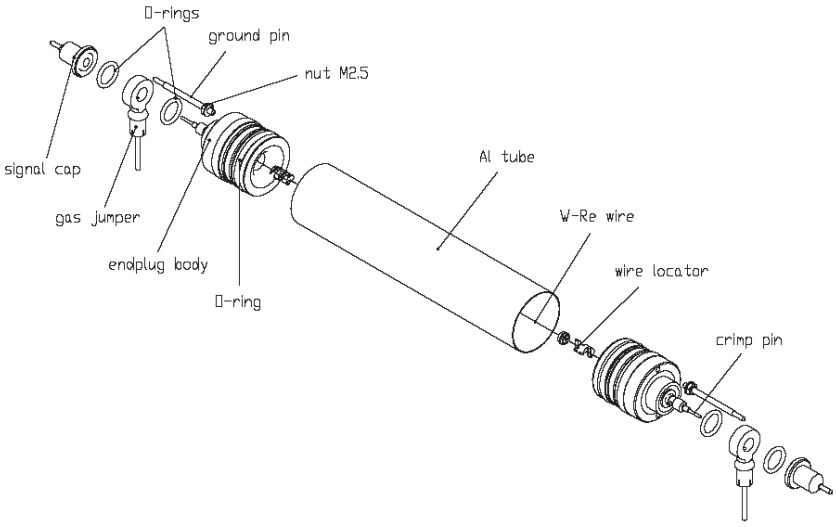

Figure 3.6: *An exploded view of an MDT tube.*

In addition to sealing the two ends of the MDTs, the endplugs provide electrical insulation between the high voltage carrying anode wire and the outer tube wall; they further fixate and position the wire with respect to the aluminium tube and they allow the connection of the MDT to the gas distribution and ti the front-end electronics. The precisely machined outer surface of the endplug is used during chamber assembly to control the relative position of the wires to the required 20 μm level. The single-wire resolution is $\sim$ 80 μm. The tube lengths vary from 70 cm to 630 cm.

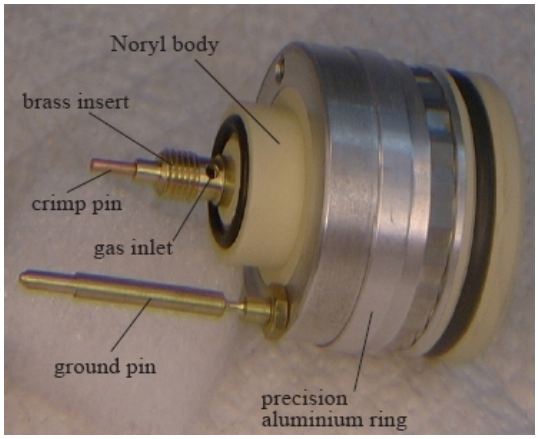

Figure 3.7: *Photograph of an MDT endplug [5]. The hole in the brass part is used to supply the gas during operation. The copper crimp pin fixates the anode wire in the assembled drift tube.*

The tubes are operated with a non-flammable mixture of 93% Ar and 7% CO_2 at 3 bar absolute pressure and the wire is at a potential of 3080 V. The chosen working point provides for a non-linear space–time relation with a maximum drift time of $\sim$ 700 ns, a small Lorentz angle, and excellent ageing properties.

Table 3.2 summarizes some operating parameters of the MDT.

Parameter	Design value
Outer tube radius	14.985 mm
Wall thickness	400 μm
Tube material	Al
Anode wire radius	25 μm
Anode wire material	W-Re alloy (97:3), gold plated
Anode wire resistance	44 Ω/m
Gas mixture	$Ar_C O_2$(93:7)
Gas pressure	3 bar abs.
Gas gain	2 $\cdot 10^4$
High voltage	3080 V
Maximum drift time	700 nm

Table 3.2: *The MDT operating parameters.*

3.2.1 Principle of Operation

Drift tubes are gas-filled ionization detectors which operate in proportional mode. The thin anode wire is supplied with a high voltage of typically a few kV, while the metallic tube wall is grounded. Electrons and ions created in pairs by a traversing ionizing particle drift towards the anode and the cathode respectively in the radially symmetric electric field

$$E(r) = \frac{V}{\ln \frac{b}{a}} \cdot \frac{1}{r} \tag{3.1}$$

where V is the anode wire potential, b the tube and a the wire radius. Close to the wire the electric field is sufficiently high for the drifting electrons to gain enough kinetic energy to cause secondary ionization; the total number of electron-ion pairs increases by a factor G known as gas gain or gas amplification. For the Atlas MDTs the nominal gas gain was chosen as $2 \cdot 10^4$, to minimize the effect of ageing.

Ionization

Muons: for muons and other charged particles the average energy loss when traversing a material layer of thickness dx is described by the Bethe-Bloch formula [6]:

$$-\frac{dE}{dx} = Kz^2 \cdot \frac{Z}{A} \cdot \frac{1}{\beta^2} \cdot (\frac{1}{2} \ln \frac{2m_e c^2 \beta^2 \gamma^2 K_{max}}{I^2} - \beta^2) \tag{3.2}$$

with $K = 0.31\ MeVg^{-1}cm^{-2}$. In this equation ρ is the density, Z the atomic number and A the mass number of the absorbing material; z is the charge of the traversing particle. The dimensionless parameters β and γ are defined in the standard way as $\gamma = E/(mc^2)$ and $\beta^2 = 1 - 1/\gamma^2$. K_{max} is the maximum kinetic energy which can be imparted to a free electron in a single collision; I is the mean excitation potential of the absorbing material. Formula 3.2.1 describes the mean energy loss of a particle in matter; fluctuations around the average value can be significant. In the case of a thin absorber, i.e. in particular for gases, the actual energy deposition follows a Landau distribution [7]. The average energy needed to ionize a single argon atom is:

$$n_p = 26eV, \tag{3.3}$$

and this energy is, more or less, independent of the type of ionizing particle. In a fraction of events the produced electron has enough energy to cause secondary ionization itself, usually very close to the point of the original interaction. This leads to the formation of electron-ion clusters along the particle trajectory. In some cases the electron produced has an energy high enough to travel a macroscopic distance, the so-called *delta* -electrons. A consequence of both the cluster size fluctuations and the finite distance between the points of ionization is that muon signals of a drift tube typically show more than one maximum (Figure 3.8); this is in particular true for tracks close to the wire for which the drift distance is largely different for electrons produced close to the tube wall and in the middle of the track.

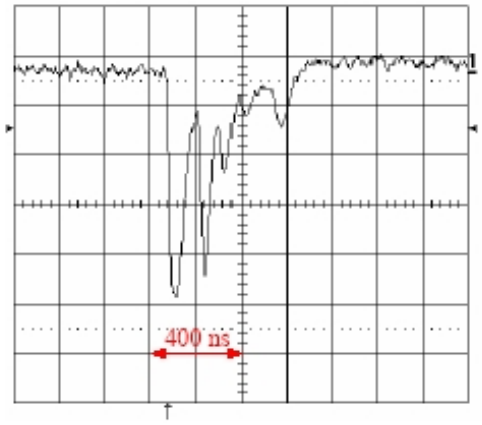

Figure 3.8: *Signal generated by a muon in a MDT [5]. Muon tracks typically generate signals with several maxima, if the track is not too close to the tube wall; these are caused by different ionization clusters along the muon trajectory.*

Photons: Photons below 1.02 MeV can interact with the operating gas or the tube wall of an MDT either by the photo-electric effect or by Compton scattering. In the first case, which dominates at low energies, the full photon energy E_γ is transferred to a single electron; for $E_\gamma < 25$ keV the range of the produced photo electron in argon at 3 bar is of the order of a few millimeters maximum (for example: for a 25 keV electron the range is 4.5 mm). The consequence is that the full photon energy is deposited in the drift gas over a relatively small path length and the MDT signal of such interactions shows a single peak without the multiple maxima typical of muons. Measured pulse charge spectra are usually Gaussian in shape; (mono-energetic) γ -sources of a few tens of keV energy (like ^{109}Cd, or ^{241}Am) are therefore well suited for pulse height studies.

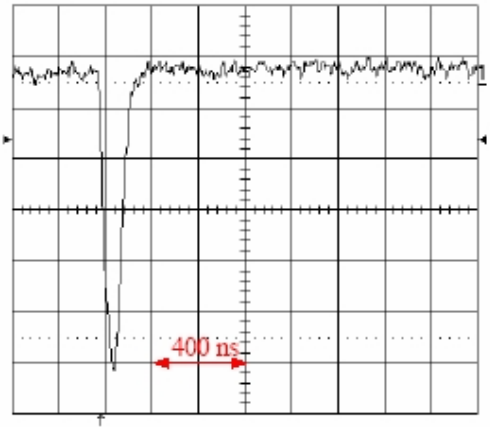

Figure 3.9: *Signal generated by a 22 keV photon from a ^{109}Cd in a MDT [5]. The signal shows a single peak structure.*

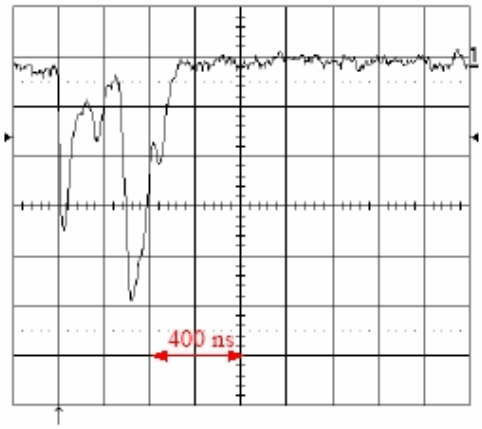

Figure 3.10: *Signal generated by a 660 keV photon from a ^{137}Cs in a MDT [5]. The signal looks like a muon signal (Figure 3.8) and it is typical of photons interacting via Compton scattering.*

Electron and Ion Drifts

The movement of the primary electrons produced along the trajectory of a charged particle traversing a drift tube is governed both by the electric field (Equation 3.2.1), and by frequent collisions with the molecules of the operating gas. The drift process can be described by the

so called rt-relation $r(t)$ which for each track distance r from the wire gives the corresponding time t the fastest electrons need to reach the anode and produce a signal. An accurate knowledge of the rt-relation, in the case of the Atlas MDTs to a level of $<20\ \mu m$, is a prerequisite for using drift tubes to precisely reconstruct particle tracks. The rt-relation is highly dependent on the chosen operating gas and on the operating parameters. The MDT mixture, $Ar : CO_2(93{:}7)$, belongs to the group of so-called nonlinear drift gases for which the electron drift velocity v_{drift} is not independent of the reduced electric field strength E/ρ where ρ is the gas density. It immediately follows that v_{drift} is not constant over the cross section of the tube. Figure 3.11) shows the rt-relation in absence of a magnetic field.

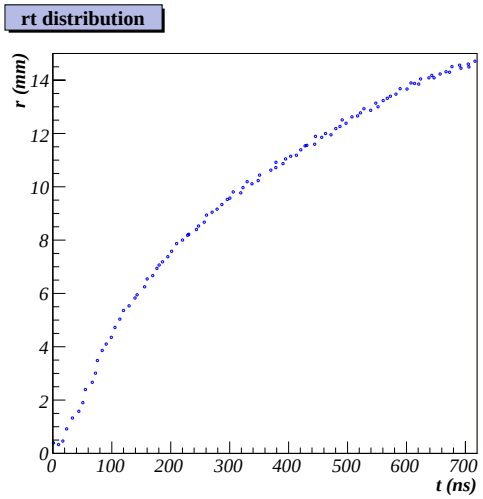

Figure 3.11: *rt-relation.*

In the magnetic field the wires are oriented essentially parallel to the field lines. The magnetic effect on the rt-relation is through a small deviation away from a radial drift and a small reduction of the apparent drift velocity; the size of this shift depends on the gas and on the fields.

The presence of certain admixtures in the gas even at concentrations of a few hundred to a few thousand parts per million can have a large impact on the drift process, either by changing the transport parameters itself or due to electron capture. The latter will result in a loss of signal height, especially for long drift distances. The most common trace impurities are oxygen, nitrogen and water. Oxygen and nitrogen will usually get into the active volume of a drift chamber through small leaks in the detector itself or in the gas system. Water is ubiquitous in almost any system due to outgassing and surface desorption effects. A second mechanism for the accumulation of water is by diffusion through plastic materials which are often permeable for H_2O molecules to a greater or lesser extent. Trace levels of oxygen or air in $Ar : CO_2$ drift mixtures have only a small influence on the electron transport. The main problem with O_2 is its large electro-negativity and thus a high affinity towards electrons. Its concentration in a drift gas has to be well controlled in order to avoid a large signal attenuation. For the Atlas MDTs the maximum oxygen concentration permitted is 100 ppm.

The majority of drifting ions in an MDT is produced during the gas amplification process close to the anode wire. The small fraction of ions which are created directly during the primary ionization process is negligible for a gas gain of $2 \cdot 10^4$. Typical ion drift velocities v_{ion} are of the order of a few mm/ms. For small field strengths, v_{ion} is proportional to the electric drift field E:

$$v_{ion} = \mu \cdot \frac{E}{p} \tag{3.4}$$

where μ is a constant, the ion mobility, and p is the gas pressure.

The Gas Amplification

Close to the wire the electric field strength becomes sufficiently large for the drifting electrons to gain enough kinetic energy to cause secondary ionization, as already mentioned. The gas amplification process follows the relation:

$$dN = \alpha \cdot N \cdot ds \tag{3.5}$$

where dN is the number of electrons produced by the multiplication in a small drift distance ds the gas and it is proportional to N, the number of already existing electron-ion pairs, and to the factor α, the first Townsend coefficient which depends strongly on the gas used, the electric field E and the gas density ρ. For drift tubes with a typical electric field E between 10^2 and 10^3 $V/(cm \cdot Torr)$ near the anode wire, an analytic formula for the gas gain G can be derived by making the assumption that α is proportional to E. Doing so one finally arrives at the expression:

$$G = \left[\frac{E(a) \cdot \rho_0}{E_{min}(\rho_0) \cdot \rho} \right]^{\frac{\ln 2 \cdot a \cdot E(a)}{\Delta V}} \tag{3.6}$$

and substituting 3.2.1 for the electric field $E(a)$ in the expression, it becomes:

$$G = \left[\frac{V}{a \cdot \ln \frac{b}{a} \cdot E_{min}(\rho_0) \cdot \frac{\rho}{\rho_0}} \right]^{\frac{\ln 2 \cdot V}{\ln(b/a) \cdot \Delta V}} \tag{3.7}$$

which is known as "Diethorn formula". As in equation 3.2.1 a is the wire radius, b the tube radius and V the applied voltage. For a given gas the two constants ΔV and E_{min} must be obtained experimentally. E_{min} can be interpreted as the minimum electric field at a given gas density ρ_0 at which the gas amplification process sets in.
The Diethorn parameters for the Atlas MDT operating gas $Ar : CO_2(93 : 7)$ were measured and they are:

$$\Delta V = 34V$$
$$E_{min} = 24kV/cm$$

with an estimated accuracy of $\pm 10\%$ for a ρ_0 of 1 bar and a temperature of 25 C [8].

Signal Formation

When an electron drifts in the high-field region, an avalanche process sets up producing ion-electron pairs. The positive ions cloud moves from the avalanche zone towards the cathode while the electrons drift to the wire, inducing a current in the anode wire. If the anode is kept at a constant potential V, the current induced i from a moving charge q can be calculated by the Ramo theorem [9]:

$$i(t) = -\frac{q}{V} \cdot v(t) \cdot E(r(t)) \tag{3.8}$$

where V is the potential, v its velocity and E the electric field. The equation 3.8 is a simple consequence of energy conservation, with the minus sign being convention. Since the drift distance covered by the electrons is about 100 μm, from the amplification zone near the wire to the wire itself, the signal induced by the electrons is a sharp spike of about 100 ps containing very little charge. Thus the contribution of electrons at the total signal is negligible compared to the contribution of the ions. Substituting in equation 3.8 the ion velocity v_{ion}, the signal induced by a single ion is:

$$i(t) = -\frac{q}{2 \cdot \ln b/a} \cdot \frac{1}{t + t_0} \tag{3.9}$$

where $t_0 = \frac{a^2}{2\mu V} \cdot ln(b/a)$ and t varies from 0 to t_{max}, which is the arrival time of the ion at the cathode (some ms). The current signal is then read out from one side of the tube, amplified, shaped and then sent to a discriminator.

3.3 The ATLAS Background environment

The physics performance of the Muon System depends strongly on the level of background recorded in the active elements. The main source of this background is from particles produced in the interaction of primary hadrons from proton-proton collisions with the material of the detector (especially the calorimeters and the toroid structures), and with machine elements such as the collimators and the beam pipe.

The particles are neutrons (Figure 3.12), low-energy photons originating from neutron capture, and charged particles. The neutrons mostly have thermal energies, while the photons

(Figure 3.13) are concentrated in the 200 keV to 2 MeV energy range. The interaction of these photons with the detector material (aluminium in the case of precision chamber, or Bakelite in the case of the trigger detectors) produces signals in the sensitive volume of the chambers via the Compton effect with a probability of about 10^{-2} [10]. Neutrons have a much lower probability to produce a direct signal in the muon detectors, but are directly responsible for the photon flux. The charged particle background consists mainly of muons, charged pions, protons, electrons and positrons. The muons and pions are produced mostly in K^0 decays, while the protons emerge from neutron spallation processes. Hadrons and muons have a typical momentum of 100 MeV.

Figure 3.12 and figure 3.13 (and figure 3.14 shows the full quadrant of ATLAS detector as simulated by the radiation background simulation program, GCALOR) show the neutron and photon fluxes as reported by the ATLAS radiation background task force [11].

Referring to figure 3.13, photon rates are highest in the region close to the beam pipe, in particular in the two innermost endcap station (Figure 3.14).

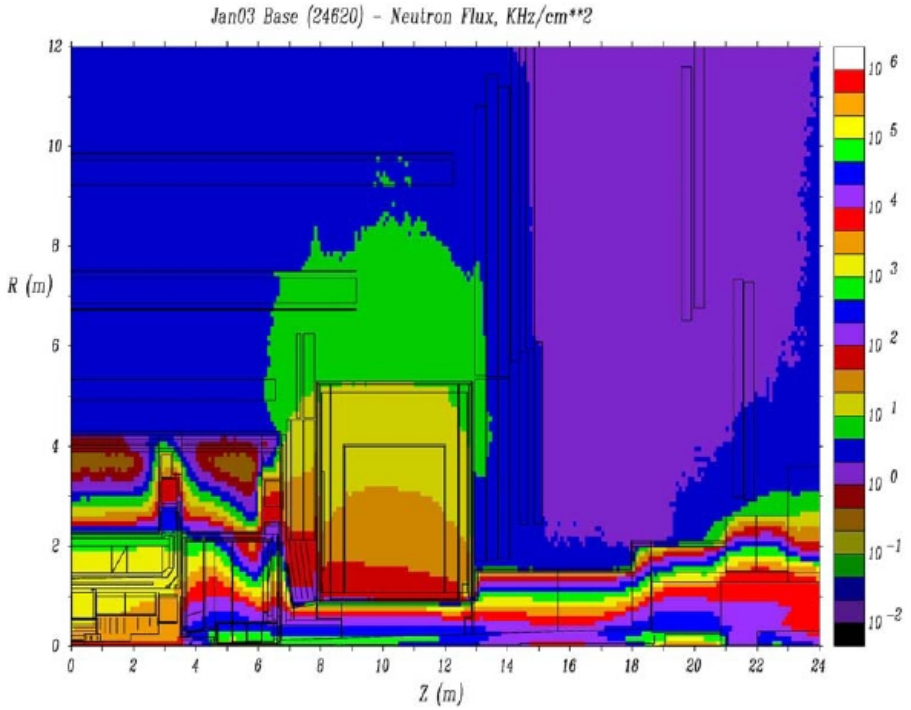

Figure 3.12: *The neutron flux in the GCALOR baseline geometry [11] for a luminosity of* $10^{34}\ s^{-1}cm^{-2}$. *Neutron rates are highest next to the interaction point.*

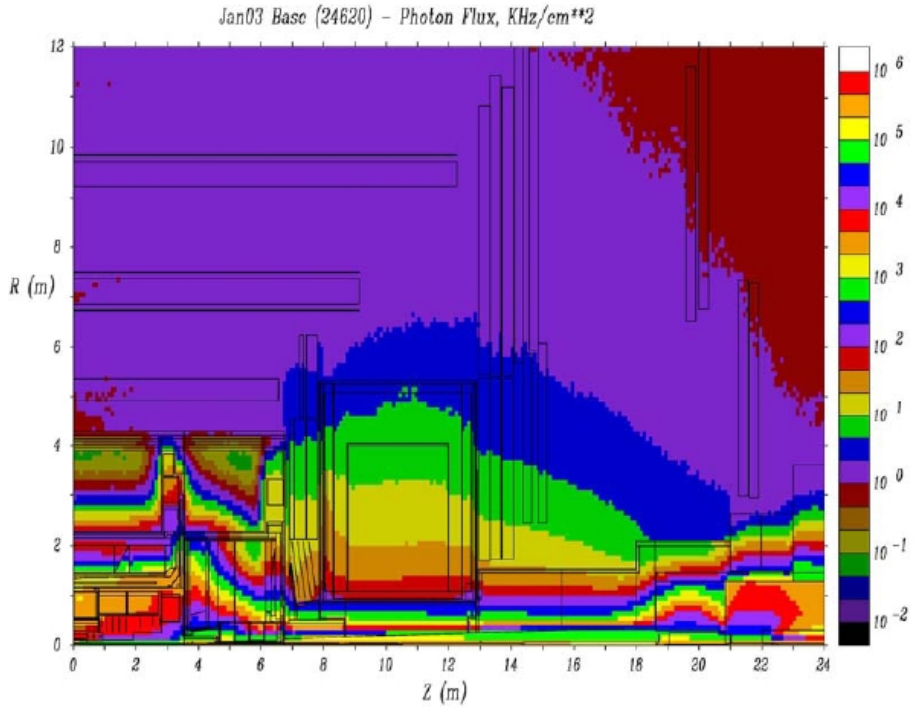

Figure 3.13: *The photon flux in the GCALOR baseline geometry [11] for a luminosity of* $10^{34}\ s^{-1}cm^{-2}$*. Photon rates are highest in the innermost part of the inner endcap station.*

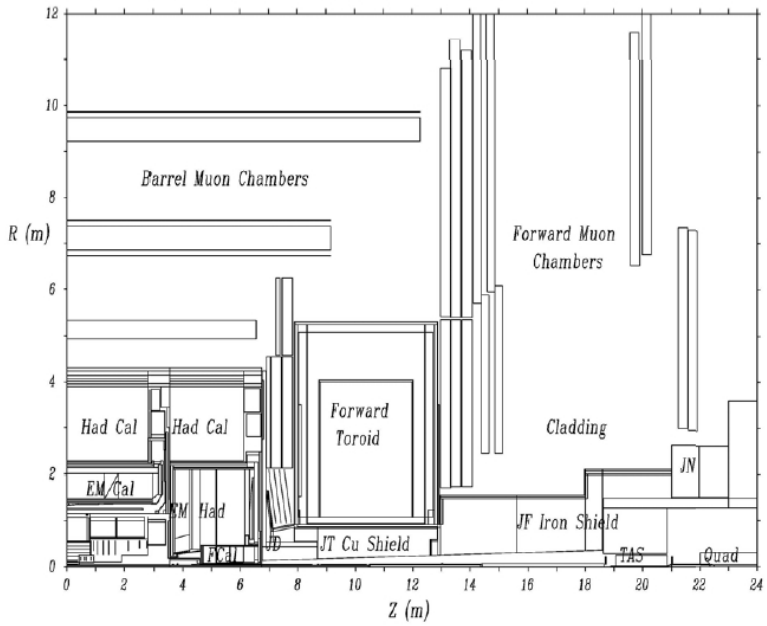

Figure 3.14: *A full quadrant of the ATLAS detector as modelled by GCALOR simulation program [11].*

3.3.1 MDT rate capability requirements

The sum of expected neutron, photon and charged particle count rates in the Muon Spectrometer is shown in figure 3.15.

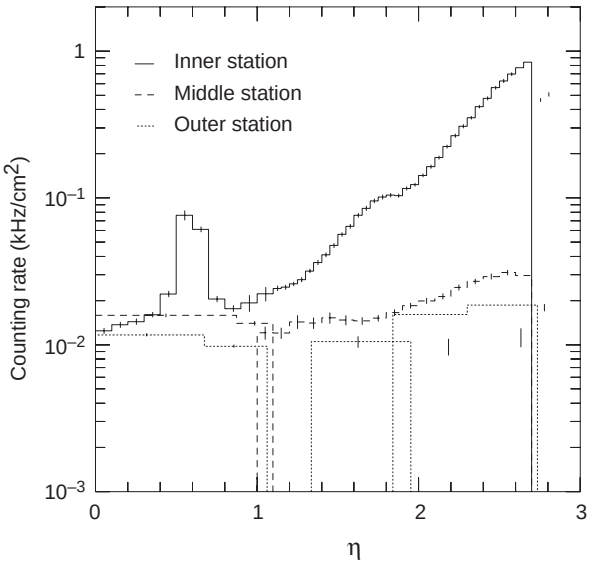

Figure 3.15: *Total counting rates in the three MDT chamber stations as a function of pseudorapidity at a luminosity of* 10^{34} $s^{-1}cm^{-2}$.

The main cause of possible degradation of MDTs is the large amount of charge deposited on the anode wire. This charge is the integral of primary charge times the gas over time:

$$Q = \int (R \cdot N_e \cdot d \cdot G \cdot e)dt \tag{3.10}$$

where R is the particle rate, N_e is the number of primary electrons produced per incident particle, d is the tube diameter, G is the gas gain and e is the electron charge in Coulomb.

The average number of expected primary electrons per photon event, which depends on the photon energy, is [1]:

$$N_e = 1235, \tag{3.11}$$

to be compared to about 750 primary electrons produced for a minimum ionizing muon. The average photon efficiency is approximately $5 \cdot 10^{-3}$.

MDT neutron detection probabilities are typically smaller by a factor 10, as has been verified experimentally both for thermal [12] and fast neutrons [13].

The highest rate, in the innerpart of the endcap inner station, is approximately 100 Hz/cm^2. Based on this result the MDTs must be able to sustain without significant degradation of their performance the maximum rate defined as:

$$R_{max} = 5 \cdot 100Hz/cm^2 = 5 \cdot 300Hz/cm \tag{3.12}$$

in which the factor 5 with respect to the actual prediction was introduced to allow for uncertainties in the background simulations as well as for changes in the shielding design and for a potential luminosity upgrade in the future.

So, during the 10 years of LHC operations(10^8s), it will be reached a maximum accumulated charge of

$$Q_{max} = 5 \cdot R \cdot N_e \cdot d \cdot G \cdot e \cdot t = 0.576 C/cm \simeq 0.6 C/cm \tag{3.13}$$

assuming a gas gain of $2{\cdot}10^4$ and treating all background events as photons (Formula 3.11).

3.4 Summary

In the Muon Spectrometer for the precision measurements of the muon tracks in the main bending direction of the magnetic field, Monitored Drift Tube chambers are mainly used, except for the innermost ring of the endcap inner station, where particle fluxes are highest. The Muon Spectrometer is designed to perform measurements with a momentum resolution $\Delta p/p < 1 \times 10^{-4} \times p/GeV$, for $p_T > 300\ GeV$.

In this chapter the gas distribution system for the muon chamber was described and the working principle of drift tubes was discussed.

At the end of the chapter the background conditions expected at the LHC were also reported.

Bibliography

[1] *ATLAS Collaboration*, ***Muon Spectrometer Technical Design Report***, CERN/LHCC 97-22, 1997.

[2] *C. Posch, E. Hazen and J. Oliver*, ***MDT-ASD, CMOS front-end for ATLAS MDT***, CERN/ATL-MUON-2002-003, 2002.

[3] *F. Hahn and S. Palestini*, ***The MDT Gas System, a Design Report***, CERN/ATLAS Internal Document, 2002.

[4] *ATC a.s.*, ***Argon-Turbo-Circulator, Technical Description and Service Instructions***, Hradec Králové, Czech Republic, 2001.

[5] *S. Zimmermann*, ***High Rate and Ageing Studies for the Drift Tubes of the Atlas Muon Spectrometer***, PhD Thesis, Albert-Ludwing Universitat Freiburg, Germany, 2004.

[6] *Particle Data Group*, ***Review of Particle Physics***, Phys. Lett. B 592, 1, 2004.

[7] *W. R. Leo*, ***Techniques for Nuclear and Particle Physics Experiments***, Springer-Verlag, New York, 1994.

[8] *M. Aleksa and W. Riegler*, ***Non-Linear MDT Drift Gases like Ar/CO_2***, CERN/ATLAS Note ATL-MUON-98-268, 1998.

[9] *W. Blum and L. Rolandi*, ***Partilce Detection with Drift Chambers***, Springer-Verlag, Berlino, 1993.

[10] *ATLAS Collaboration*, ***ATLAS Detector and Physics Performance Technical Design Report***, CERN/LHCC 99-14, 1994.

[11] *ATLAS Radiation Background Task Force*, ***Estimation od Radiation Background, Impact on Detectors, Activation and Shielding Optimization in ATLAS***, CERN/ATL-GEN-2005-001, 2005.

[12] *S. Borzakov et al.*, ***Response of the MDT to Thermal Neutrons***, CERN/ATLAS Note ATL-MUON-96-116, 1996.

[13] *S. Ahlen et al.*, ***Measurement of ATLAS MDT Neutron Sensitivity and Development of a Simulation Model***, CERN/ATLAS Note ATL-MUON-98-236, 1998.

Part II

AGEING STUDIES

Chapter 4

Ageing Studies on the Drift Tubes of the Muon Spectrometer

This chapter summarizes the results of ageing studies performed on ATLAS MDT chambers and on a prototype of the ATLAS gas recirculation system from September 2003 till May 2004 at the CERN **G**amma **I**rradiation **F**acility (**GIF**). In 2002-2003 and 2003-2004 ageing tests the conditions differed significantly from previous ageing studies which were typically performed with single tubes in a dedicated laboratory setup and with a simple flushing gas system.

The 2002-2003 ageing test [1],[2] on an ATLAS MDT chamber of type BIS [3], performed to validate the final ATLAS high speed gas circulator ATC (Argon Turbo Circulator [4]), revealed a loss in performance of MDTs operated under gas recirculation due to Silicon pollution. The test also revalidated the Ar:CO_2 mixture and the materials used in MDTs construction as ageing-free, since MDTs operating in flushing mode did not show any ageing behavior. Further analyses made on the BIS multilayer affected by ageing and on gas system components showed the source of Silicon to be the sealing material of three valves in the gas system. This result was the reason to perform another ageing test with the same gas recirculation system after its careful cleaning. The aim was to finally validate the ATC and to certificate the cleaning and assembly procedures and the proper functionality of some gas system components.

Another goal of the 2003-2004 test was to verify the standard behaviour of "reconditioned" MDTs, such as those tubes cured from the problem of self-sustained dark currents.

For this new test the same ATLAS MDT chamber of type BIS (Beatrice) and two small chambers with four layers of six tubes each, commonly referred to as "bundles", have been installed in the X5/GIF area at CERN. One of the two bundles was made of reconditioned tubes, the other one was mounted as comparison. The chambers were exposed to intense γ-radiation from a 630 GBq ^{137}Cs source, emitting 662 keV photons for 6.5 days per week and during the remaining half a day reference runs were taken.

An accumulated charge equivalent to 5 years of LHC operation (including the safety factors 5 to allow for uncertainties in the estimated background) was reached. The study was performed with chambers under gas circulation using the gas circulator ATC and all the

gas system components carefully cleaned.

The test set-up, the DAQ and the analysis chain were changed with respect to the previous ageing test, to maximize the sensitivity on the MDTs performances at different positions along the wire. To check their uniform response along the wire, the pulse height generated in the tubes by the signals of two movable ^{241}Am γ-sources was monitored during weekly reference runs.

4.1 The Gamma Irradiation Facility - GIF

The **G**amma **I**rradiation **F**acility - ***GIF*** - is an experimental zone located in the West Area at CERN in which an intense radioactive ^{137}Cs source (740 GBq initial activity) and a weak muon beam line from the SPS accelerator (***X5***) are present to test LHC detectors under conditions very similar to the operating environment at the Large Hadron Collider. A sketch map of the GIF zone is shown in figure 4.1.

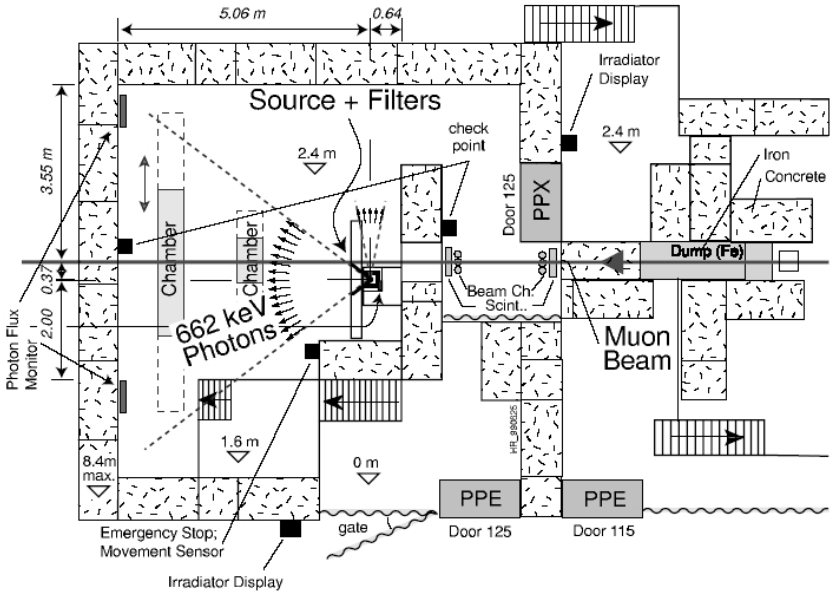

Figure 4.1: *Sketch map of X5/GIF test beam zone at CERN West Area.*

The radioactive ^{137}Cs source emits photons of 662 keV energy. A set of movable lead filters are located in front of the source and they can be used to adjust the photon flux over a range of several orders of magnitude.

4.2 The "Ageing" Problem

Due to the complexity of the ATLAS detector design, the need to change a muon spectrometer chamber after some time of operation in case of a failure will be dangerous in term of time consuming and difficulty, or practically impossible. A careful study of the factors limiting drift tubes lifetime is therefore essential. Typical effects of degradation with time are gas gain losses, decrease in resolution or efficiency, excessive currents and formation of sparks. The various effects are radiation induced, not reversible by a simple gas exchange and affect the tube normal operation, and they are summed up in the expression "ageing".

4.2.1 Wire Chamber Ageing Mechanism

Ageing effects observed in wire chambers are normally due to deposits on either the anode or the cathode surfaces. Thin coatings on the anode wire surface, which can be insulating or not, lead to a loss in gas gain, as it is possible to see regarding the Diethorn's formula (Equation 3.7). Deposits on the cathode have no direct impact on the gas gain; they can however be the cause for spontaneous discharges and self-sustained currents via a mechanism known as the *Malter effect* [5].
Laboratory ageing studies are normally performed on a time scale far smaller than the foreseen lifetime of the detector, leading to an "extrapolation" to the real LHC conditions. Also it is not clear how the ageing of a drift tube scales with the gas flow, which can often be adjusted over some range. Usually it is assumed that the ageing rate is lower for a higher flux, but it is true only if the ageing is due to the formation of deposits from long-lived or stable molecules, i.e. with a lifetime comparable to the time they stay in the detector volume.

Many attempts were made in the past to find an MDT operating gas on the basis of Argon and methane or ethane [6],[7]. Such mixtures had the advantage of a linear rt-relation, i.e. an electron drift velocity that is independent of the electric field, gas pressure and temperature; in this case field fluctuations caused by a high radiation background do not affect the tube resolution. Methane is moreover a very effective quenching gas without the drawback of a considerable increase in the maximum drift time, as encounted for CO_2. For a long time the gas mixture Ar:CH_4:N_2(91:5:4) was the baseline gas for ATLAS Spectrometer [8], until ageing studies showed that a foreseen MDT lifetime of 10 years under LHC conditions could not be reached with this composition [9]. A modified gas mixture Ar:CH_4:N_2:CO_2(94:3:2:1) was more promising; finally this gas mixture was also discarded in favour of the Ar:CO_2(93:7) gas mixture. This gas mixture was extensively tested for ageing in different laboratory setups using single drift tubes. It proved to be very radiation resistant; no degradation in MDT performances was observed up to integrated charges well above the 0.6 C/cm required for ATLAS (Par. 3.3). The absence of polymerization processes was the main factor because it became the final MDT operating gas, despite a non-linear rt-relation and the relatively large maximum drift time of 700 ns.

Ageing due to Contaminants

Other than the operating gas polymerization, the pollution is the major cause of ageing. The main mechanisms by which contaminants are produced, are:
- *Outgassing*: plastic material often contains traces of non-polymerized monomers left from their production. Since they are not firmly bound to other molecules they can evaporate from the material;
- *Dissociation and material breakdown under irradiation*: chemical substances, that are very stable under normal conditions, can deteriorate if they are exposed to ultraviolet or ionization radiation;
- *Evaporation*: valves in a detector gas system are often greased to prevent them from getting stuck. Soft sealants are used to achieve gas tightness and oils may be present in bubblers to monitor the gas flow. In each of these cases molecules will evaporate from the surface of the liquid or semi-solid material until the concentration in the gas phase equals the vapour pressure of the given substance;
- *Improper cleaning*: a variety of oils, lubricants and cooling fluids is used in the production and machining of both plastics and metals. They have to be removed from the components of a drift detector before its assembly in order to avoid uncontrolled contamination of the operating gas.

From the above list it is evident that materials used in the construction of gaseous detectors to be operated under high rated conditions need to be carefully chosen in order to guarantee an adequate lifetime. The mechanism by which contaminants cause ageing in a wire chamber is the formation if deposits either on the anode or the cathode, as in the case of ageing due to the operating gas, which molecules polymerize and form heavily crosslinked macro-molecules. If ageing is caused by a pollutant, the growth rate of a possible deposit will increase with the gas flow if the probability for impurities to be captured by the anode wire is high, since in this case a larger number of molecules is transported into the detector volume in a given time.
An element found as a deposit on the anode wire in numerous ageing studies is Silicon (Si), which has a very high affinity for deposition on the anode wire of a drift chamber [10].

4.3 2001-2003 Ageing Test

A final ATLAS chamber of type BIS (Barrel Inner Small) [3] (Figure 4.2) became available for ageing tests in 2001. The chamber was exposed over its full size to an intense photon flux at GIF between November 2001 and May 2003 [1]. The MDT performances were monitored in weekly reference runs using cosmic muons, recording for each tube the drift time measurements and, every third tube, recording the pulse height of the signal generated by the muon using a charge integrating ADC.

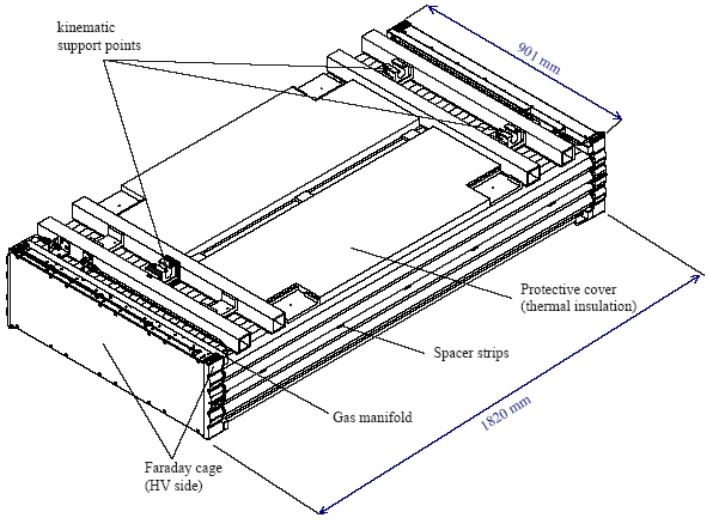

Figure 4.2: *Three dimensional model view of a BIS MDT chamber.*

During reference runs the γ-source was retracted into its lead housing. A 4-layer 105·100 cm^2 scintillator hodoscope was used for trigger purpose; it also permitted to point the position of the cosmic rays in the direction of the MDT wires. One of the major goal of the study was to test a gas recirculation system similar to the one foreseen at ATLAS (Par. 3.1.3). The gas system parameters were chosen such to reproduce the ATLAS conditions as closely as possible; a bypass loop was included to run the gas compressor Argon Turbo Circulator at its nominal flow rate despite the BIS volume constitutes less than one per mille of the total ATLAS volume. One of the two multilayer of the BIS, from now referred as "multilayer 1", was connected to the gas recirculation system, while the second one ("multilayer 2") was operated in flushing mode for comparison.

A typical pulse charge spectrum measured in a reference run is showed in figure 4.3.

For each tube, thus each spectra, a Landau distribution was fitted to the data. The maximum of the Landau distribution, Q_{tube}, is proportional to the gain of the tube, and can be used to investigate possible gain drops. All data has been scaled to 20^oC according to the relation $Q_{20} = Q(T)[1 + 0.022 \cdot (20^o - T)]$, which was established in test beam measurements performed in summer 2002. This relation is in agreement with the one which can be derived from the Diethorn formula 3.7: $\Delta G/G = 9.86 \cdot \Delta T/T$, which corresponds to a gas gain

variation of 3.3% per temperature degree.

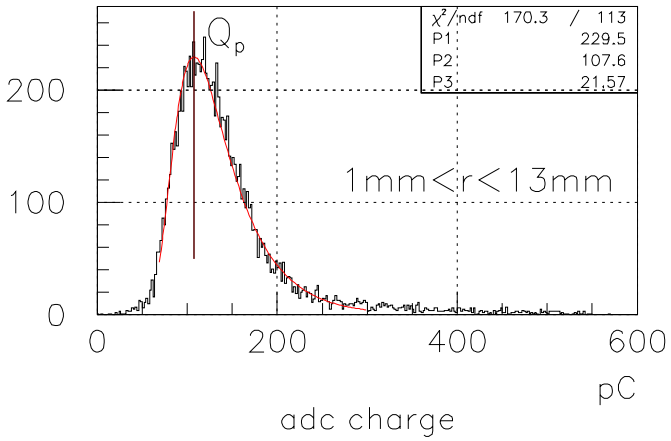

Figure 4.3: *Pulse charge spectrum for cosmic muons; a Landau distribution is fitted to the data. The maximum is indicated as Q_p.*

4.3.1 Results for "multilayer 2" operated in flushing mode

For tubes operating in flushing mode, no loss in pulse height was observed up to an accumulated charge of 240 mC/cm, equivalent to 4 years of LHC operations included the safety factor of 5. Figure 4.4 shows the pulse height $Q_{rel} = Q_{tube(i)}/Q_{ref.tube}$, where $Q_{ref.tube}$ were the tubes disconnected from the high voltage during the irradiation, thus they did not accumulate charge.

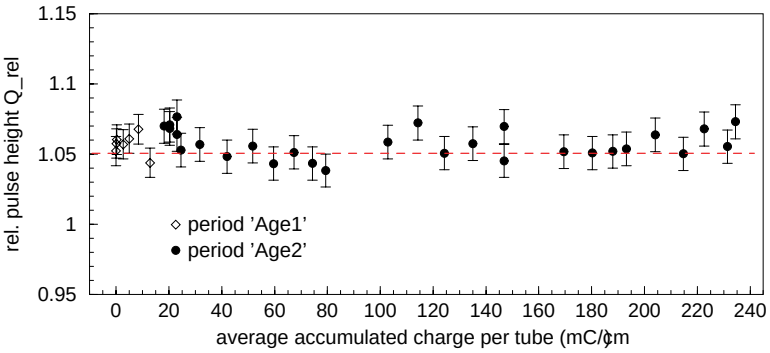

Figure 4.4: *Relative pulse height Q_{rel} as a function of the integrated charge; the results are consistent with a line of zero slope, thus no evidence for ageing is present in the multilayer operated in flushing mode. During the period "Age 1" 30 mC/cm of charge were accumulated, while at the end of period "Age 2" was reached 240 mC/cm of accumulated charge.*

None of the 38 monitored tubes belonging to the vented multilayer showed any distortions in the ADC spectrum, that were similar to the one showed in 4.3.

4.3.2 Results for "multilayer 1" with gas recirculation

For the tubes operated in recirculation mode, ageing effects started to show up when 40 mC/cm of charge were accumulated on the wires. The first effect observed was a distortion of the pulse height spectra, which started to show a second peak at charge smaller than the one fitted with the Landau distribution (Figure 4.5).

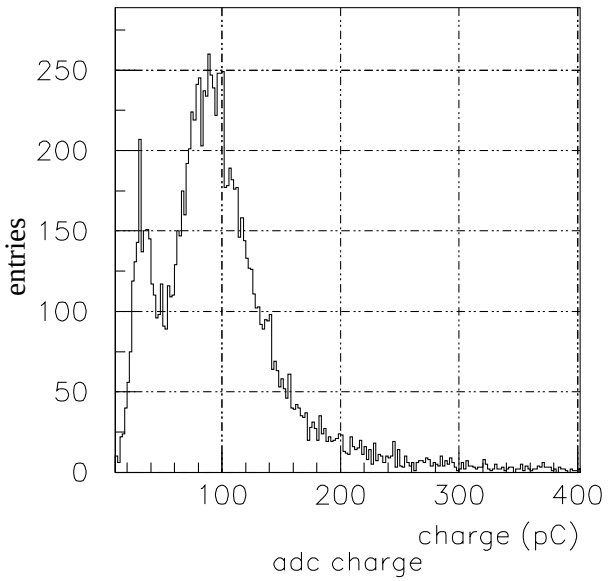

Figure 4.5: *ADC spectrum for a tube operated with gas recirculation after an irradiation of 240 mC/cm.*

Further investigations were done during normal reference runs by reconstructing the cosmic muon track positions along the wire using the hodoscope informations. These studies showed a large loss of gain in the first 30 cm of wire from the gas inlet, then the effect decreased until it was negligible after 50 cm, as it is shown in figure 4.6. These results were obtained after the irradiation period by moving a small radioactive source along the tubes.
All the 33 monitored tubes under high voltage during the irradiation showed drops of gain close to the gas inlet side, while the two reference tubes disconnected from high voltage during the irradiation kept constant their behaviour. After approximately 240 mC/cm the chamber irradiation was stopped, and several MDT were opened: the scanning electron microscope technique (SEM) revealed a growth of needle-like structures on the anode wire.

They had a length of 5-7 μm close to the gas inlet side and decreased in size when moving further along the tube, in agreement with the pulse height behaviour. An energy dispersive X-ray (EDX) analysis indicated that these deposits were made of silicon and oxygen, while no carbon was detected. It was concluded that the observed ageing effects were due to a contaminant: a first attempt to find the pollutant directly in the gas by doing a gas chromatography was unsuccessful. Therefore, since the MDT operated in flushing mode did not show any ageing effects, a deep analysis of the gas system was performed, especially in the region of the recirculation loop. It was found that three valves contained a silicone sealant. Further it was discovered that the specifications about the use of lubricant (no lubricant in all

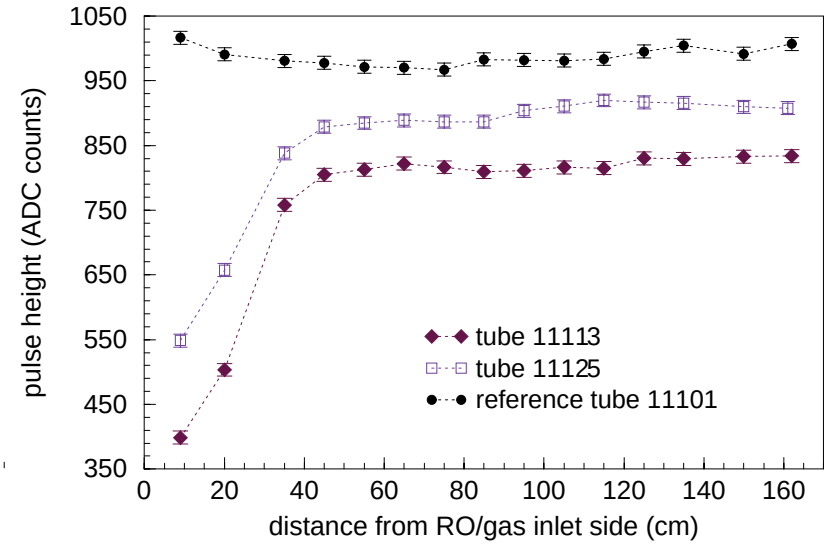

Figure 4.6: *Pulse height versus position in the wire for two tubes operated in recirculation mode.*

the gas system except for the silicon-free vacuum grease Apiezon in few well-defined locations) were not respected.

4.4 2004-2005 Ageing Test: The Experimental Setup @ GIF

In the 2004 the ATLAS MDT chamber of type BIS (Barrel Inner Small), called "Beatrice", and two little test-chambers, referred to as "bundles", were used to perform another ageing test in the light of the previous test results.

The BIS chamber Beatrice (Figure 4.2) is composed of two multilayers, each consisting of 4 layers of 30 MDTs, 170 *cm* long. Only the multilayer used in flushing mode during the previous ageing test and that did not show any ageing effects, was equipped with the gas distribution system and the electronics for the test; the other multilayer was not used, since its tubes were affected by ageing from the previous test and two tubes of these underwent some destructive operations in order to analyze anode wires and aluminium tubes, looking for the source of the loss in performance. So the total BIS volume was of 144 l. The two bundles, are made up of four layers of six 270 *cm* long tubes each; they were placed next to the BIS chamber on a mechanical support. The two bundles were inserted in the setup to test the HV cured tubes (one of the two bundles) and to compare BIS pulse height results and also to test possible differences due to the on-chamber gas system, that was serial for the bundles, different from the fully parallel version of the BIS [11]. The bundles volume was 48 l.

The chamber and the bundles were mounted with the tubes in vertical direction and the setup was placed inside the GIF area (Figure 4.7) at a distance of ~ 1.5 m from the ^{137}Cs γ-source.

Figure 4.7: *A picture of the experimental setup in X5/GIF area.*

Both the bundles were equipped with ATLAS gas distribution system components and the 10k MDT prototype electronic boards that have an analog output, one every three channels. The first bundle, directly in front of the GIF source - from now on referred to as 'source side' bundle - was mounted in the support with the read-out side at the bottom, as the BIS chamber. The other one, made of reconditioned tubes, behind the first bundle, further from the source - from now on referred to as 'back side' bundle - had the read out side at the top.

The BIS chamber and only the source-side bundle were readout during weekly reference

runs; the back-side bundle, the one made of reconditioned tubes, did not acquire any data during the test, but only the current was monitored to check its behaviour.

This bundle on the back side did not acquire any data during the test, but only the current was monitored to check its behaviour. The mechanical support had a moving part controlled by two step motors, for horizontal and vertical movements. Two ^{241}Am sources with an activity of 36.5 MBq each were placed on the moving part and were used to take weekly reference runs to monitor the pulse height. It was decided to use ^{241}Am sources to irradiate only small parts of tubes and to study the correlation between pulse height and position along the wire.

The sources were enclosed in a metallic shielding with a slit collimating γs in a small area in the vertical direction (~ 3 cm on the 4th layer, the further one). The collimation and the movement direction along the wire was of particular importance since the previous ageing study showed that a loss in pulse height might only be present in some part of the MDTs (within the first ~ 30 cm of the tube measured from the gas inlet in the previous test).

4.4.1 The Gas System and Slow Control

As mentioned above one of the main goals of the MDT ageing study is to test the circulating gas system foreseen for ATLAS (Par 3.1.3).The prototype system built for testing and evaluation at GIF uses the final ATLAS gas circulator, a custom-designed high speed compressor type ATC, together with a specially designed gas system setup which allows simulation of the later ATLAS operation.

The off-chamber gas system is the same as the one used in the previous ageing test and the details of the gas system setup itself and its associated slow-control system are reported in [12]. The main difference in the 2004 setup is related to the absence of one of the BIS multilayers and the introduction of the two bundles.

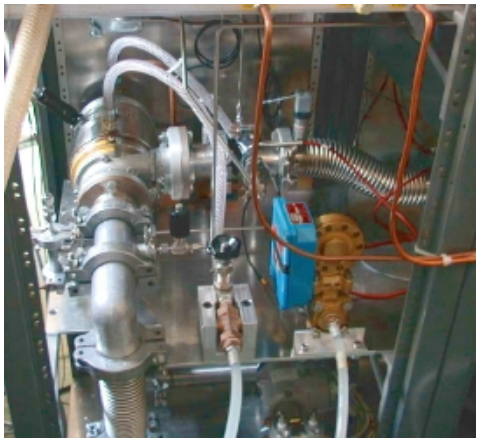

Figure 4.8: *The ATC installed in the MDT test system at GIF.*

The gas mixture used, Ar:CO_2 (93 : 7) was provided as premix in batteries. The gas racks were installed outside the GIF area and two pipes brought the gas inside GIF: one line was used to supply gas to the BIS, the other one supplied gas to the two bundles in series. Both the BIS and the bundles have operated in gas recirculation mode, using the final ATLAS

Parameter	Value
Nominal gas flow	100 Nm^3/h
Max. flow rate	200 Nm^3/h
Gas pressure at inlet	$\sim$ 2.9 *bar*
Gas pressure at outlet	$\sim$ 3.2 *bar*
Max. power at full speed	2.5 kW
Max. speed	55000 rpm

Table 4.1: *Operation parameters of the ATC gas circulator.*

Argon Turbo Circulator, ATC, which comprises a high speed turbine running at up to 55000 rpm. Figure 4.8 shows the ATC compressor after installation in the MDT tests setup at GIF. The main difficulty in building an appropriate down-scaled test setup was the adjustment of the ATC gas flow to a much smaller system than the full ATLAS muon spectrometer. To solve this problem, the recirculation prototype included a bypass loop with a 200 l buffer volume in order to run the ATC at its nominal gas flow of $100Nm^3/h$ (inside the loop), while it was connected to the BIS and the bundles (representing a tiny fraction of the full ATLAS volume) to be operated at a much lower gas flow ($50 - 100$ Nl/h).
The operating conditions were such that 10% of the gas passing through the chambers was replaced by fresh gas in each cycle. The gas flow through the chambers was 2 volume exchanges per day for a first period of the test, i.e. 50 Nl/h, and 4 volumes exchanges per day in the second period of the test (from the March, 10^{th}), i.e. 100 Nl/h. The irradiated gas returning from the chambers was diluted in the ratio 1:1 with the gas present in the buffer volume of the recirculation system, before being recirculated itself. Table 4.1 summarized the main characteristics of the ATC circulator.

The BIS on-chamber gas distribution system was fully parallel, i.e. each tube was separately supplied with the operating mixture from the gas manifold ("gas bar") by a small stainless steal tubelet (see Par. 3.1.4 Figure 3.5). The gas inlet was in the bottom part of the chamber, on the read out side.
The bundle on-chamber gas distribution system was serial, i.e. the six tubes in each layer were connected in series, the gas inlet was on the first tube of the layer, the gas outlet was on the sixth one, while the four layers were connected in parallel. The two bundles themselves were also in series, i.e. the gas input from the gas rack came into the first bundle while the second bundle, on the back side, received as input the gas from the output of the first one.

The slow control system was very similar to the one of the previous test. All the gas system parameters - flows, pressures, temperatures - were monitored and if one or more monitored values went out of range the system automatically stopped and remained in a safe state. The gas system was interlocked with the HV supply in order to switch off the HV if the gas flow stops. Ten temperature sensors mounted on the chambers were acquired every minute and used in data off-line analysis to apply temperature correction. The control panels of two slow control programs are shown in figures 4.9 and 4.10.

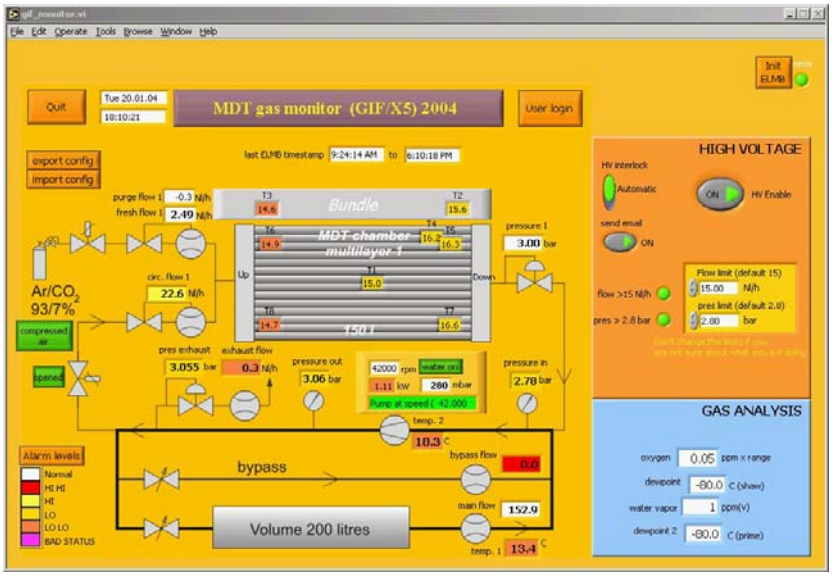

Figure 4.9: *A picture of the gas system slow control panel. In the middle the chamber outline and on it the temperature sensor placement.*

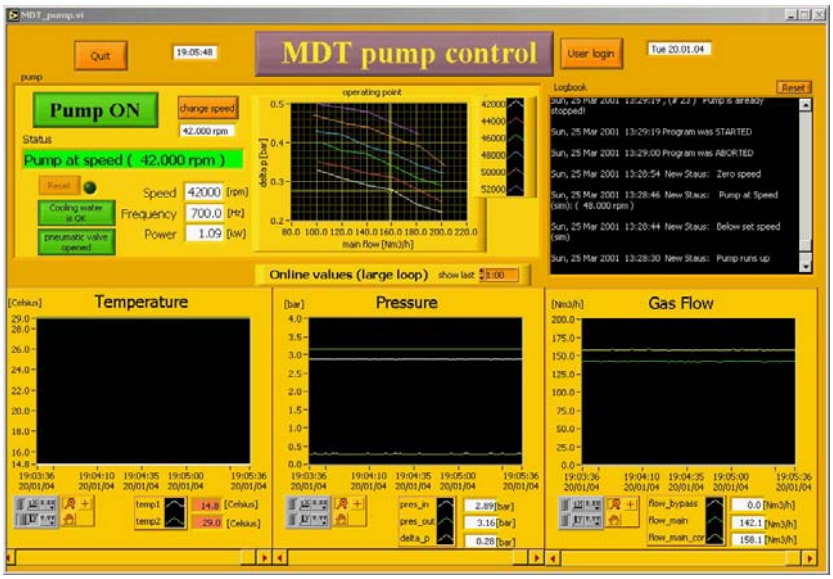

Figure 4.10: *A picture of the ATC pump control panel. The pump control program, inherited from the previous test, allows a secure and stable operation of the ATC under different rotation speeds.*

The HV monitoring was performed via a CAENET interface to the CAEN SY127 power supply through CAEN A128HS - high speed CAENET communication controller module and CAEN V288 - high speed CAENET VME controller module. The values of voltage and current were acquired every minute by the PC dedicated to the DAQ and automatically transferred to a storage area on Lxplus; they were also displayed on a web page for monitoring.

4.4.2 Front-End Electronics and DAQ

The chambers were equipped with the ATLAS MDT electronic boards : HV and RO hedgehog boards and mezzanine lites. The use of the mezzanine lites instead of the final mezzanines was due to the little sensitivity with respect to gain changes when using the octal ASD Wilkinson ADC [13]. In order to have a proper measurement of gain loss with the final mezzanine, since it is not possible to integrate the full length of the signal due to the bipolar shaping applied on it, it was tried to use the information stored in the Wilkinson ADC, that integrates the signal in a programmable gate from 8 to 45 ns. The signal of a small ^{109}Cd γ -source (85% 22 keV, ~ 60 kBq) illuminating one tube was acquired using the standard electronics parameters configuration (gate 15 ns, rundown current 4.5 μA, threshold -44 mV) and simulating the variation of gain by decreasing the high voltage. The Wilkinson ADC spectra that we obtained are showed in figure 4.11-*left*. As cross-check, we did the same test with cosmic muons. The Wilkinson ADC spectra that we obtained for cosmic muons are showed in figure 4.11-*right*.

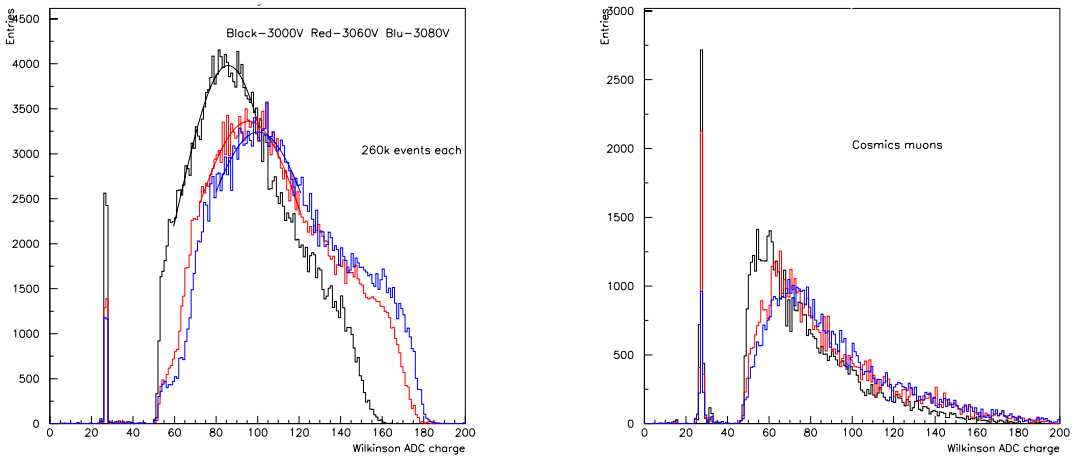

Figure 4.11: ***On the left:*** *Wilkinson ADC charge spectra obtained for a* ^{109}Cd γ *source at different high voltages. The "shoulder" on the right of the spectra is probably due to saturation in the capacitor used to store the integrated charge.* ***On the right:*** *Wilkinson ADC spectra for cosmic muons at different high voltages.*

To understand the sensitivity on this measurement of gain loss, the variation of the peak position was compared to the expected variation of gain as reported in [14] at different high voltages. The results are shown in figure 4.12, proving that the sensitivity in pulse height was significantly reduced when integrating only the rising edge of the signal with the octal ASD.

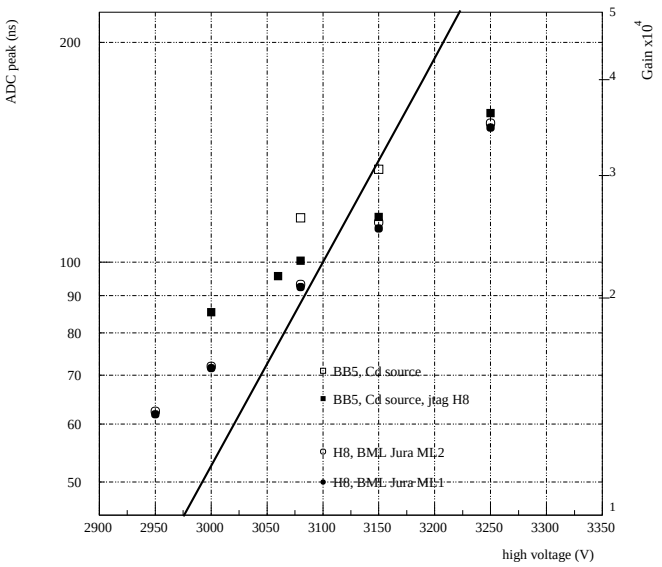

Figure 4.12: *Wilkinson ADC reading versus HV for low energetic photons (^{109}Cd source) and for muons (H8 data). The two types of squares indicate the measurements of pulse height with two different gates. The solid line (right axis) is the change in gain expected from Diethorns formula [14].*

Other tests were done changing Wilkinson ADC parameters to improve the measurement, but these showed similar results. These preliminary tests proved that in order to have a proper measurement of gain reduction (differences of about 5-10%), it was better to integrate the full signals (Figure 4.18) instead of the rising edge (15-20 ns) only. So it was decided to use the debugging analog output provided on each mezzanine ASD-lite card for every third channel. The position of tubes with an analog read out is shown in figure 4.13.

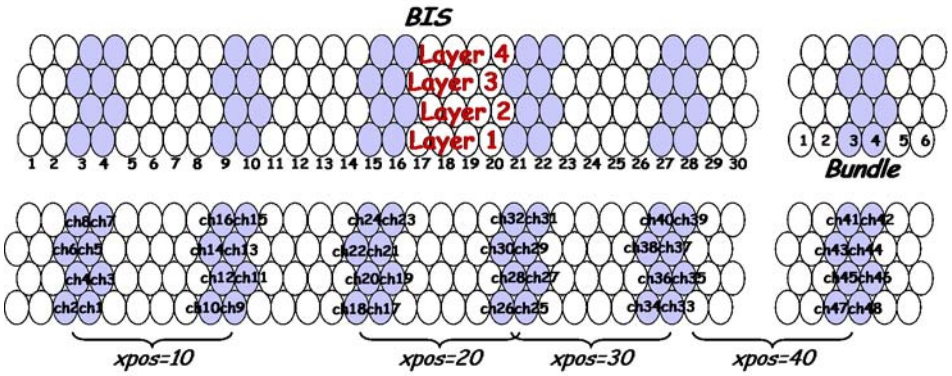

Figure 4.13: *This scheme shows the acquired tubes in a different colour, eight tubes for each mezzanine card. The number of ADC channel is also reported on the second schema on the bottom and the same name convention is used afterward.*

The analog outputs of 48 tubes were sent to charge integrating ADCs - CAEN V792 module, 32 Channel Multievent Charge ADC (32 ch., 12bit, 400 pC max charge) - and integrated a gate of 500 ns in order to perform pulse height measurements. For this the differential analog signals provided by the mezzanine cards were transformed into single ended signals by a set of pulse transformers. These signals were carried out of the X5 zone with 80 m long BNC cables and fed into custom-made splitters. One of the two outputs of the splitter was delayed

of 75 ns and it was sent to the CAEN V792 ADC, the other was sent to a discriminator. The discriminators outputs were sent to coincidence units and then to the 500 ns gate generator which drives the ADC. The scheme is shown in figure 4.14.

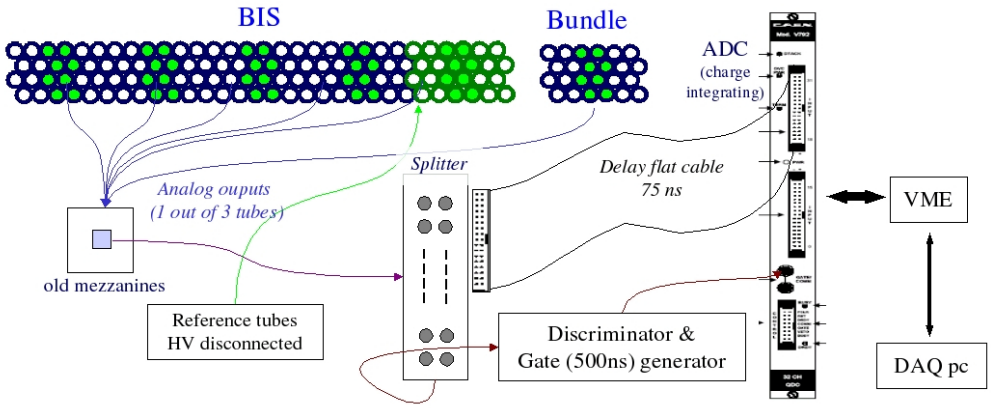

Figure 4.14: *The trigger scheme.*

A set of 24 tubes (a whole mezzanine) was disconnected from HV during the GIF γ-irradiation (the last hedgehog card - tubes from 25 to 30 - on BIS chamber). The eight read out tubes on this mezzanine were used as a reference to monitor the pulse height in order to control changes in gas gain due to temperature effects, or other effects, different from ageing effects.

The bundle on the back side was not read out, but only its current - integrated charge - was registered. This bundle was made of tubes which drew current during production QA/QC (Quality Assurance and Quality Control) tests and which were cured (HV curing procedures) leading to normal current values afterwards. It was decided to test this kind of tubes in this setup to compare its behaviour with the other identical bundle made of "normal" tubes.

The VME crate housing the ADC modules was interfaced to a PC running Windows operating system via National Instruments VXI-MXI bus. The DAQ software was developed to acquire data and to monitor the HV. Data was taken once a week when the GIF source was off, during the remaining time (about 6.5 days per week) the values of voltage and current were acquired every minute and transferred to the test storage area on Lxplus by the DAQ software. The main DAQ control panel also included the interface to guide the step motors moving the ^{241}Am-sources. The control of the step motors was realized using the MIND S controller through the serial port of the DAQ pc. The serial driver interface and the motor control services were integrated in the DAQ library. The position accuracy of the motorized sources was $\sim$ 0.5 mm in the vertical direction and $\sim$ 1 mm on the horizontal direction. Figure 4.15 shows the DAQ control panel.

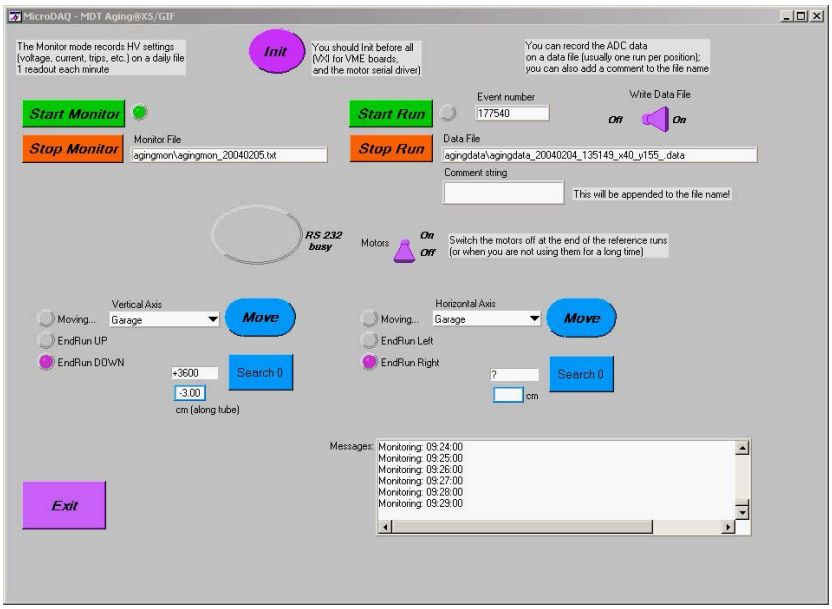

Figure 4.15: *The control panel of the DAQ software, which is written in National Instruments LabWindows-C for Virtual Instrumentation language.*

4.5 Data taking

^{241}Am γs were used to monitor the chamber performances in weekly reference runs with the GIF ^{137}Cs source switched off (in the GIF area it is possible to "switch off" the radioactive source moving it into a lead housing).

Data were taken from the 28^{th} of January to the 28^{th} of April 2004 once a week. During all the remaining time the chambers were irradiated by the GIF ^{137}Cs source. The weekly data consists of runs of about 350000 events, when the ^{241}Am sources irradiate two mezzanine at the same time (16 tubes acquired), and of about 175000 events, when the ^{241}Am sources irradiate one mezzanine (8 tubes acquired), to have at least 10000 events per tube. Data were taken with the ^{241}Am sources at different positions along the tubes and the sources were also moved on the horizontal axis in four different positions to irradiate all the acquired tubes (see Figure 4.13 and Table 4.2). Further data were acquired after the irradiation (the "ageing period") was stopped:

- there was a second period of data taking from the 29^{th} of April to the 3^{rd} of May, during which all the tubes of the BIS chamber, not read out before, were acquired. To allow these measurements the BIS mezzanines were displaced, respect to their usual position, by two tubes on the left (to read out the tubes number 1, 2, 7, 8, 13, 14, 19, 20, 25, 26 of each layer), and by two tubes on the right (to read out the tubes number 5, 6, 11, 12, 17, 18, 23, 24, 29, 30 of each layer). The X-pos of the sources were modified in order to irradiate those tubes.

- there was a third little data taking period from the 6^{th} to the 7^{th} of May, after the dismantling of the mechanical setup. A complete set of runs like the ones in the first period was acquired with the BIS chamber in horizontal position outside the GIF area as cross-check. The aim was to verify that the observed effect was not due to some kind of dust in the bottom part of the tubes for gravitational effect.

4.5.1 Accumulated Charge

The charge accumulated by the BIS chamber and by the two bundles is shown in figures 4.16 and 4.17.

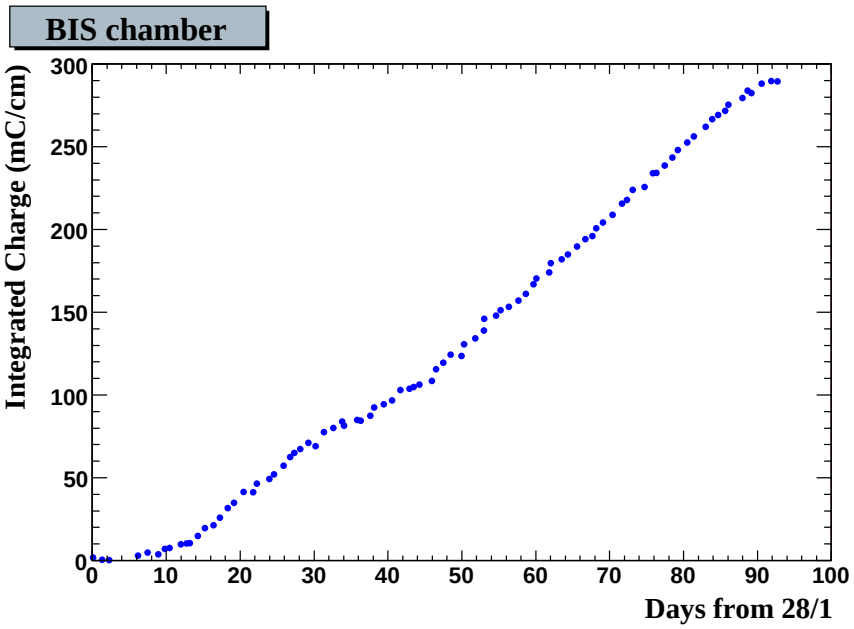

Figure 4.16: *Integrated charge in mC/cm for the BIS.*

During the first two weeks of test the high voltage was set to the standard operating value of 3080 V, that corresponds to a gain of 2×10^4. Then the high voltage was set to 3400 V (that correspond to a gain of about 8×10^4) to increase the accumulated charge, and so, to accelerate the ageing processes.

The maximum accumulated charge in 10 years of LHC operations is 600 mC/cm, calculated including a safety factor 5 to allow for uncertainties in the background simulations (Par. 3.3.1). A charge of 290 mC/cm was collected by BIS until the end of the measurements corresponding to about 50% of the LHC requirement.

The two bundles were slightly out of the irradiation cone of the GIF source, so they accumulated less charge than the BIS chamber. The same integrated charge of $\sim$52 mC/cm was accumulated by the two bundles, as the plot in the figure 4.17 shows. This is a good result for the 'back side' bundle made of "HV cured" tubes, confirming the normal working

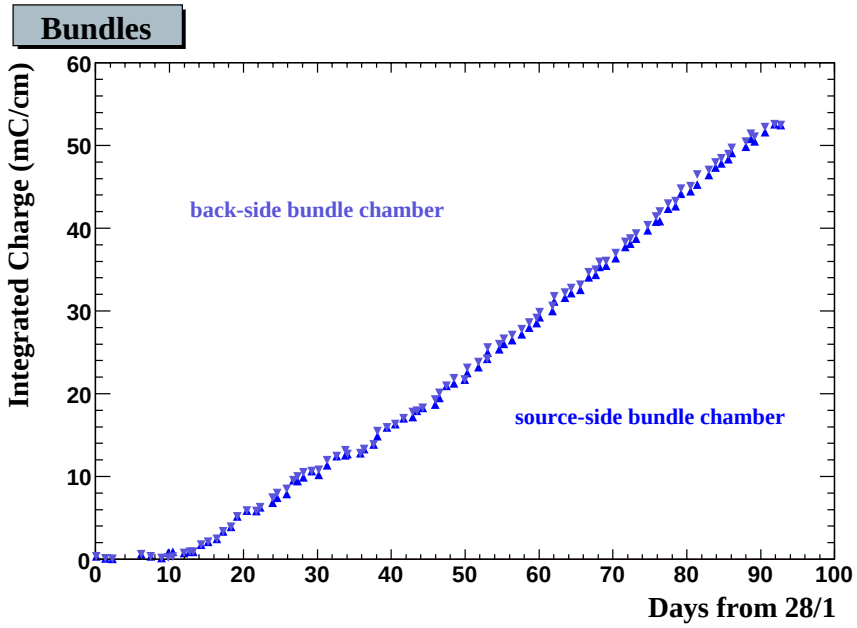

Figure 4.17: *Integrated charge in mC/cm for the two bundle chambers.*

behavior of this kind of tubes.

4.5.2 Weekly Reference Runs

As already mentioned, the performance of the chambers was monitored during the ageing study by weekly reference runs using two ^{241}Am sources. Apart from α particles, readily absorbed and undetected, ^{241}Am emits photons (Figure 4.18) at different energies, the most energetic ones are 60 keV photons corresponding in the spectrum (Figure 5.2) to the largest peak on the right; referring to the same figure, the first narrow peak on the left is the pedestal and the peaks in the middle correspond to the less energetic photons emitted by ^{241}Am (14 keV, 35 keV). The ADC value of the 60 keV peak was used to monitor the gain variations.

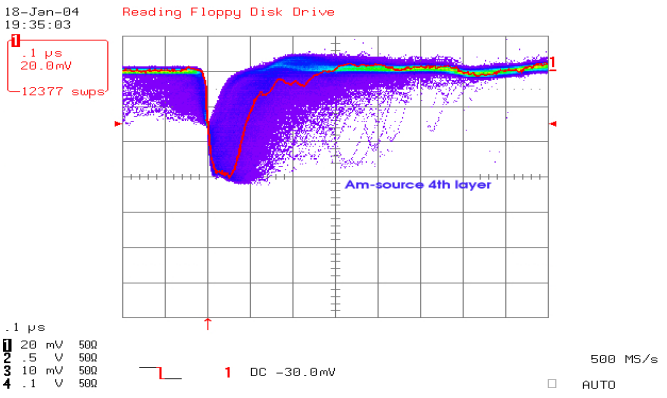

Figure 4.18: *The signal generated by the ^{241}Am on a tube of the fourth layer. The oscilloscope scales are 20 mV and 0.1 μs. The threshold is set to -30 mV, the same value of the discriminators threshold. The violet-blue gradient is proportional to the persistency of the signals.*

As it was said before, it was possible to move the two step motors to different positions and table 4.2 shows the positions studied systematically during the data taking.

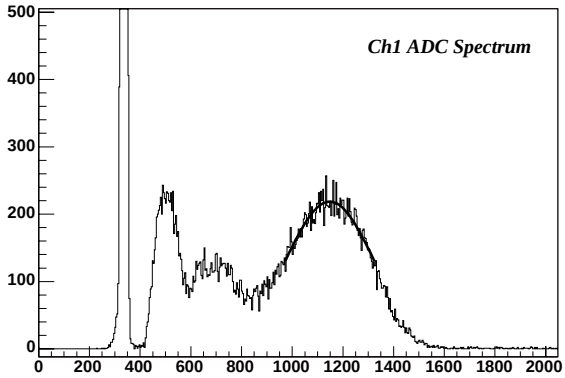

Figure 4.19: *An example of ADC spectrum.*

The two ^{241}Am sources were positioned 10 *cm* far from the first layer of tubes and a collimator was positioned in front of each source. The collimators were built so that only ∼3 *cm* of wire were irradiated on the fourth layer, which is ∼18 *cm* away from the source. On the coordinate along the chamber width no collimation was done, so 6 tubes on the fourth layer were irradiated simultaneously. The distance between the center of the two source collimators mounted on the mechanical support was 18 *cm*, in order to simultaneously irradiate two pairs of readable tubes on the BIS chamber. A summary of the studied positions, and the ADC channels involved in each position, is listed in table 4.2.

X-pos 10		**X-pos 20**		**X-pos 30**	**X-pos 40**
Mezzanine1	Mezzanine2	Mezzanine3	Mezzanine4	Mezzanine5	Mezzanine6
Lay. 1,2,3,4 Tubes 03,04 BIS	Lay. 1,2,3,4 Tubes 09,10 BIS	Lay. 1,2,3,4 Tubes 15,16 BIS	Lay. 1,2,3,4 Tubes 21,22 BIS	Lay. 1,2,3,4 Tubes 27,28 BIS	Lay. 1,2,3,4 Tubes 3,4 bundle
Y-pos (for each X-pos) **0, 2, 5, 8, 10, 12, 15, 25, 35, 55, 85, 120, 155, 158, 161** cm from gas inlet					

Table 4.2: *The ^{241}Am sources positions during the weekly reference runs (see Figure 4.13).*

The X-pos 10 and 20 illuminated two mezzanines together, while the X-pos 30 and 40 only one each. This was due to the fact that the distance between the last mezzanine of the BIS and the mezzanine of the bundle was ∼10 *cm* more than the distance between two close mezzanines of the BIS. The Y-pos at 0 and 161 cm corresponded to the position of the crimps of the endplugs. For time reasons not all the Y-pos were taken all the weeks, in particular we added the Y-pos at 0, 2, 8, 10, 12, 158 and 161 only after degradation of pulse height, close to gas inlet side, was observed in three tubes. Thus some Y-pos in the middle of the tubes were excluded because the gain in the middle region was stable.

Each data run was processed by a C++/ROOT program to fill histograms. The program

also fitted the pedestal peak and the $60keV$ peak and it produced an ASCII file with these informations for the off-line analysis.

The first step of the off-line analysis consisted in the calculation of the integrated charge Q_{60keV} corresponding to the position of the $60keV$ peak evaluated after pedestal subtraction:

$$Q_{60keV} = Q_{peak} - Q_{ped} \tag{4.1}$$

The value Q_{60keV} was then corrected for temperature effects and it was correlated with the coordinate along wire.

4.6 Normalization and Corrections

A series of systematic studies was performed before starting the actual ageing test, to check the linearity and to measure the sensitivity of the system, and during the analysis to find the right way to correct data for systematic effects, like those due to temperature changes.

4.6.1 System linearity and sensitivity

To understand the sensitivity of the full system, a variation of gain was simulated with an external variable attenuator. It was mounted before the splitters in order to simulate also the possible variations in the number of triggers generated by that channel. The variations of the pulse height spectrum is shown in figure 4.20, where the spectrum generated by signals without attenuation (coloured in red) is plotted together with the spectrum generated by signals attenuated of 1 dB (coloured in black). The results of the measured attenuation for different values of the attenuator are reported in figure 4.21.

The statistical error on each data point was between 0.8% and 1.1% of the value. The overall system sensitivity for the detection of a loss of gain was estimated around 3%. The fit parameters of the data show that the system overestimated the gain drops, thus this correction was applied:

$$\Delta G_{true} = \frac{\Delta G_{measured} + 0.264}{1.269} \tag{4.2}$$

4.6.2 Off-line Corrections

The gas gain G of a MDT is highly dependent on voltage and on gas density, that is pressure and temperature, according to Diethorn' formula (Par. 3.2.1 Equations 3.6 and 3.7).
So the voltage and the pressure were monitored and remained stable inside the given range, since the voltage was kept constant from the high voltage power supply and the pressure from the pressure regulators inside the gas circulation loop, so the only source of gain variation was temperature.

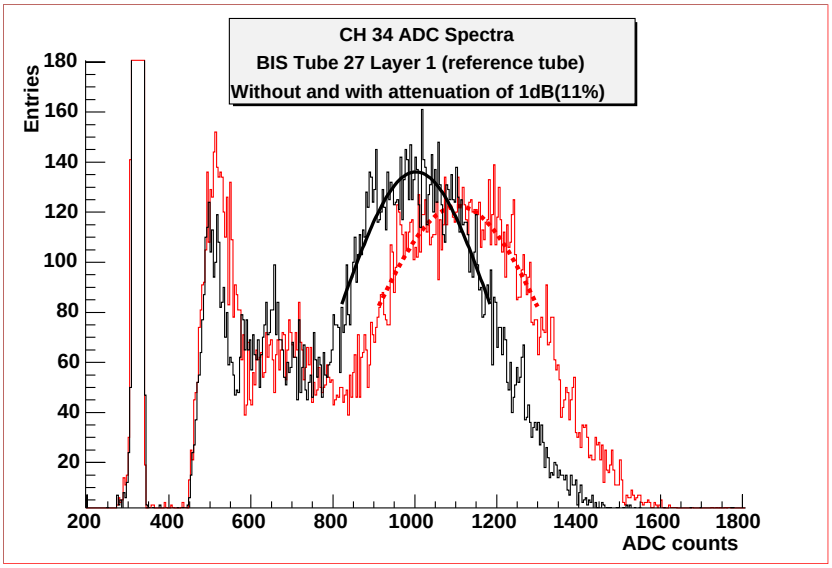

Figure 4.20: *Two superimposed pulse height spectra. The red one is the ADC spectra of the signal without attenuation, the black one corresponds to an attenuation of 1 dB (11%).*

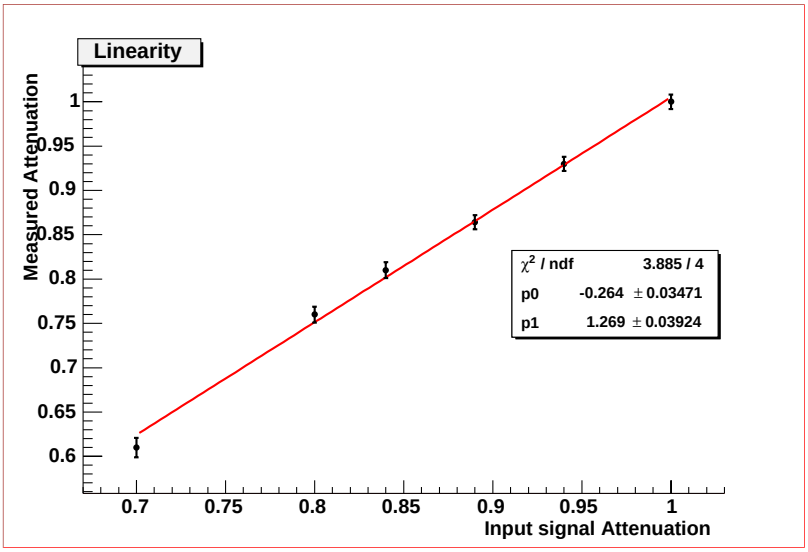

Figure 4.21: *Measured attenuation of the 60 keV peak versus the value of the attenuator added in the setup. The statistical errors are shown on the data points.*

The relation between temperature variations and gas gain variations for the MDT gas mixture, Ar:CO_2 (93 : 7) is([1])

$$\frac{\Delta G}{G} = 9.86 \cdot \frac{\Delta T}{T} \tag{4.3}$$

which corresponds to a gas gain variation of 3.3% per temperature degree.

Using the monitoring temperature data from the ten sensors placed on chambers, all measured pulse height data were corrected off-line. Figure 4.22 shows the temperature behavior during the day in the experimental area.

The variation of temperature during all the test is shown in figure 4.23 as a function of the time.

The temperature behaviours taken into account were:

• The variation of the external temperature during the test over a period of ∼100 days: it is of the order of 10 C^o, as it is shown in figure 4.23. This is a global effect, in fact the temperature of the different sensors varied together and their differences remained approximately constant (Figure 4.23).

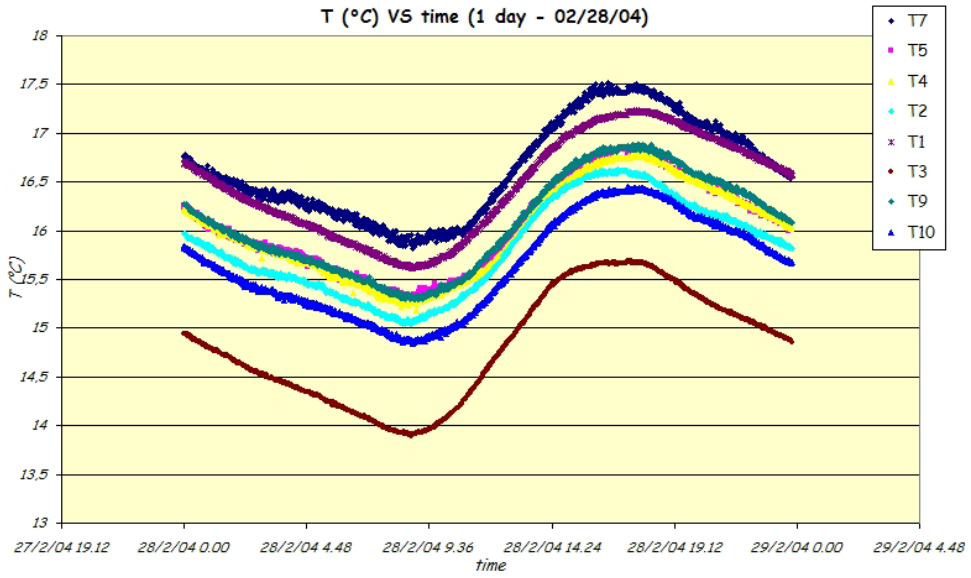

Figure 4.22: *Temperatures in °C of nine sensors on the BIS chambers versus time relative to a day of March. The difference from the highest temperature and the lowest one was about 1.5° in a day.*

• The vertical temperature gradient due to the presence of electronics (read-out and HV side) and mainly due to the closer space in the bottom part of the chamber. The maximum temperature difference along the tubes was about 1.5° (1° gradient was in the first 30 *cm*) as

[1] calculated using Diethorn parameters: $E_{min} = 24\ kV/cm$ and $\Delta V = 34\ V$ from [14].

figure 4.25 shows.

• The horizontal temperature gradient; its behaviour was shown in figure 4.24 and in figure 4.23 where the $T7$ and $T2$ sensors were those positioned on the bottom left and bottom right of the setup and the the $T8$ and $T3$ sensors were those positioned on the top left and top right of the setup. The difference between left and right side was about 1°.

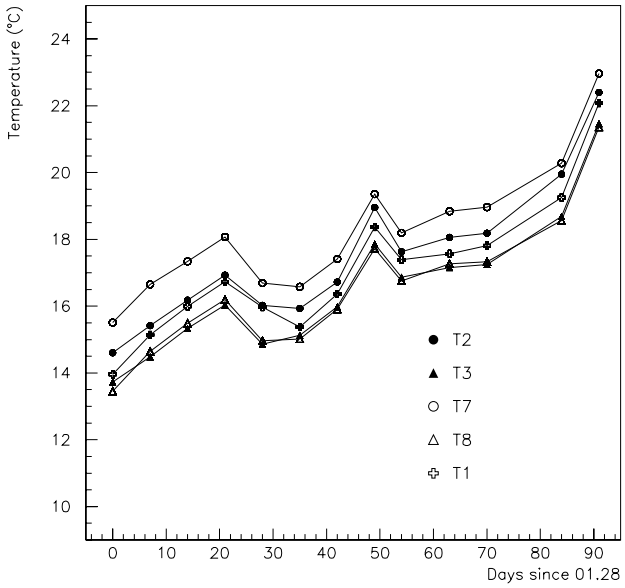

Figure 4.23: *Temperature of five sensors on the BIS and on the bundle as a function of days from the 28th of January. $T1$ is positioned on the center of the BIS, $T7$($T8$) on the bottom(top) left of the BIS, while $T2$($T3$) on the bottom(top) of the bundle. The difference from the highest temperature and the lowest one was about 8°C in the period of 3 months.*

Different algorithms were developed for the off-line temperature correction, the simplest one using only an average global temperature correction, while more complicated ones were position dependent.

From now on the 60 keV pulse height peak is considered as a function of the accumulated charge (q), of the tube ($tube$), of the position along the tube (Y) and of the temperature (T):

$$Q_{60keV}(q, Y, tube, T). \tag{4.4}$$

Intercalibration Factor Correction

The possible different response of the electronic chain (mezzanine, cables, ADC) was taken into account when comparing different tubes. So an intercalibration factor was defined as:

$$Intercalib(tube) = \frac{Q_{60keV}(q^0, Y, tube, T)}{Q_{60keV}^{meanYpos}(q^0, tube, T)} \tag{4.5}$$

where q^0 refers to the value at 0 mC/cm of accumulated charge.

Temperature corrections

- **Global and local temperature correction**

  In order to introduce also a local correction depending on the y coordinate, the functional dependence of the temperature as found from the fit shown in figure 4.25 was used.

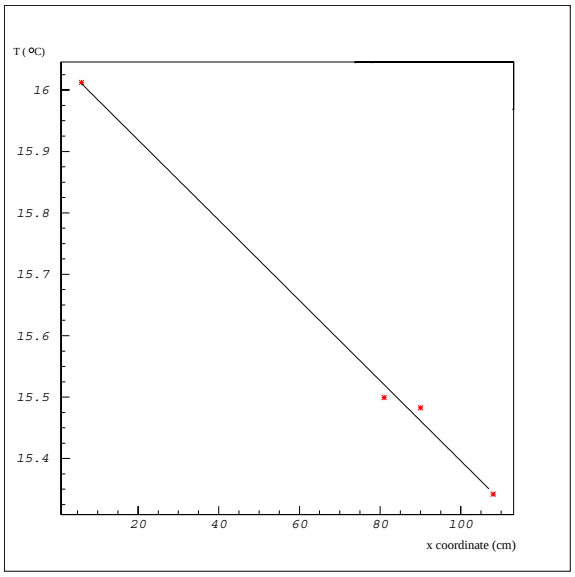

Figure 4.24: *The plots show the temperature in °C as a function of x position along the chamber width in cm.*

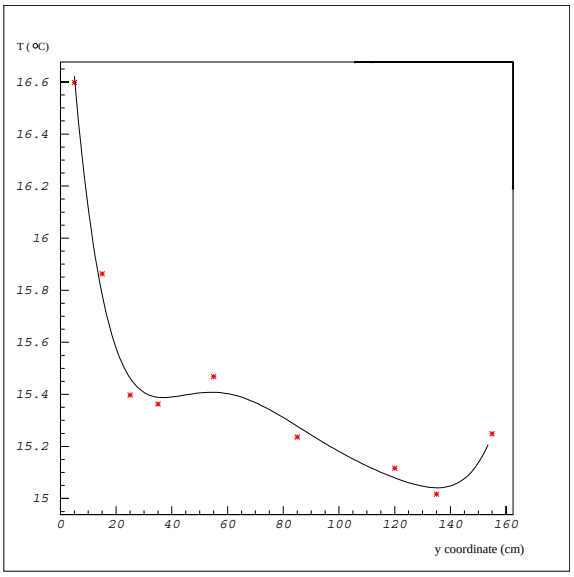

Figure 4.25: *The plots show the temperature in °C as a function of y position along the tube height in cm.*

The temperature was evaluated from the following relation, where also the dependence on the x coordinate has been introduced:

$$T_{corr} = [(T_7 - A \cdot x) - B \cdot y + C \cdot y^2 - D \cdot y^3 + E \cdot y^4 - F \cdot y^5 + G \cdot y^6] \tag{4.6}$$

where: T_7 is the temperature of one of the sensors taken as reference; A is the parameter of the linear fit on temperature values along chamber width; B, C, D, E, F and G are the parameters of the non linear fit on temperature values along wire direction.

The slow control temperature data, acquired every minute, were used and different set of parameter were produced for each 15 days period, according to the external temperature variation. In this way the position of the 60 keV peak was corrected to the temperature of 300 K multiplying it for a factor:

$$Q_{60keV}^{corr} = Q_{60keV} \cdot corr \tag{4.7}$$

where the multiplying factor $corr$ is:

$$corr = 1 - 9.86 \cdot \frac{T_{corr}(K) - 300K}{300K} \tag{4.8}$$

- **Simple global temperature correction**

  The slope α of the Q_{60keV} versus temperature for each channel and each Y-pos was fitted using data in a wide range of temperatures, as shown in figure 4.26.

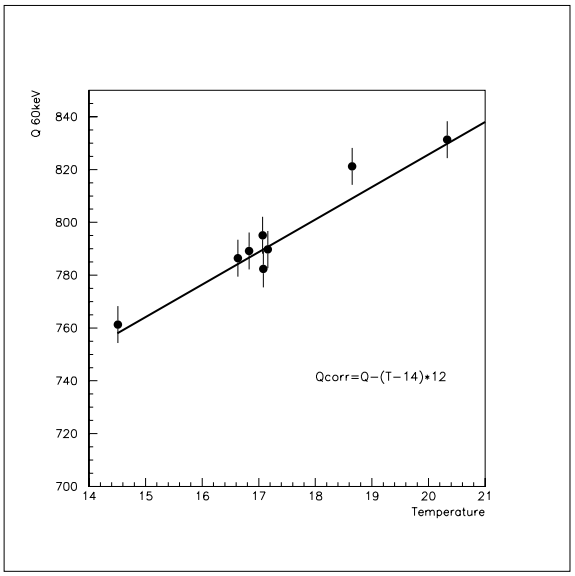

Figure 4.26: *Q_{60keV} as a function of the temperature for one channel at 85 cm.*

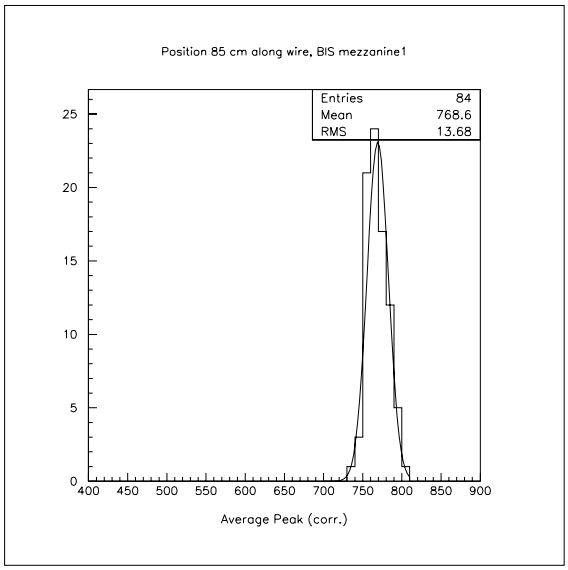

Figure 4.27: *$Q_{60keV}^{temp.corr}$ distribution for different tubes at 85 cm.*

We used the average of these fits as temperature correction factor at a reference temperature. Data were corrected to 14^oC (T_{start}), the average temperature when we started the test, using relation (4.9).

$$Q_{60keV}^{corr}(q, Y, tube) = Q_{60keV}(q, Y, tube, T) \cdot [1 + \alpha(T - T_{start})] \tag{4.9}$$

The global effect of the corrections can be evaluated from figure 4.27. We plot the values of Q_{60keV}^{corr} for Y=85 cm from all the tubes of a mezzanine for the complete data taking period. The relative width of the distribution is $\sigma/mean \sim 2\%$.

Both the temperature corrections result accurate enough for the pulse height studies.

4.7 Analysis

Data were analysed looking at corrected pulse height values of each tube relating them to the position along the wire (the results are shown in Par. 4.7.1) or to the accumulated charge (the results are shown in Par. 4.7.1).

There were two possible approaches to clearly show the gain variations:

- Each tube could be compared to one of the reference tubes (HV disconnected during GIF irradiation so no accumulated charge). For each Y-pos as a function of the accumulated charge, or for each accumulated charge as a function of the Y-pos, the ratio:

$$R_1 = \frac{Q_{60keV}^{temp.corr}(q, Y, tube)}{Q_{60keV}^{temp.corr}(q^0, Y, tube^{Ref})} \tag{4.10}$$

  could be plotted. Using this method the intercalibration factor correction has to be applied because data from two different tubes were compared, and the global and local temperature correction have been applied to take into account the temperature gradients along the chambers height and width.

- The relative variation of gain of each tube and for each position along the wire could be studied as a function of the integrated charge. Thus, for each Y-pos, the ratio:

$$R_2 = \frac{Q_{60keV}^{temp.corr}(q, Y, tube)}{Q_{60keV}^{temp.corr}(q^0, Y, tube)} \tag{4.11}$$

  could be plotted as a function of the integrated charge. To compare pulse height measurements at different position along the wire we can also plot the numerator of (4.11) as a function of Y-pos. In this way the results are not dependent on the reference tubes.

If no gain drops were measured then both the ratios should have 1 as expected value ($R_1 = R_2 = 1$). It was observed that the two explained methods gave compatible results, so it was decided to use the second one because it is simpler to implement, and because each measurement depends only from a single channel and not from the behaviour of the reference tubes.

From now on, we refer to the results coming only from the BIS tubes, unless explicitly explained, since the bundle accumulated too few charge to compare its results to the BIS ones.

4.7.1 Analysis Results

Pulse Height versus Position along the Wire

Four weeks after the beginning of the irradiation, corresponding to about 68 mC/cm of accumulated charge, three tubes on the third layer (tube4-ADC channel 5, tube10-ADC channel

13 and tube16-ADC channel 21) have shown ageing effects in the first few centimeters of the wire from the gas inlet side. Thus it was decided to add reference runs at different positions along the tubes height to improve measurements, as reported in table 4.2.

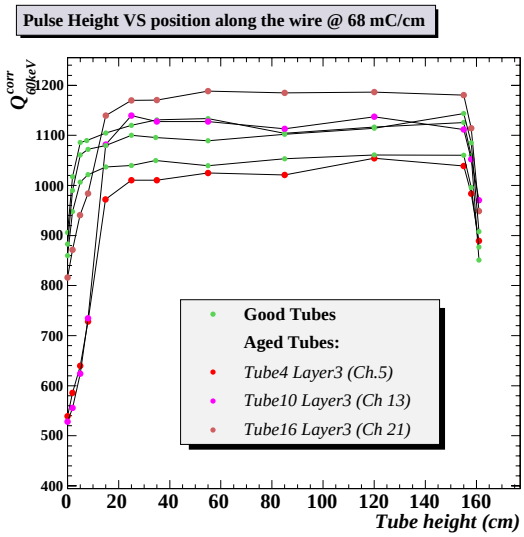

Figure 4.28: *Pulse height $Q^{temp.corr}_{60keV}$ as a function of the position along the wire, at an integrated charge of 68 mC/cm. The drops in the first and last two centimeters were due to the electric field distortion in the regions next to the MDT end-plugs.*

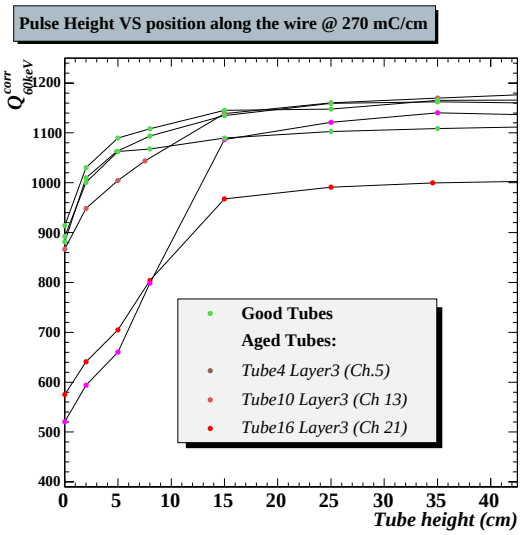

Figure 4.29: *Pulse height $Q^{temp.corr}_{60keV}$ in the first 40 cm from the gas inlet, at an integrated charge of 270 mC/cm.*

The figure 4.28 shows the behaviour of the three affected tubes as a function of the distance from the gas inlet, compared with other tubes that didn't show ageing effects up to February, 25^{th} (68 mC/cm of integrated charge). In figure 4.28 the pulse height drops at the begin and at the end of the tubes, equal for both sides and for all the tubes, were due to distortion of the electric field in the regions next to the MDT end-plugs. The drop behaviour is different for the three affected tubes in the gas inlet side. The figure 4.29 shows the pulse height as a function of the distance from the gas inlet in the first 40 cm up to April, 21^{st} (270 mC/cm of integrated charge).

In figure 4.30 it is shown the behaviour of one of the three affected tubes (tube 10-ADC channel 13) in the first 40 cm for different integrated charges. The ageing stopped after 70 mC/cm and only the first $10 \div 12$ cm were affected as figures 4.28, 4.29 and 4.30 show. It was not possible to be more accurate in evaluating the zone affected by ageing because the BIS wire zone illuminated by the ^{241}Am γs was $\sim$3 cm long due to the mechanical construction of the collimators.

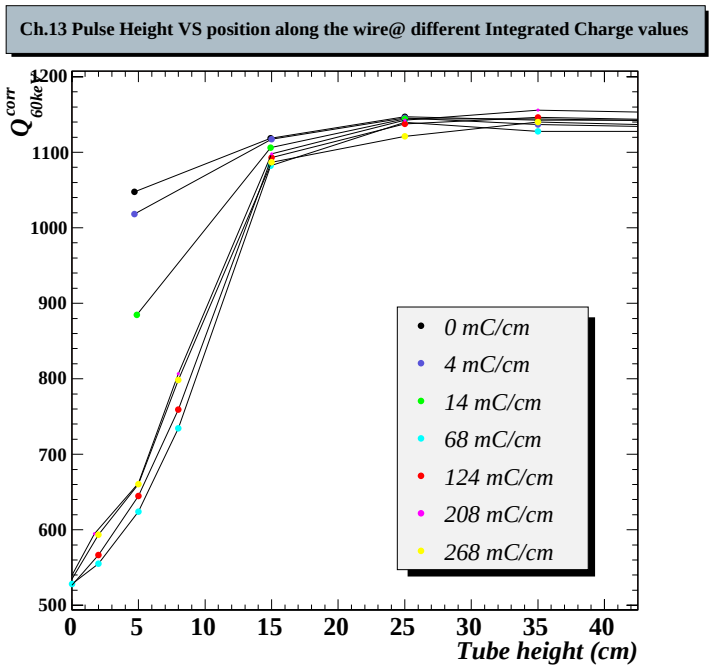

Figure 4.30: *Pulse height $Q_{60keV}^{temp.corr}$ over the first 40 cm from the gas inlet, at different integrated charges for tube 10 in layer 3 (Ch.13).*

Pulse Height versus Accumulated Charge

During the test period only 3 tubes out of 40 monitored (32 irradiated, 8 reference) have shown an ageing effect. No reference tube has shown reduction in pulse height, as expected.

The three affected tubes are tube 4 (ADC channel 5), tube 10 (ADC channel 13) and tube 16 (ADC channel 21) in the third layer; the pulse height, measured once a week, started to drop right after establishing irradiation and it decreased until about 70 mC/cm of integrated charge; at that point the pulse height became constant and stayed on a plateau (60÷90% on the original value), and the effect was visible only at Y-pos=5 cm. For the three affected tubes $Q_{60keV}^{temp.corr}$ at Y-pos=5 cm is shown in figure 4.31 as a function of the integrated charge. Also three of the remaining 29 irradiated tubes that did not show any ageing effect are plotted.

The pulse height remained stable even after the gas flow was changed from 2 volumes per day to 4 volumes per day on March, 10^{th} (110 mC/cm). The behaviour of $Q_{60keV}^{temp.corr}$ as a function of the integrated charge and the y coordinate was similar for all the three affected tubes. In particular, as a function of the y coordinate, the drop stopped at Y-pos=15 cm, while for greater Y-pos the behaviour is identical to all the other tubes (Figure 4.32).

In the gas outlet zone no ageing effect was found for any tubes (Figures 4.33, 4.34, 4.35 and 4.36).

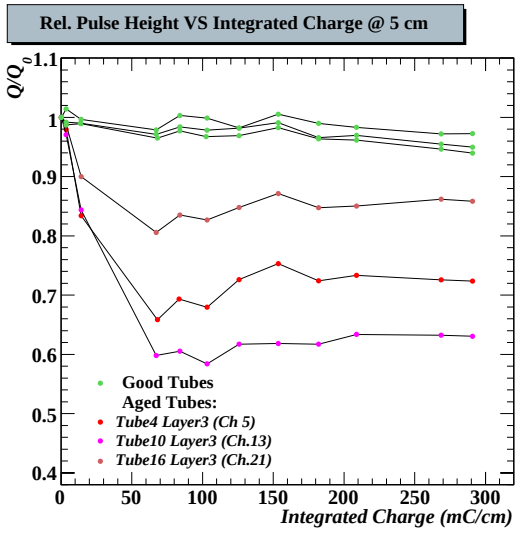

Figure 4.31: *Pulse height $Q_{60keV}^{temp.corr}$, relative to $t = 0$, as a function of the integrated charge at 5 cm from the gas inlet.*

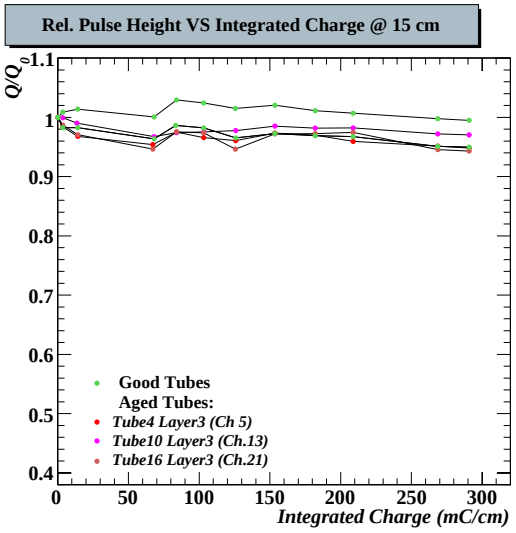

Figure 4.32: *Pulse height $Q_{60keV}^{temp.corr}$, relative to $t = 0$, as a function of the integrated charge at 15 cm from the gas inlet.*

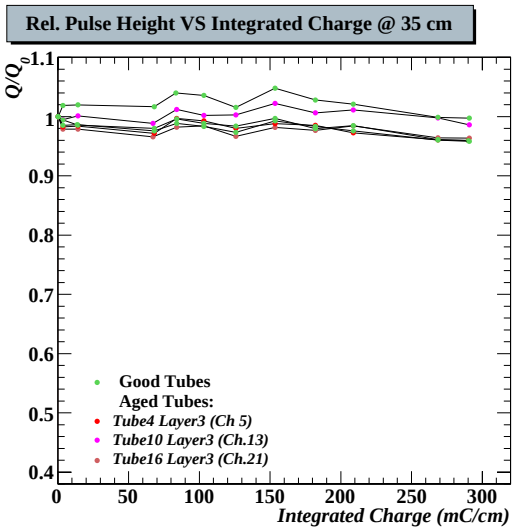

Figure 4.33: *Pulse height $Q_{60keV}^{temp.corr}$, relative to $t = 0$, as a function of the integrated charge at 35 cm from the gas inlet.*

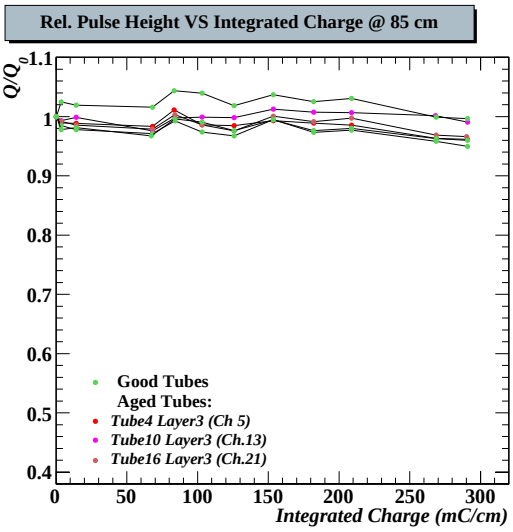

Figure 4.34: *Pulse height $Q_{60keV}^{temp.corr}$, relative to $t = 0$, as a function of the integrated charge at 85 cm from the gas inlet.*

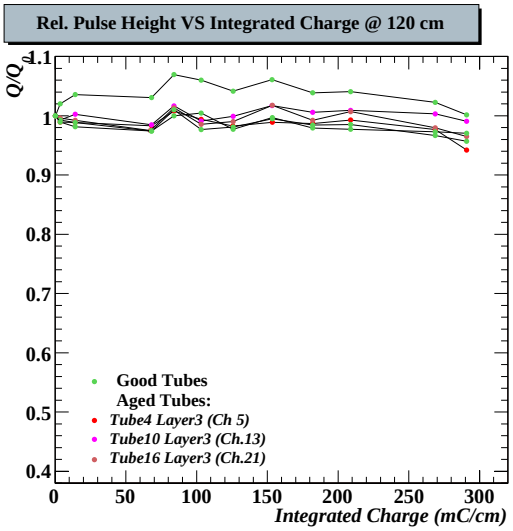

Figure 4.35: *Pulse height $Q_{60keV}^{temp.corr}$, relative to $t = 0$, as a function of the integrated charge at 120 cm from the gas inlet.*

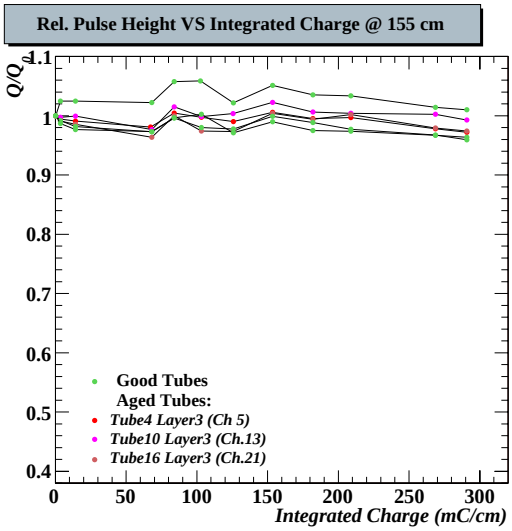

Figure 4.36: *Pulse height $Q_{60keV}^{temp.corr}$, relative to $t = 0$, as a function of the integrated charge at 155 cm from the gas inlet.*

BIS Final Runs

At the end of the first data taking period, after irradiation was stopped, the same kind of data were taken from all the tubes not read out before during irradiation period, by moving the hedgehog and mezzanine cards. The readout setup was modified as explained in par. 4.5.

The behaviour of 11 out of 64 tubes was found similar to the one shown by the three affected tubes. Also the Y-pos range of pulse height drop was consistent with the results shown in figures 4.28, 4.29 and 4.30. The three tubes studied during the test seem to be a good sample to describe the observed ageing effect.

The tubes with a proper functionality, after 290 mC/cm of integrated charge, were separated from the tubes with ageing effects, in terms of the variable $\Delta G/G$, defined in relation:

$$1 - \Delta G/G = \left(\frac{Q_{60keV}^{temp.corr}(5cm)}{Q_{60keV}^{mean}(15, 25, 35cm)} + 0.264\right)\frac{1}{1.269} \tag{4.12}$$

where the ratio between the $Q_{60keV}^{temp.corr}(5cm)$ and the average of the $Q_{60keV}^{temp.corr}(Y-pos)$ at 15, 25 and 35 cm from the gas inlet, was corrected for the linearity of the system to obtain the real gain reduction, as explained in equation (4.2), at 5 cm from the gas inlet.

Figure 4.37 shows the results for all the BIS irradiated tubes, giving an overview of the aged tubes on BIS chamber: 14 out 96 showed a $\Delta G/G > 5\%$. The effect was not uniformly spread over the four layers. None of the 24 reference tubes has shown ageing effects.

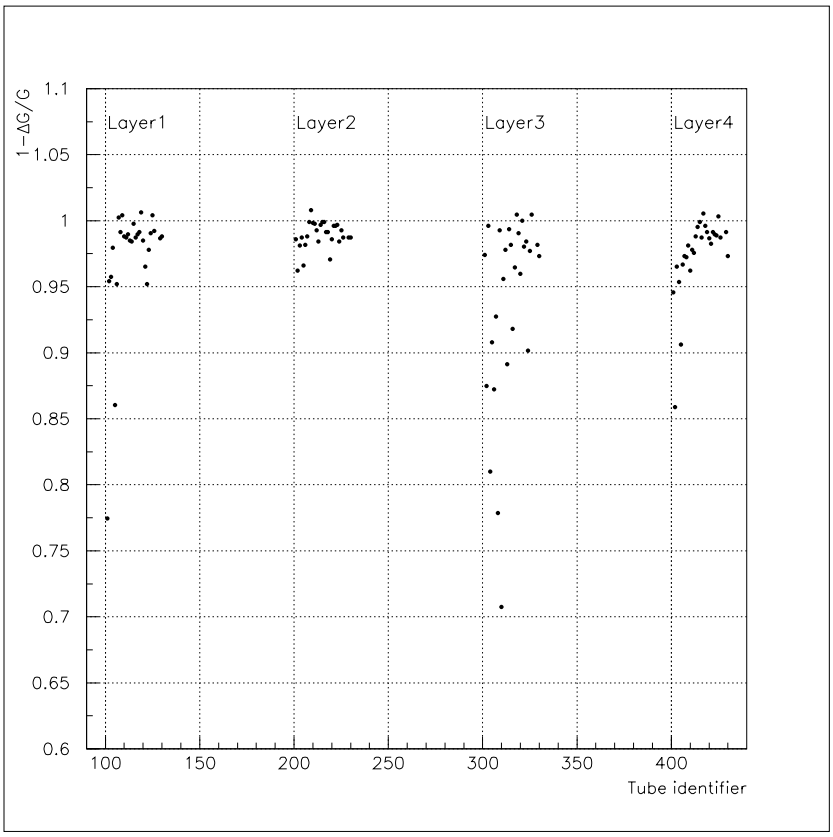

Figure 4.37: $1 - \Delta G/G$ *for the BIS tubes.*

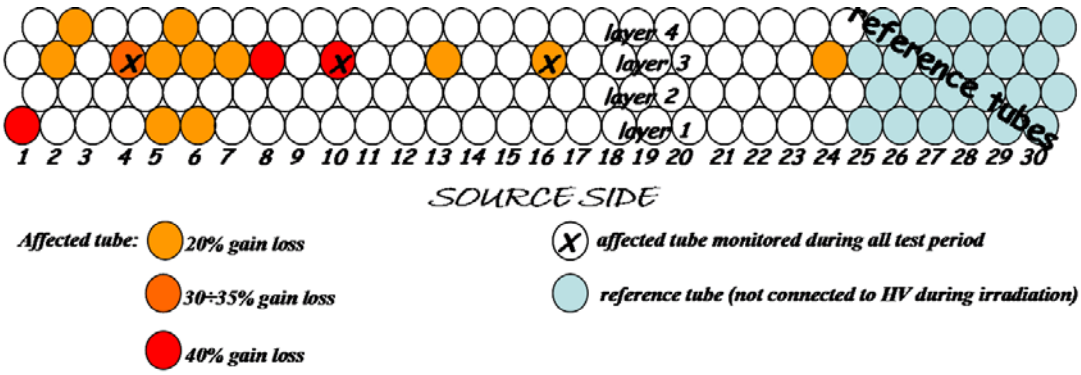

Figure 4.38: *This schema summarize the BIS tube which showed a loss in pulse height. The different colours indicate the different slop of the* Q^{corr}_{60keV} *plotted versus the wire coordinate [See figure* **??** *]. The three tubes signed by a "X" are the three monitored during all the ageing test.*

4.8 Further Analysis

In order to understand the source of the observed gain loss further analyses were made on anode wires and on tubelets (the final gas distribution components) after the irradiation period. In order to confirm or discard the suspicion of Si-contaminant being responsible for the observed ageing effects as in the previous 2003 ageing test, and to find its source, SEM (Scanning Electron Microscopy), EDX (Energy Dispersive X-ray) and FTIR (Fourier-Transform Infrared Spectroscopy) analysis methods have been used.

4.8.1 Wire Analysis

It was decided to analyze three tubes from the third layer, two affected by ageing and one not affected.

The main problem to analyze the wires was to extract them from tubes avoiding the alteration of the possible contamination. To solve this problem an "ad hoc" procedure was put down.

Wire Extraction

In order to avoid the chamber total destruction because the wires to be analyze were placed in the third inner layer, and above all in order to avoid an alteration of the wire pollution, or a contamination of it related to extraction and not to ageing, this safe procedure was set up.

A particular structure guiding a drill was made to extract the wire from a tube in a chamber and a special drill bit, referred as 'cup mill' (Figure 4.39), was used.

The procedure consists in five step:

- The first step consists in digging the end-plug of the gas outlet side up to about 0.5 mm to its bottom; in this way the central part of the end-plug is left attached to the rest.
- The second step consists in digging the end-plug of the gas inlet side up to about 0.5 mm to its bottom leaving the central part on it attached to the rest.
- The third step consists in breaking the thin 0.5 mm layer of the end-plug in the gas outlet side. To do this a brass bar is screwed on the end-plug central part; a chisel is used to remove the thin layer of Noryl while, at the same time, the brass bar was held to avoid the end-plug central part and the wire going into the tube due to the wire stretching.
- The fourth step consists in breaking the end-plug on the other side (it can be done kindly by hand, now the wire is safely held on the other side).
- The fifth step consists in the wire extraction. It must be done carefully trying to keep the wire stretched and without touching the tube wall.

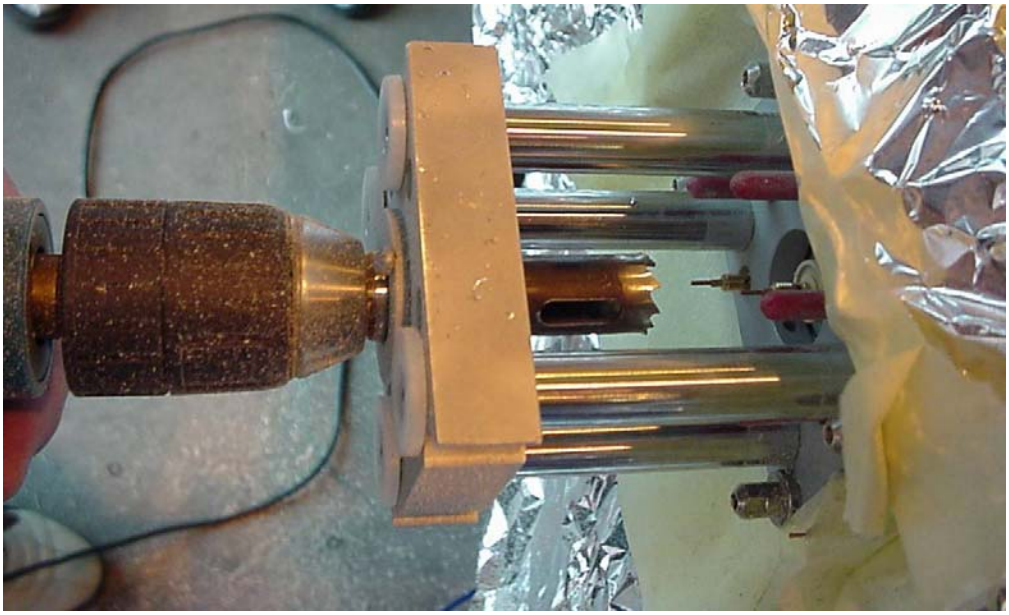

Figure 4.39: *A picture taken during wire extraction. The cup mill and the structure guiding the drill are shown.*

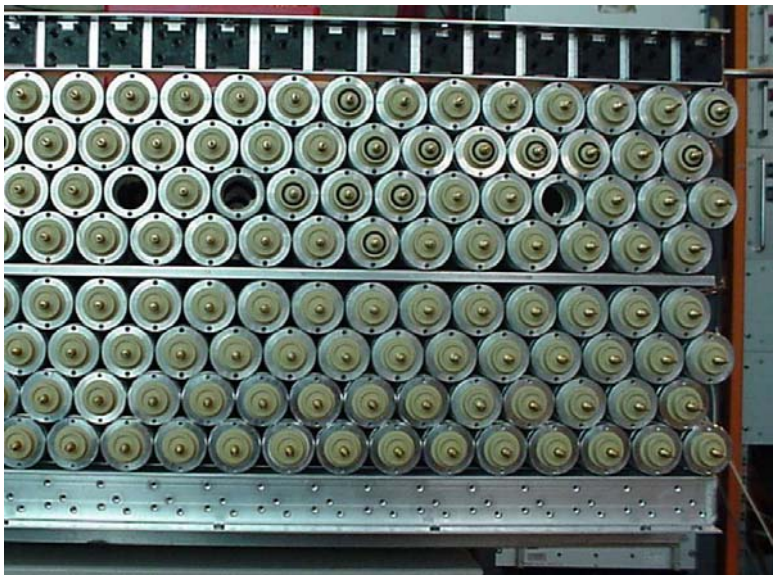

Figure 4.40: *A picture of a BIS side after the extraction of the three wires on the third layer for analyses.*

Results from SEM Analysis

SEM analyses on different samples of ageing affected and non-affected wires were performed at CERN TS Department and at the Chemical Department of Calabria University (Figure 4.41). Both set of analyses gave same results.

Figure 4.41: *A picture of the Scanning Electron Microscope of the Chemical Department of Calabria University. It is a Leo-Leika SEM.*

The analyzed wires belonged to tubes of the third layer, tube 4 and tube 10 affected and tube 12 not affected (Figure 4.40).

Micrographs of the affected wires confirmed the presence of needle-like growth perpendicular to the wire surface in the first centimeters. Figures 4.42, 4.43, 4.44, 4.45 and 4.46-*left* show micrographs of the tube 10 layer 3 wire. The pollution are visible only in the first 10÷15 centimeters of the wire, as expected from pulse height analysis.

Figure 4.43-*right* shows the EDX spectrum acquired at the beginning of tube 10 layer 3 wire. A big Silicon peak and an Oxigen peak are visible confirming the nature of the pollution, the same of the previous ageing test results. Since Silicon are not part of any of the gases making up the operating mixture, the observed ageing effects are clearly due to a contaminant.

Figure 4.46-*right* shows a micrograph taken on the first centimeters of the wire from the not affected tube 12 of layer three. No deposits are visible on it as expected from pulse height analysis.

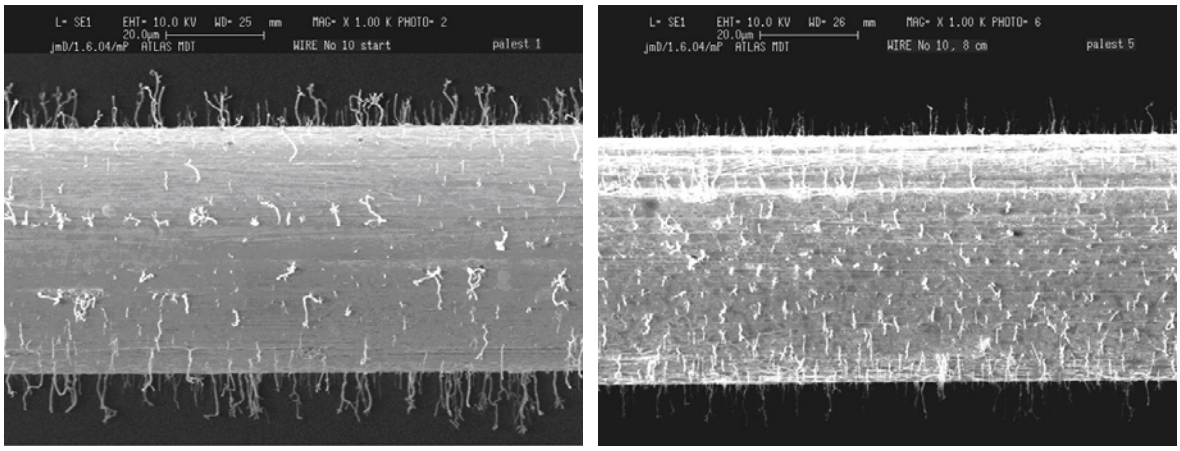

Figure 4.42: Tube 10 layer 3. ***On the left:*** *the beginning of the wire from the gas inlet side, needle-like deposits are clearly visible on the surface.* ***On the right:*** *8 cm from the gas inlet side, thick needle-like deposits on the surface are visible. (CERN)*

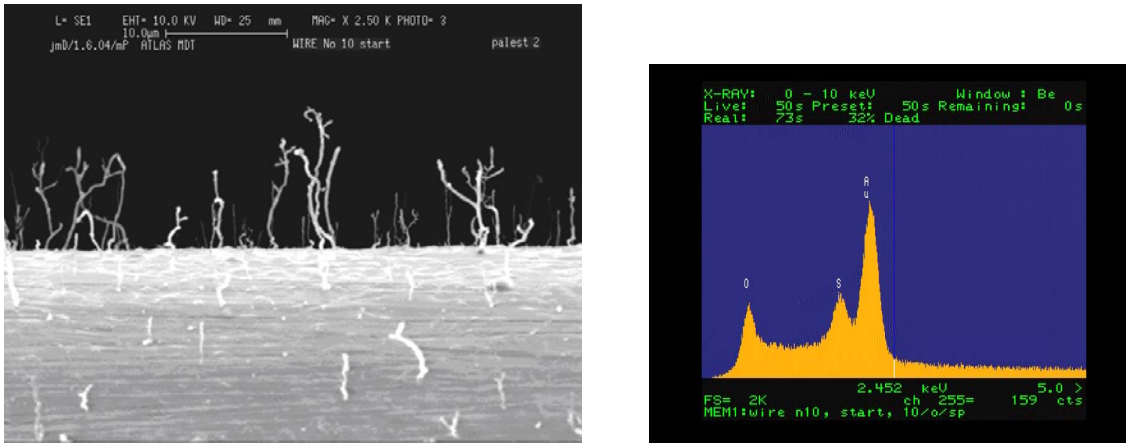

Figure 4.43: Tube 10 layer 3. ***On the left:*** *the beginning of the wire from the gas inlet side, an enlargement of the previous picture on the left, single whiskers some µm long are clearly visible.* ***On the right:*** *the relative EDX analysis. The EDX spectrum shows a big Silicon peak generated by the needle-like deposits. (CERN)*

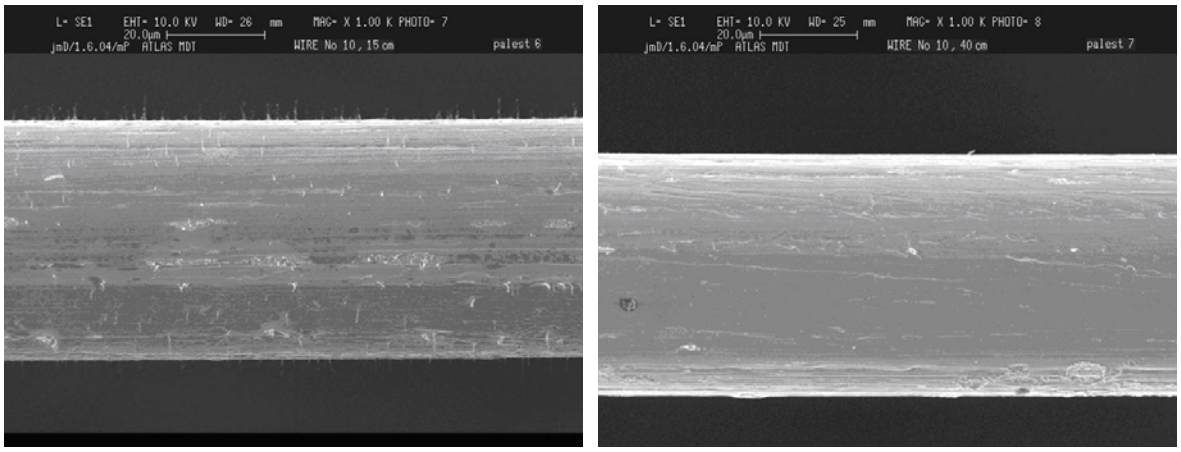

Figure 4.44: Tube 10 layer 3. ***On the left:*** *15 cm from the gas inlet side, a very few needle-like growths are visible on the wire surface.* ***On the right:*** *40 cm from the gas inlet side, no needle-like deposits are visible on the wire surface. (CERN)*

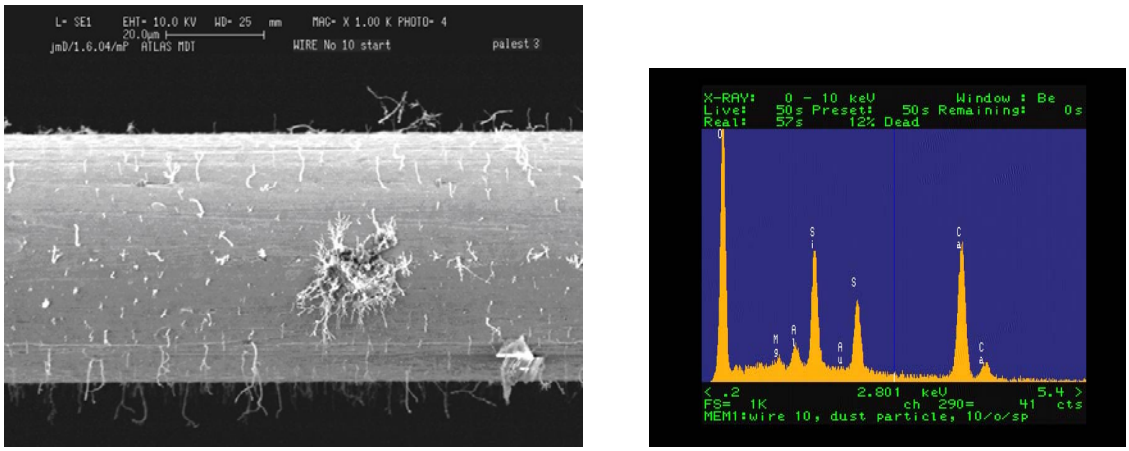

Figure 4.45: Tube 10 layer 3. ***On the left:*** *a micrograph of the tube 10 layer 3 wire showing ageing effect in the first 10 centimeters. It shows a special germination on a probably preliminary dust particle on the surface of the first centimeters of wire.* ***On the right:*** *the relative EDX analysis. The EDX spectrum shows Ca, S and Mg that are typical elements of a dust particle, and a big Si peak generated by the needle-like deposits. (CERN)*

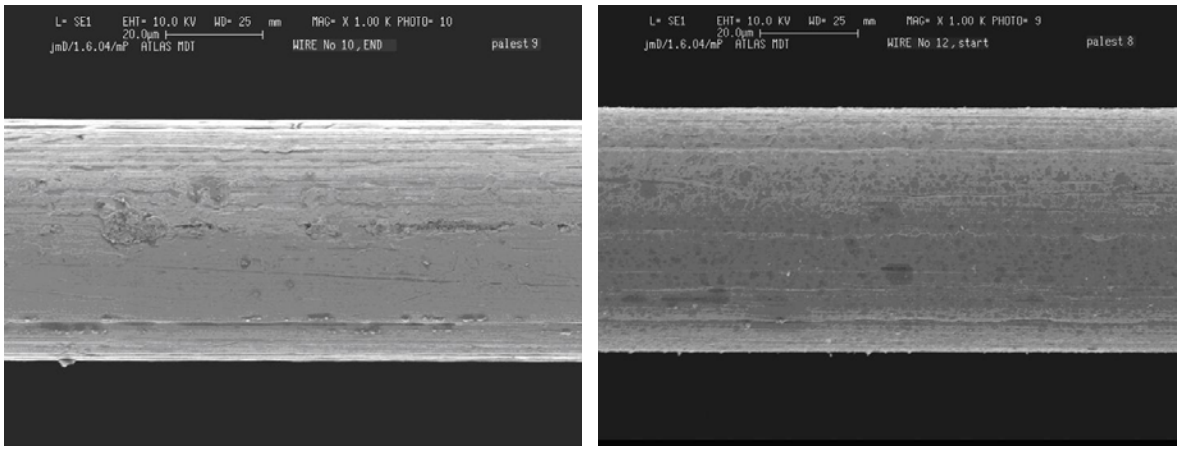

Figure 4.46: ***On the left:*** **Tube 10 layer 3.** 160 *cm from the gas outlet side (end of the wire - gas outlet side), there is no Si-contamination visible on the wire surface.* ***On the right:*** **Tube 12 layer 3.** *This micrograph taken at the beginning of the wire shows no deposit on the wire surface, as expected from the pulse height analysis. (CERN)*

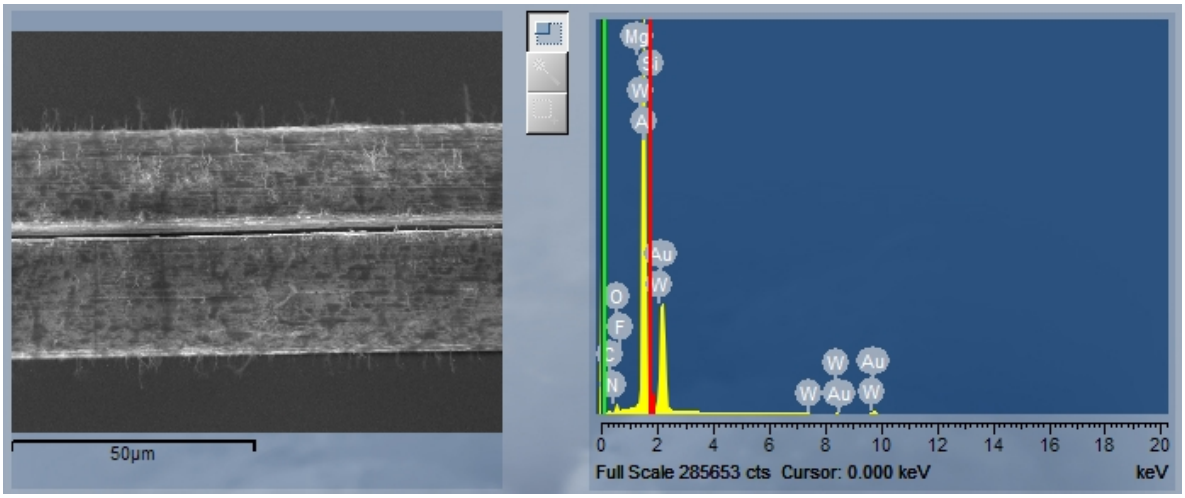

Figure 4.47: *The micrograph (on the left) and the EDX spectrum (on the right) relative to the SEM mapping performed on* **Tube 4 layer 3** *wire shown in figure 4.48. The EDX spectrum shows a big Silicon peak generated by the needle-like deposits; in the spectrum the Si α and β lines are emphasized in red and green respectively. (UNICAL)*

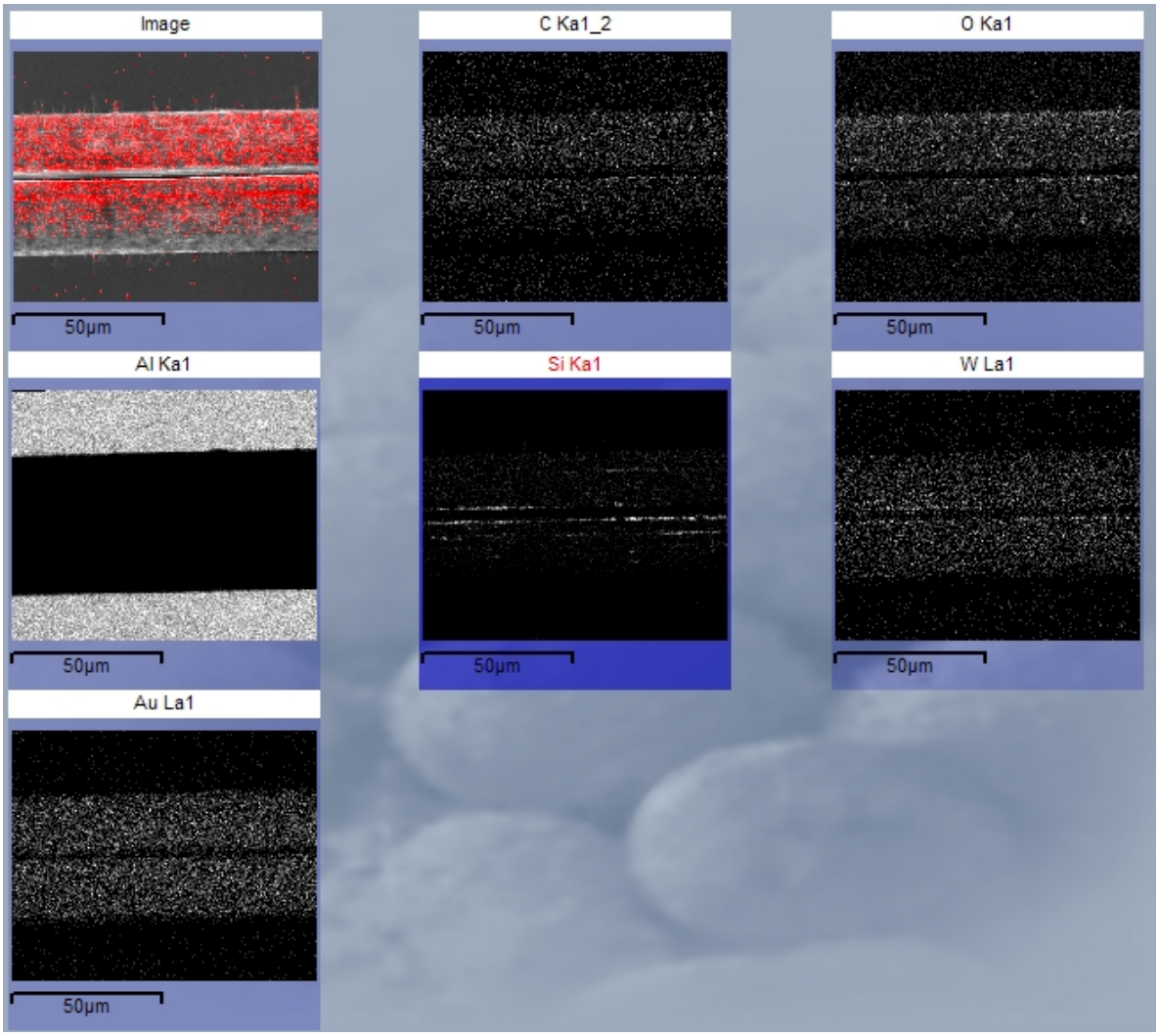

Figure 4.48: *A SEM mapping from* **Tube 4 layer 3.***: it shows a map of the different elements detected on the sample; in red the Si-contamination, which map-micrograph is the picture in the middle, is emphasized. The presence of C and O is due to the SEM analysis itself. (UNICAL)*

Figure 4.47-on the left shows the same micrograph of the wire sample from tube 4 layer 3, on the wire a groove is visible. It is normal and due to the wire production process, in fact it was observed many times on new wire sample analysed as comparison with the aged ones. Figure 4.47-on the right shows the EDX spectrum acquired on the same wire sample. The presence of C and O is due to the SEM analysis itself (background).

Figure 4.48 shows a map of the different elements detected on the wire sample from tube 4 layer3. In the different pictures are shown the maps of the detected elements on the sample. In the first picture the Silicon contamination superimposed to the micrograph of the wire is reported.

4.8.2 Tubelet Analysis

The largest part of tubes affected by ageing was in the BIS third layer, as the figures 4.37 and 4.38 show. Due to the non uniformity of the ageing effects it was decided to analyze the gas components not being common to all tubes. It was decided to analyze the tubelets, little stainless steel tubes which, one for each tube, distribute gas from the gas manifold (Par. 3.1.4, Figure 3.5).

The tubelets set on BIS chamber were previously cleaned in batch. In order to find out if something was wrong in the cleaning procedure of these components, some tubelets from BIS and some tubelets from the same cleaning batch as those ones on BIS layer 3, but tubelets not used before, were analyzed by Fourier-Transform Infrared Spectroscopy (FTIR) technique looking for any type of pollution, but in particular Silicone traces. The FTIR technique has the advantage of being sensitive to certain chemical groups, due to the range of large wavelength that it uses, which excites mainly vibrational degrees of freedom in the molecules studied. FTIR spectroscopy is the most reliable method in identifying silicone compounds. The analyses were performed at CERN TS Department.

The sample of 5 tubelets from BIS chamber was composed by two tubelets from affected tubes, one of layer one and one of layer three, and three tubelets from not affected tubes, one of layer one and two of layer three. Figure 4.53 shows the transmission plot of a affected tube (tube 16) of layer three, while the figure 4.52 shows the transmission plot of a not affected tube (tube 12) of layer three. Figure 4.54 shows the transmission plot of the five tubelets sample not used in the test. Two of the tubelets (one belonged to a tube showing ageing, the other belonged to a tube not showing ageing) show a slightly different IR spectrum. However no clear signal for a Si-contamination (signal from Si is expected in the range $500 \div 1500$ cm^{-1}) could be observed in either case, nor in the set of five tubelets not used before (ruling out the hypothesis of a bad cleaning of the tubelets).

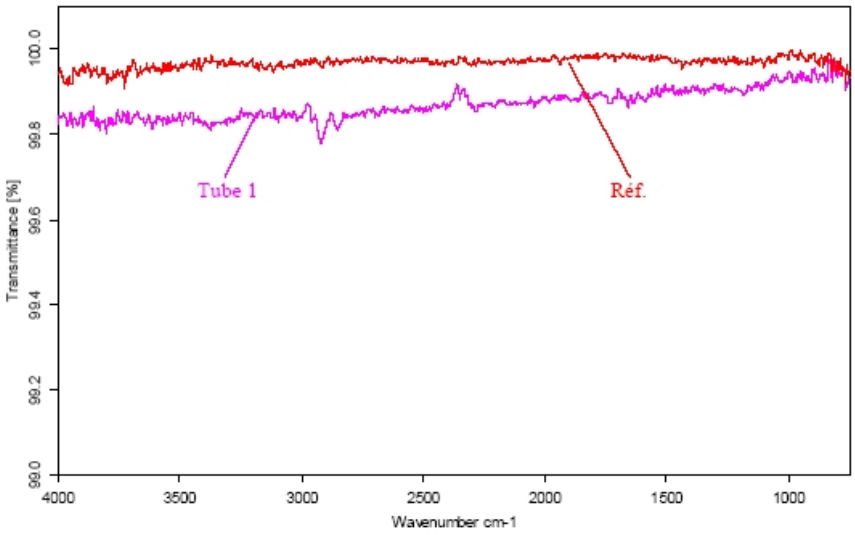

Figure 4.49: *Tubelet from tube 1 layer 3, shown loss in pulse height.*

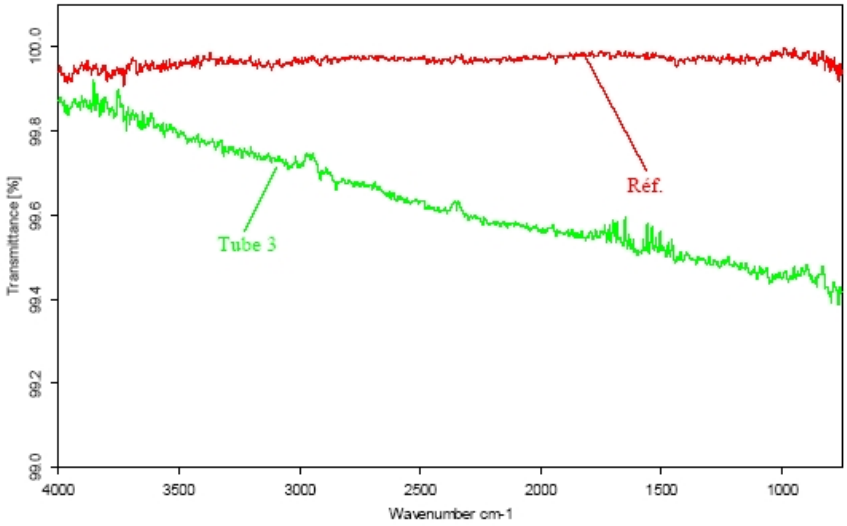

Figure 4.50: *Tubelet from tube 3 layer 3, shown loss in pulse height.*

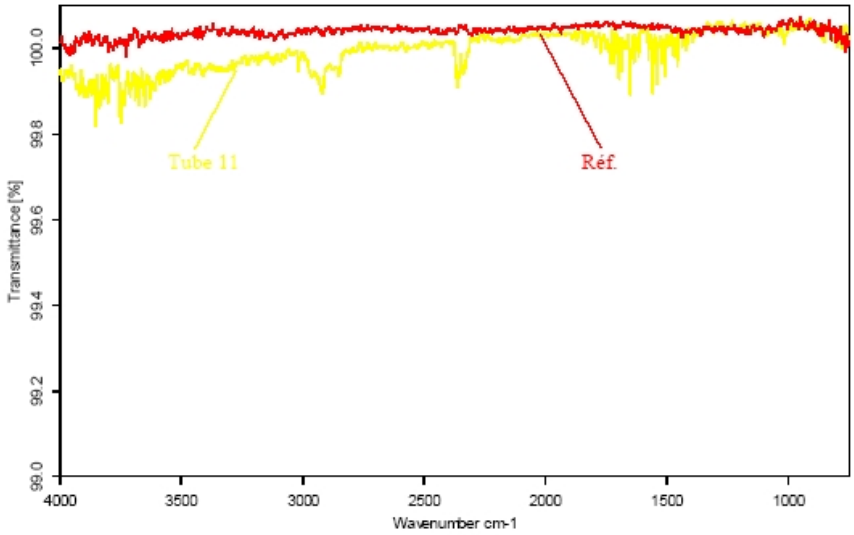

Figure 4.51: *Tubelet from tube 11 layer 3, shown loss in pulse height.*

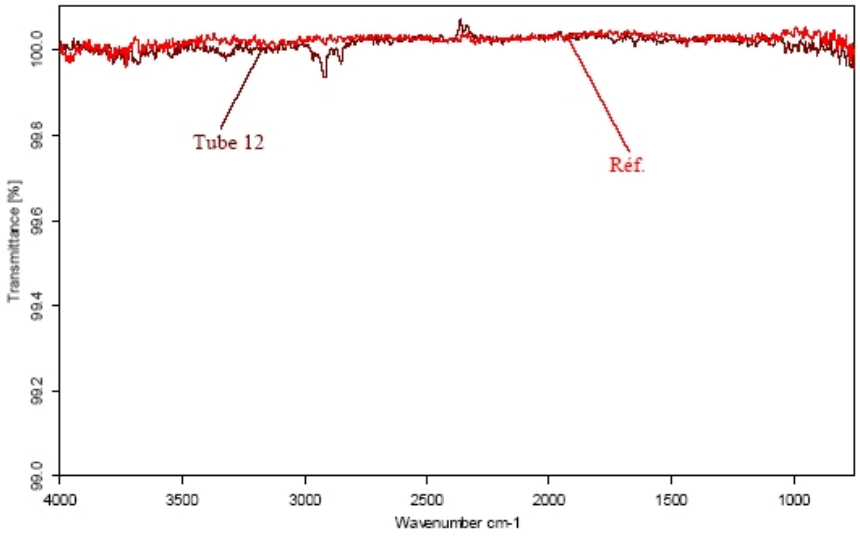

Figure 4.52: *Tubelet from tube 12 layer 3, shown loss in pulse height.*

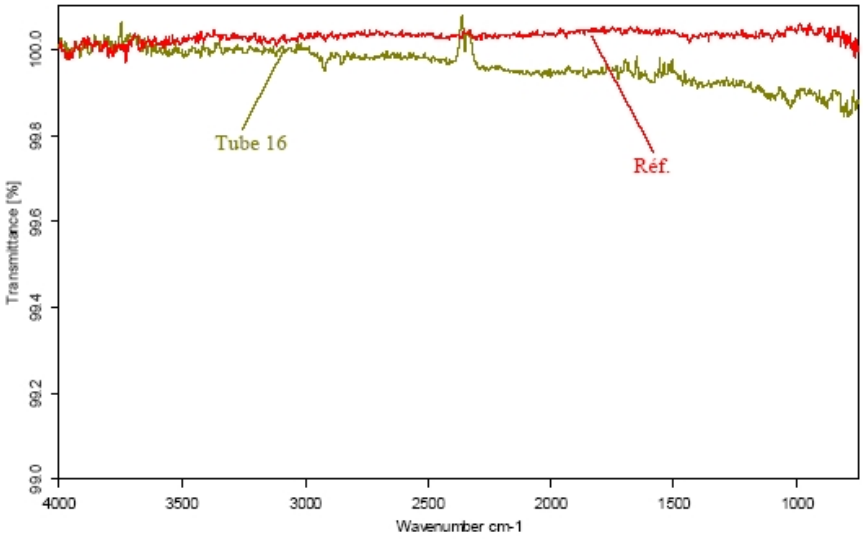

Figure 4.53: *Tubelet from tube 16 layer 3, shown loss in pulse height.*

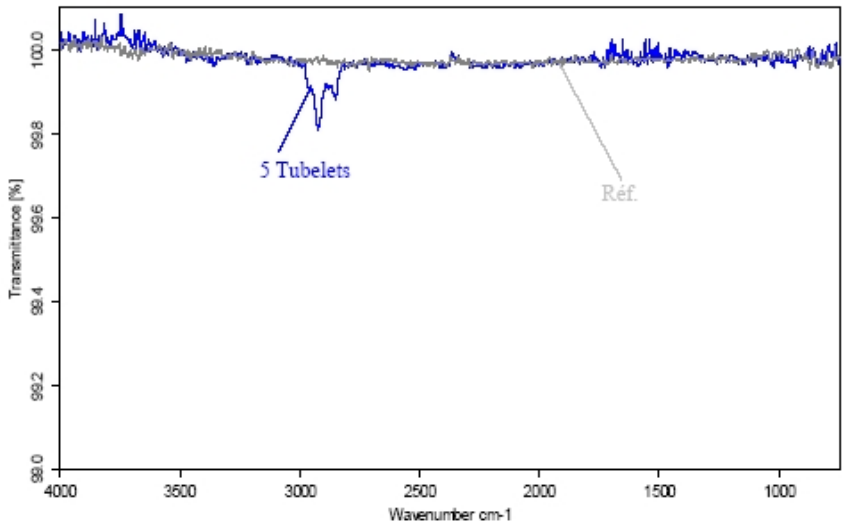

Figure 4.54: *Sample of five tubelets not used, belonging to the same cleaning batch of the used ones.*

4.9 Summary and Conclusions

In this chapter the ageing studies performed on MDT chambers were presented. This ageing study is also reported in detail in [15] and [16].

At first the ageing problem for wire drift chamber were presented. Then the 2001-2003 ageing test was briefly summarized and its major results reported as a starting point for the 2004-2005 ageing test.

The main part of the chapter was dedicated to the 2004-2005 ageing study, which set-up, preliminary tests, analysis and further analysis investigations were reported in detail.

After 100 days of irradiation at CERN GIF, corresponding to 290 mC/cm, equivalent to 5 years of LHC operation (including the safety factors 5 to allow for uncertainties in the estimated background) the following results have been found:

- no tube had a decrease of the signal greater than 5%, apart from the first 10÷12 cm from the gas inlet;
- 82 out of 96 tubes showed no appreciable deterioration of the signal, in the first 10÷12 cm of the tube;
- the remaining 14 tubes showed a decrease of the pulse height between 5% and 30%; the drop was not linear with the accumulated charge, but remained constant after 70 mC/cm without any further decrease of the pulse height;
- the loss in efficiency was negligible, because it affected a small region of wire;
- the chemical analyses of the wires, both with the Scanning Electron Microscope, the Energy Dispersive X-ray and the Fourier Transform InfraRed spectroscopy techniques, were able to identify the effect, but had given no clue for its cause.

To summarize, although the origin of the effect is not completely understood, its size and phenomenology have been successfully measured; they do not look very dangerous for the experiment.

Bibliography

[1] *S. Zimmermann, C. Cernoch*, ***MDT Ageing Studies - Results of the studies conducted at the Gamma Irradiation Facility GIF between autumn 2001 and summer 2003***, ATLAS Note ATL-MUON-2004-019, 2004.

[2] *S. Zimmermann*, ***High Rate and Ageing Studies for the Drift Tubes of the Atlas Muon Spectrometer***, PhD Thesis, Albert-Ludwing Universitat Freiburg, Germany, 2004.

[3] *G. Kaptis et al.*, ***Mechanical design of the BIS module zero MDT chamber***, ATLAS Note ATL-MUON-98-242, 1998.

[4] *ATC a.s.*, ***Argon-Turbo-Circulator, Technical Description and Service Instructions***, Hradec Králové, Czech Republic, 2001.

[5] *L. Malter*, ***Thin Film Field Emission***, Phys. Rev. 50 48-58, 1936.

[6] *M. Dolt et al.*, ***Fast Gases for the ATLAS Monitored Drift Tubes***, ATLAS Note ATL-MUON-94-043, 1994.

[7] *T. Zhao, L. He*, ***A study of gas mixtures for ATLAS MDT***, ATLAS Note ATL-MUON-95-102, 1995.

[8] *ATLAS Collaboration*, ***ATLAS Muon Spectrometer Technical Design Report***, CERN/LHCC 97-22, 1998.

[9] *M Kollefrath et al.*, ***Ageing Studies for the ATLAS Monitored Drift Tubes***, Nucl. Instr. and Meth. A 419, 351-356, 1998.

[10] *M. Capeans*, ***Aging and Materials: Lessons Learned for Detectors and Gas Systems***, Nucl. Instr. and Meth. A 515, 73-88, 2003.

[11] *A. Caldarone, M. Cirilli, A. Di Domenico, A. Di Girolamo, S. Fiore, C. Luci, L. Pontecorvo, D. Salvatore, S. Zimmermann*, ***Study of the serial gas connection effect on MDT chambers***, ATLAS Comunication ATL-COM-MUON-2005-004, 2005.

[12] *C. Cernoch, S. Zimmermann*, ***First experience with the prototype Atlas MDT gas circulation system at GIF***, ATLAS Comunication ATL-COM-MUON-2002-023, 2002.

[13] *J. Oliver C. Posch, E. Hazen*, ***MDT-ASD, CMOS front-end for ATLAS MDT***, CERN/ATL-MUON-2002-003, 2002.

[14] *M. Aleksa, W. Riegler*, ***Non-Linear MDT Drift Gases like Ar/CO_2***, ATLAS Note ATL-MUON-98-268, 1998.

[15] *A. Di Domenico A. Di Girolamo S. Palestini M.Schioppa P. Valente S. Zimmermann C. Adorisio, M. Cirilli*, ***Results from the 2004 Atlas MDT ageing test in X5/GIF (Gamma Irradiation Facility) area***, CERN/ATL-COMM-MUON-2005-, 2005.

[16] *A. Di Girolamo*, ***Studies on the performances of the Monitored Drift Tubes of the Atlas detector***, PhD Thesis, Università degli studi di Siena, Italia, 2004.

Part III

MSSM HIGGSES DECAY STUDIES

Chapter 5

Observability of MSSM Heavy Neutral Higgs Bosons Decaying Into Neutralinos with the ATLAS Detector

In this chapter the possibilities to observe the decay of heavy neutral SUSY Higgs bosons into supersymmetric particles at Atlas detector is discussed. I will focus on the most promising channel where the heavy neutral Higgs bosons decay into a pair of next-to-lightest neutralinos $\tilde{\chi}_2^0$, followed by $\tilde{\chi}_2^0 \to \tilde{l}_L^{\pm}\, l^{\mp}$ and $\tilde{l}_L^{\pm} \to l^{\pm}\, \tilde{\chi}_1^0$. This decay chain leads to a final state signature of four isolated leptons plus E_T^{miss}.

5.1 Introduction

One of the main goals of the Large Hadron Collider project is to find new physics signals. If SUSY is indeed the right new physics at the electroweak scale, the first task of the LHC will be to detect a deviation from Standard Model predictions characteristic of SUSY. The ability to do so is clearly model dependent. For example if all SUSY particles were nearly degenerate in mass, then they would decay into very soft jets or leptons plus an invisible χ_1^0, and nothing would be observable. Fortunately such a degenerate spectrum does not occur in any reasonable model [1].

While the problem of the electroweak symmetry breaking can be solved in the Standard Model by the Higgs mechanism, introducing one Higgs boson, the Minimal Supersymmetric Standard Model requires five physical Higgs bosons: a light CP-even (h^0), a heavy CP-even (H^0), a heavy CP-odd (A^0) and two charged Higgs particles ($H^{\pm}$), as we have seen in the first chapter. Therefore the discovery of heavy neutral Higgs bosons would be a major breakthrough in verifying the supersymmetric nature of the fundamental theory.

At the tree level all Higgs masses and couplings can be expressed in terms of only two

parameter, $\tan\beta$ and m_A. After introducing effect from radiative corrections, the mass of the lightest Higgs boson h^0 is predicted to be smaller than $m_{h^0} < 130$ - $150\ GeV$, while the H^0, A^0 and $H^\pm$ bosons masses are heavier, almost degenerate and no upper limit is given by the model.

The most promising channel to discover the heavy SUSY Higgs bosons is the $A/H \to \tau\tau$ channel, [2], [3] and [4], where both the leptonic and hadronic decays of the τ can be exploited. This channel has been shown to cover large parts of the intermediate and high $\tan\beta$ region of the MSSM parameter space. For low values of $\tan\beta$ the coupling of the Higgs bosons to taus is not high enough and therefore this region is not accessible for the $\tau\tau$ channel.
Higgs bosons decaying into sparticles might open new possibilities to explore regions of parameter space where SM decays would not be accessible.

In this Ph.D. theses work I report on a study of this type of decay with the ATLAS detector. I will focus on the decay of the heavy neutral Higgs H^0 and A^0 bosons into two next-to-lightest neutralinos, with each of the neutralinos in turn decaying into two isolated leptons plus E_T^{miss}, such as $\tilde{\chi}_2^0 \to l^+l^-\tilde{\chi}_1^0$, resulting in a clear four isolated leptons final state signature, so the bosons cascade decay is:

$$A/H \to \tilde{\chi}_2^0\tilde{\chi}_2^0 \to 4l^\pm + X \qquad (l = e, \mu).$$

The search for $A/H \to \tilde{\chi}_2^0\tilde{\chi}_2^0$ was already proposed some years ago in a theoretical paper [5] and a subsequent study reported the prospectives for observability of this channel with the ATLAS detector in [6] and [7] at the so-called LHC Point 3 (mSUGRA scenario) [2].

5.2 Framework

This study was performed in the framework of the Minimal Supersymmetric Standard Model (MSSM), considering the actual LEP-II limits and the latest constraints on dark matter from the WMAP experiment [8].

Assuming that all the squark masses are equal and the masses of all the slepton generations are also equal, the event samples were generated taking these 12 parameters, instead of the 18 of the MSSM, as free: the mass of the CP-odd Higgs m_A, the Higgsino mass parameter μ, the bino and the wino mass parameter M_1 and M_2, the slepton masses $m_{\tilde{l}_L}$ and $m_{\tilde{l}_R}$, the gluino mass $m_{\tilde{g}}$, the squark mass $m_{\tilde{q}}$, the Higgs VEV ratio $\tan\beta$ and the top, bottom and τ trilinear coupling parameters A_t, A_b and A_τ. The top quark mass is assumed at the default value of $175\ GeV$. In table 5.1 the chosen values are reported.

The high negative value of the trilinear coupling parameter A_t was chosen to have a great mixing in the stop sector and a light Higgs mass m_h compatible with the LEP limits.

The following framework was adopted as a starting point for this study:

- Neutralinos and charginos are considered light and above the LEP-II limits. In fact M_1 was fixed to $75\ GeV$ and, using the renormalization group relation $M_2 \approx 2M_1$, M_2 was set to $150\ GeV$. So, it was taken: $M_1 < M_2 < |\mu|$. This large μ scenario is favoured

Parameter	Chosen Value	Parameter	Chosen Value
m_A	350 GeV	μ	500 GeV
M_1	75 GeV	M_2	150 GeV
$m_{\tilde{l}_L}$	200 GeV	$m_{\tilde{l}_R}$	120 GeV
$m_{\tilde{g}}$	1050 GeV	$m_{\tilde{q}}$	1000 GeV
$\tan\beta$	6	A_t	-1000
A_b	0	A_τ	0

Table 5.1: *The chosen values of some MSSM free parameters (Input values for the event samples generations).*

in models where $\tilde{\chi}_1^0$ is the dark matter candidate, like mSUGRA. In low μ scenarios, the decay of $\tilde{\chi}_2^0$ into leptons will be strongly suppressed. For large values of μ, $\tilde{\chi}_2^0$ is rather wino and $\tilde{\chi}_1^0$ is bino-like. Therefore it approximately holds that $m_{\tilde{\chi}_1^0} \approx M_1$ and $m_{\tilde{\chi}_2^0} \approx M_2$.

- Sleptons were taken to be also light. It was considered the case they would be lighter than $\tilde{\chi}_2^0$, thereby allowing two-body decays into lepton; $m_{\tilde{l}} < m_{\tilde{\chi}_2^0}$, meaning that real decays of neutralinos into sleptons are allowed:

$$\begin{aligned} \tilde{\chi}_2^0 &\rightarrow \tilde{l}^{\pm} l^{\mp} \quad \text{and} \\ \tilde{l}^{\pm} &\rightarrow l^{\pm} \tilde{\chi}_1^0. \end{aligned}$$

- The masses of squarks and gluinos are kept at the 1 TeV scale. In the MSSM it is natural that these sparticles are heavier than neutralinos and sleptons.

While this chosen point in the MSSM parameter space may not be the one that nature has chosen, it is necessary to emphasize that consistent sets of analyses can only be performed in the context of a consistent model. This is because many promising signals that might be clearly distinguished from Standard Model backgrounds in one channel, can be obscured by production and decays of other supersymmetric particles. It is not necessary to believe in this model, but the model that Nature has chosen will be self-consistent [9].

5.2.1 MSSM Mass Spectrum

For the point in the MSSM parameter space chosen, the SUSY particles are rather light, with masses ranging from $\tilde{\chi}_1^0$ ~73 GeV for the LSP, to $\tilde{\chi}_1^{\pm}$ ~142 GeV for the lightest chargino, to ~1 TeV for the first family of squarks and gluino. The lightest Higgs boson, m_h ~113 GeV, the heavy ones have masses of m_{A^0/H^0} ~350 GeV. The detailed spectrum of SUSY particles masses is reported in table 5.2.

In table 5.3 the branching ratios for h^0, H^0 and A^0 bosons are reported as given by HERWIG generator program (Par. 5.3).

Sparticle	Mass (GeV)	Sparticle	Mass (GeV)
$m_{\tilde{g}}$	1050.00	$m_{\tilde{q}}$	~1000
$m_{\tilde{l}_L}$	205.20	$m_{\tilde{l}_R}$	127.37
$\tilde{\chi}_1^0$	72.98	$\tilde{\chi}_2^0$	141.85
$\tilde{\chi}_3^0$	504.47	$\tilde{\chi}_4^0$	514.64
$\tilde{\chi}_1^\pm$	141.75	$\tilde{\chi}_2^\pm$	515.03
m_h^0	113.03	m_H^0	351.33
m_A^0	350.11	$m_H^\pm$	358.49

Table 5.2: *The expected mass spectrum for SUSY particles and Higgs bosons at the chosen point in the MSSM parameters space.*

Decay Mode	Branching Ratio	Decay Mode	Branching Ratio
$h^0 \to b\bar{b}$	85.8%	$h^0 \to gg$	4.8%
$h^0 \to \tau^+\tau^-$	7.3%	$h^0 \to c\bar{c}$	1.8%
$A^0 \to \tilde{\chi}_2^0\tilde{\chi}_2^0$	9.2%	$H^0 \to \tilde{\chi}_2^0\tilde{\chi}_2^0$	3.1%
$A^0 \to b\bar{b}$	45.5%	$H^0 \to b\bar{b}$	60.8%
$A^0 \to \tilde{\chi}_1^+\tilde{\chi}_1^-$	21.4%	$H^0 \to h^0h^0$	10.2%
$A^0 \to \tilde{\chi}_1^0\tilde{\chi}_2^0$	8.2%	$H^0 \to \tilde{\chi}_1^+\tilde{\chi}_1^-$	7.4%
$A^0 \to t\bar{t}$	7.6%	$H^0 \to \tau^+\tau^-$	6.5%
$A^0 \to \tau^+\tau^-$	4.8%	$H^0 \to \tilde{\chi}_1^0\tilde{\chi}_2^0$	5.5%
$A^0 \to \tilde{\chi}_1^0\tilde{\chi}_1^0$	1.8%	$H^0 \to W^+W^-$	2.1%
$A^0 \to Z^0/\gamma^* h^0$	1.1%	$H^0 \to \tilde{\chi}_1^0\tilde{\chi}_1^0$	1.6%

Table 5.3: *The expected branching ratios for Higgs bosons at the chosen point in the MSSM parameters space.*

5.3 Event Samples Generation

The signal events were generated with HERWIG [10], [11]. A^0 and H^0 were produced via gluon interaction (Figure 5.1):

$$gg \rightarrow A^0, H^0.$$

The associated production $gg \rightarrow b\bar{b}A^0, H^0$, WW/ZZ and Higgsstrahlung processes were not included.

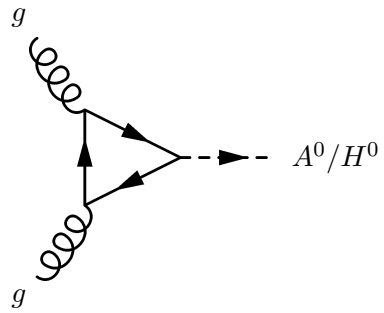

Figure 5.1: *Feynman diagram of the heavy neutral Higgs bosons production via gluon fusion.*

Then the Higgs bosons were forced to decay in two next-to-lightest neutralinos (Figure 5.2):

$$A^0/H^0 \rightarrow \tilde{\chi}_2^0\tilde{\chi}_2^0.$$

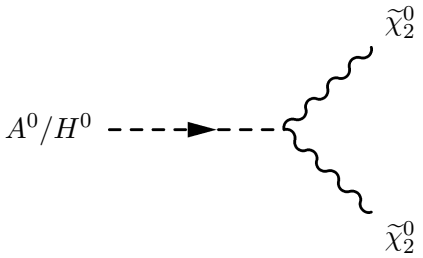

Figure 5.2: *Feynman diagram of the heavy neutral Higgs bosons decay into two next-to-lightest neutralinos.*

Each neutralino was forced to decay in $\tilde{l}_R^{\pm}l^{\mp}$, with $l = e, \mu$ only; while slepton decay into lepton-LSP, $l\tilde{\chi}_1^0$, has a branching ratio of 1. Figure 5.3 shows the Feynman diagram of the next-to-lightest neutralino decay chain.

The SUSY background events were also generated with HERWIG. The SUSY spectrum was calculated with ISAJET [12]. The ISAJET program iteratively solves the actual Renormalization Group Equation (RGE) for SUSY masses and couplings; next the output parameters of a general MSSM model were used to calculate the physical masses, which are a mixing of the eigenstates, and the branching fractions. Then it was interfaced to HERWIG using the ISAWIG package [13].

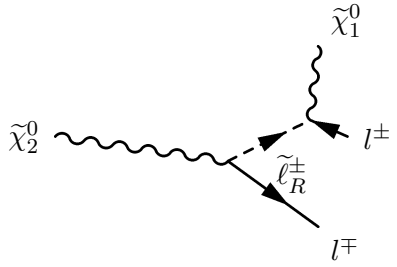

Figure 5.3: *Feynman diagram of the next-to-lightest neutralino $\tilde{\chi}_2^0$ decay chain.*

The HERWIG `IPROC` code used was 3000 (2 partons to 2 sparticles), that includes the following processes:

- (`IPROC=3010`) 2 partons to 2 spartons,
- (`IPROC=3020`) 2 partons to 2 gauginos,
- (`IPROC=3030`) 2 partons to 2 sleptons.

The cross sections of the supersymmetric processes, as given by the generator, are reported in table 5.4.

IPROC	Process	Cross Section (pb)
3620	$gg \to H^0$	0.913
3630	$gg \to A^0$	0.835
3010	2-*parton* $\to$ 2-*sparton*	1.396
3020	2-*parton* $\to$ 2-*gaugino*	6.696
3030	2-*parton* $\to$ 2-*slepton*	0.461
3000	2-*parton* $\to$ 2-*sparticle*	8.558

Table 5.4: *SUSY process cross sections as given by HERWIG.*

The Standard Model background process were generated with PYTHIA [14]. The following SM backgrounds giving rise to four leptons in the final state have been generated: ZZ, $Zb\bar{b}$ and $t\bar{t}$. The decays of Z into taus have not been included.

The ATLAS detector response was simulated using the ATLFAST Monte Carlo [15], which contains a parametrized description of the detector response. The effects of event pile-up at the LHC had not been included.

All the productions were performed in the official ATLAS offline software framework ATHENA [16] (ver. 10.0.1).

5.4 Signal Versus Background Discrimination

Two categories of background have to considered: Standard Model processes and SUSY background.

The analysis strategy is based on the following selection criteria:

- the requirements of events with two pairs of leptons with opposite sign and same flavour (OS-SF), with transverse momentum p_T greater than 10 GeV and within $|\eta| < 2.7$;
- the applying of kinematical cuts to reduce SM ZZ background and SUSY background;
- the applying of isolation criteria to reduce SM $t\bar{t}$ background.

In the following paragraphs this strategy is illustrated.

As the first step four-lepton events were selected at the generator/ATLFAST processing step using the `MultiLeptonFilter` in ATHENA. This filter selects events with four leptons in the final state with $|\eta| < 2.7$ and $p_T > 4$ GeV.

The first kinematical cut used was a requirement on the transverse momenta of the four leptons to have a good reconstruction; so it was required events with $p_T > 10$ GeV for each lepton and with almost two leptons with $p_T > 20$ GeV, taking into account the ATLAS trigger requirements (Par. 2.4.6).

5.4.1 Higgs Signal

There are several SUSY decay modes of the neutral heavy Higgs bosons into neutralinos which lead through the cascade decay to the multileptonic final state but, as shown in table 5.3, at the chosen point in the MSSM parameter space the only decay into neutralinos which leads to a four-leptons signature is:

$$A^0/H^0 \rightarrow \tilde{\chi}_2^0\tilde{\chi}_2^0,$$

with each neutralino decaying as:

$$\tilde{\chi}_2^0 \rightarrow \tilde{l}_R^{\pm} l^{\mp},$$

and each slepton decaying as:

$$\tilde{l}_R^{\pm} \rightarrow l^{\pm}\tilde{\chi}_1^0,$$

This decay chain gives a clear four-leptons signature plus E_T^{miss} due to the two LSP $\tilde{\chi}_1^0$. The A^0 and H^0 decay cannot be distinguished experimentally from each other, since the two heavy Higgs bosons are almost degenerate in mass in the relevant region of parameter space.

Table 5.5 shows the expected $\sigma \times BR$ (values by HERWIG generator program) and table 5.6 shows the expected number of events in three years at high luminosity at LHC ($\mathcal{L}$=300 $fb^{-}1$).

The problem in event selection consists in combining the four leptons into two pair, one for each neutralino. The two-body decay chain of the next-to-lightest neutralino:

$$\tilde{\chi}_2^0 \rightarrow \tilde{l}_R^{\pm} l^{\mp} \rightarrow l^{\pm} l^{\mp} \chi_1^0,$$

produces opposite-sign, same-flavour dileptons which have an m_{ll} invariant mass distribution with an edge at the kinematical limit:

$$m_{ll}^{max} = m_{\tilde{\chi}_2^0} \sqrt{1 - \frac{m_{\tilde{l}_R}^2}{m_{\tilde{\chi}_2^0}^2}} \sqrt{1 - \frac{m_{\tilde{\chi}_1^0}^2}{m_{\tilde{l}_R}^2}} \approx 51.15 \ GeV \tag{5.1}$$

Decay	$\sigma \times BR$ (pb)
$A^0 \to \tilde{\chi}_2^0\tilde{\chi}_2^0$	0.077
$H^0 \to \tilde{\chi}_2^0\tilde{\chi}_2^0$	0.028
$(A^0 + H^0) \to \tilde{\chi}_2^0\tilde{\chi}_2^0$	0.105
$(A^0 + H^0) \to \tilde{\chi}_2^0\tilde{\chi}_2^0 \to 4l\tilde{\chi}_1^0\tilde{\chi}_1^0$	0.044

Table 5.5: *The expected A^0 and H^0 Higgs bosons rates ($\sigma \times BR$) in two next-to-lightest neutralinos and in the four-leptons channel.*

Figures 5.4 and 5.6 show the dilepton invariant mass distribution for signal events with an

Decay	Expected events
$A^0 \to \tilde{\chi}_2^0\tilde{\chi}_2^0$	23100
$H^0 \to \tilde{\chi}_2^0\tilde{\chi}_2^0$	8400
$(A^0 + H^0) \to \tilde{\chi}_2^0\tilde{\chi}_2^0$	31500
$(A^0 + H^0) \to \tilde{\chi}_2^0\tilde{\chi}_2^0 \to 4l\tilde{\chi}_1^0\tilde{\chi}_1^0$	13200

Table 5.6: *The expected number of events with four leptons from A^0 and H^0 Higgs bosons for an integrated luminosity of 300 fb^-1.*

electron pair and a muon pair, $e^+e^-\mu^+\mu^-$. Selecting events where one neutralino decay into electrons and the other one into muons avoids improper combinations of leptons. Figures 5.5 and 5.7 show the dilepton invariant mass distribution for signal events with two pairs of opposite sign leptons of the same flavour, $l^+l^-l^+l^-$. The shape of the dilepton invariant mass spectrum can be used for signal versus background discrimination. The m_{ll}^{max} edge is very clean in the first case (Figure 5.4), the case of two electrons and two muons, but it is not so much clean in the case of four same-flavour leptons due to the mis-combinations that give rise to a "*combinatorial background*".

The first kinematical cut was set at the edge value, $m_{l+l^-} < 55\ GeV$; this cut reduces the "combinatorial background" introduced by the mis-combinations of leptons.

Usually only events with OS-SF lepton pairs $e^+e^-\mu^+\mu^-$ are taken into account for the analysis; in this study it was decided to take into account also the events with four same-flavour leptons, because the combinatorial background introduced by these events is low enough as it will be see in the Higgs mass reconstruction step (Par. 5.6). Figure 5.8 shows the dilepton mass distribution for $e^+\mu^-\mu^+e^-$ signal events superimposed to the $l^+l^-l^+l^-$ dilepton mass distribution. Figure 5.9 shows the dilepton mass distribution for the $l^+l^-l^+l^-$ signal events subtracted of the "combinatorial background", which was estimated using $e^+\mu^-\mu^+e^-$ events distribution.

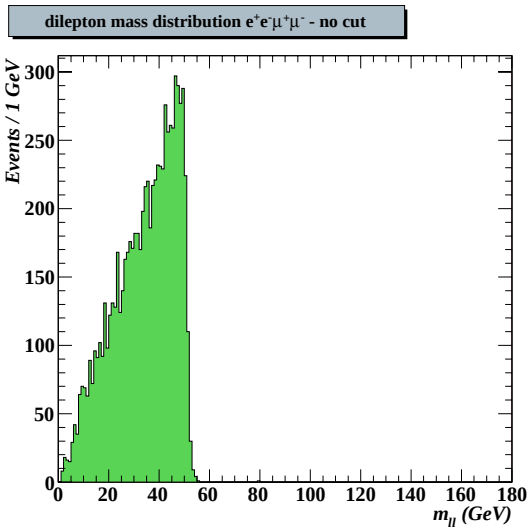

Figure 5.4: *Kinematical edge in the dilepton invariant mass distribution for four-leptons events with a muon pair and an electron pair OS-SF.*

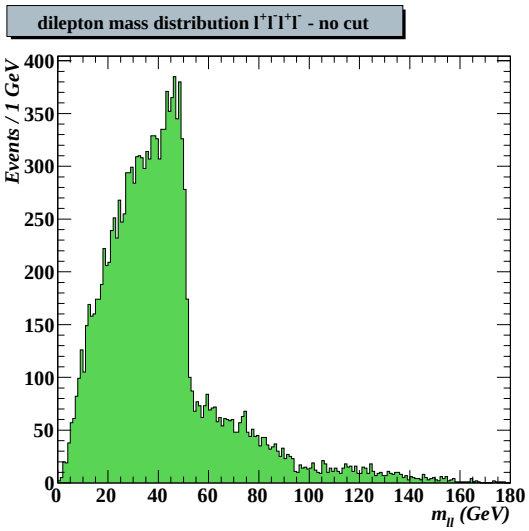

Figure 5.5: *Kinematical edge in the dilepton invariant mass distribution for four same flavour leptons events with two pairs OS.*

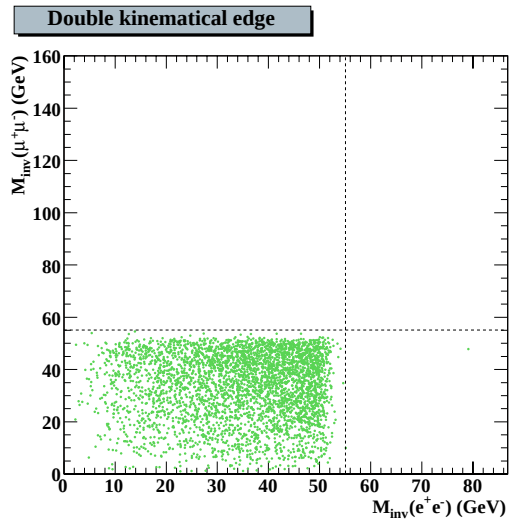

Figure 5.6: *Double kinematical edge in the di-muon versus di-electron invariant mass.*

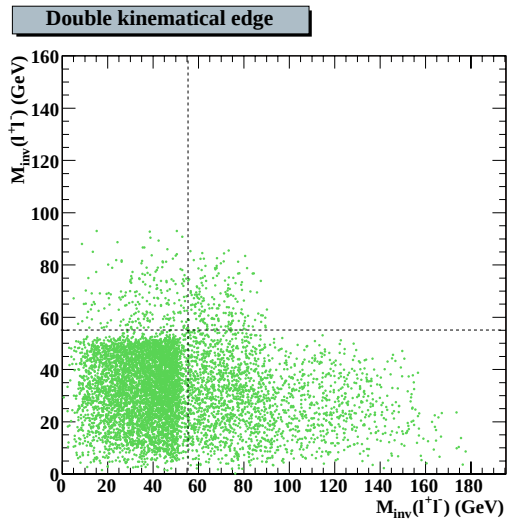

Figure 5.7: *Double kinematical edge in the di-muon versus di-electron invariant mass.*

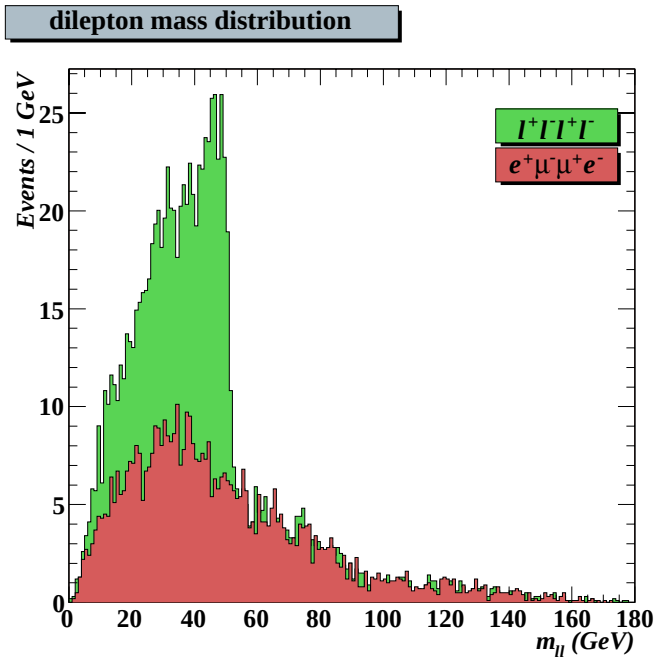

Figure 5.8: *Dilepton invariant mass distribution for $e^+\mu^-\mu^+e^-$ signal events superimposed to dilepton mass distribution for $l^+l^-l^+l^-$ events.*

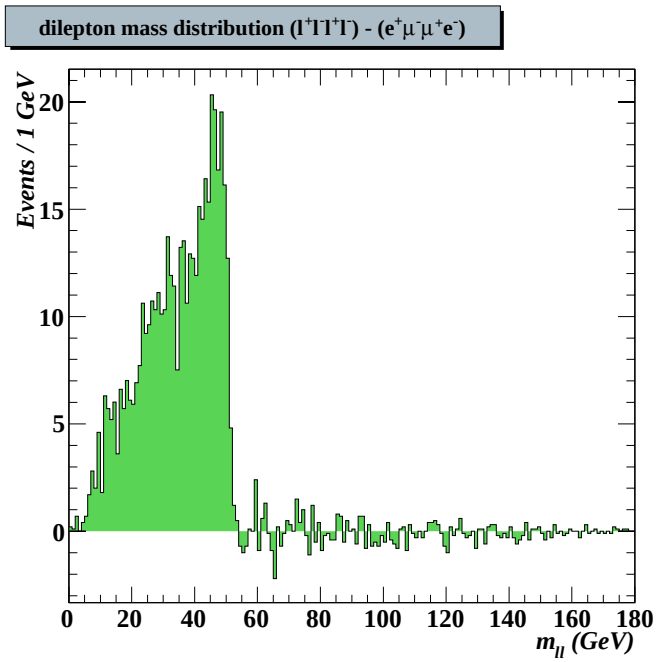

Figure 5.9: *Dilepton invariant mass distribution for $l^+l^-l^+l^-$ events subtracted of the "combinatorial background".*

This kinematical cut reduces the combinatorial background introduced by selecting same flavour four leptons events and it also cuts down the SM ZZ and $Zb\bar{b}$ backgrounds because the kinematical edge is lower than the Z-mass ($55\ GeV = m_{ll}^{max} < m_Z$). Therefore this cut eliminates also any other background containing a Z boson.

As it is said before, the final state signature is four isolated leptons plus E_T^{miss}. The p_T^{miss} distribution of signal, SUSY and SM backgrounds are shown in figures 5.10 - 5.14. In view of these distributions a second kinematical cut was applied selecting events with $p_T^{miss} > 20\ GeV$. This cut essentially reduce further the SM ZZ and $Zb\bar{b}$ backgrounds.

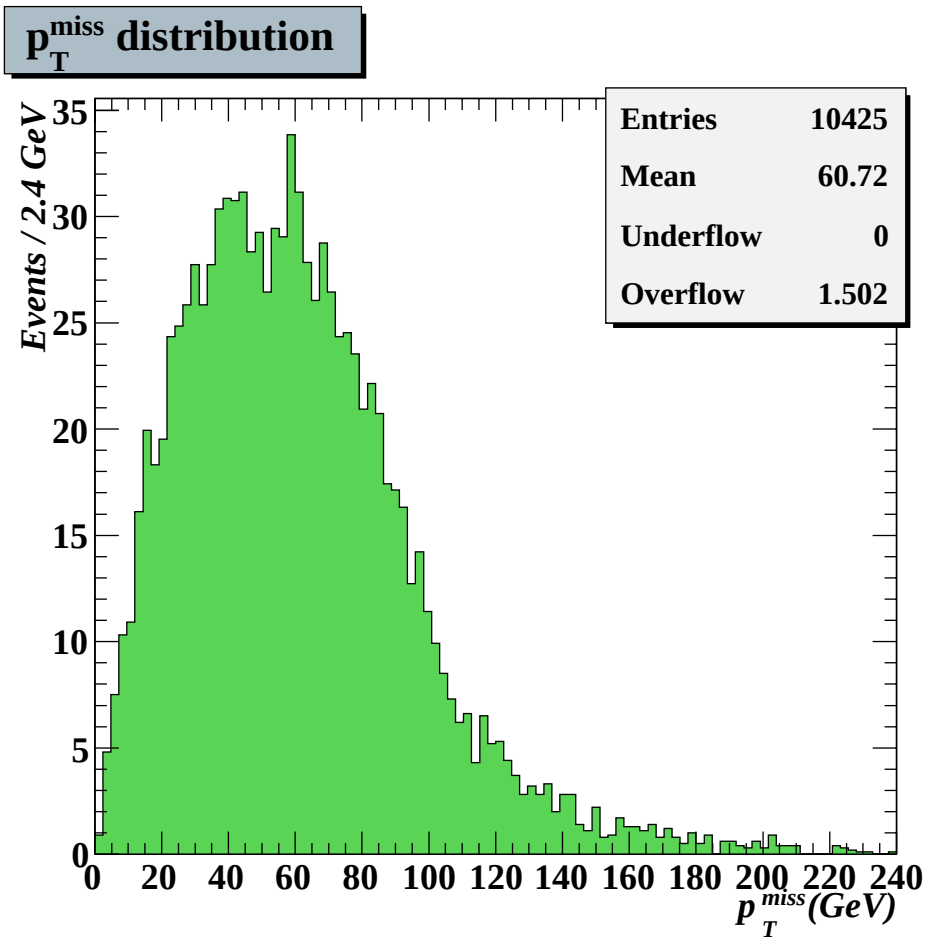

Figure 5.10: *p_T^{miss} distribution for signal events normalized to 30 fb^{-1}.*

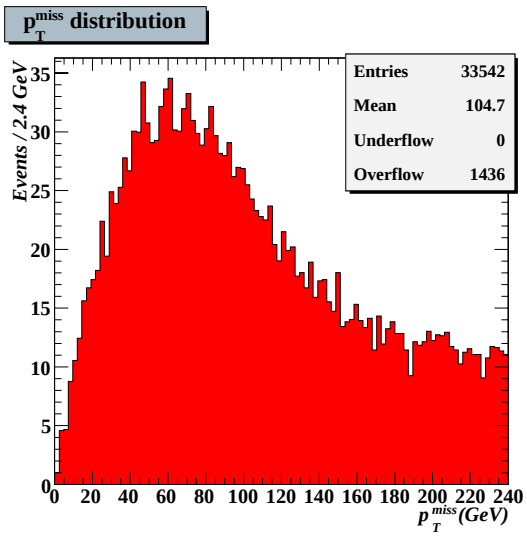

Figure 5.11: *p_T^{miss} distribution for SUSY background events normalized to 30 fb^{-1}.*

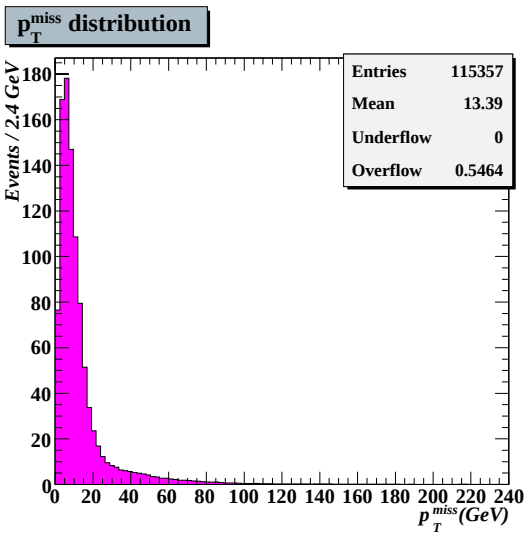

Figure 5.12: *p_T^{miss} distribution for SM ZZ background events normalized to 30 fb^{-1}.*

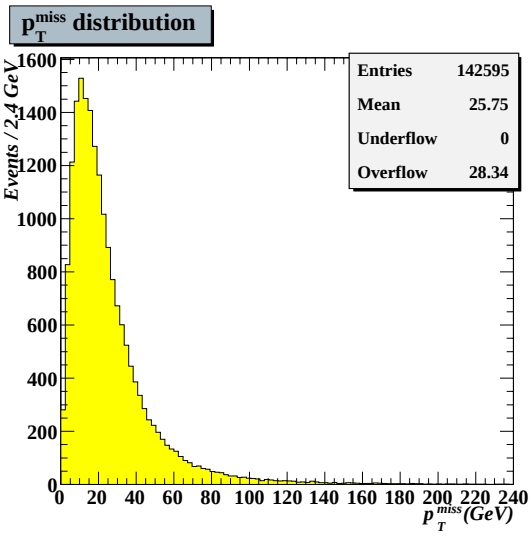

Figure 5.13: *p_T^{miss} distribution for SM $Zb\bar{b}$ background events normalized to 30 fb^{-1}.*

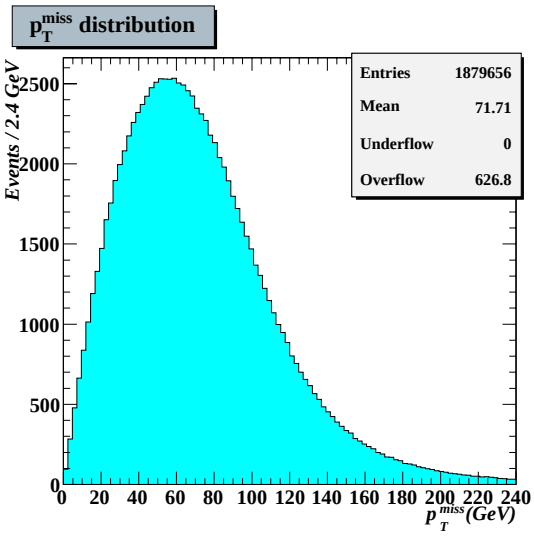

Figure 5.14: *p_T^{miss} distribution for SM $t\bar{t}$ background events normalized to 30 fb^{-1}.*

5.4.2 SUSY Background

The dominant processes for SUSY production at LHC are $\tilde{q}\tilde{g}$ and $\tilde{g}\tilde{g}$ events with charginos and neutralinos being abundantly produced in the cascade decay. The abundant production of leptons in the decay of gauginos lead to characteristic final states with uncorrelated (flavour and sign) multi-leptons, jets and missing energy.

Squark/gluino production is characterized by a large jet multiplicity with ~ 4 jets on average, a significant p_T^{miss} and jet transverse momenta that are larger compared to the expectations for the signal.

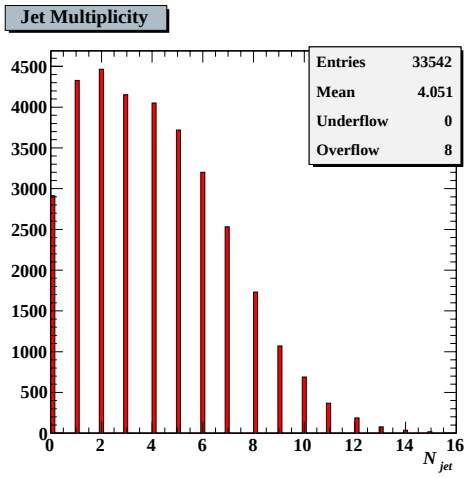

Figure 5.15: *The jet multiplicity (number of jet per event) for SUSY background.*

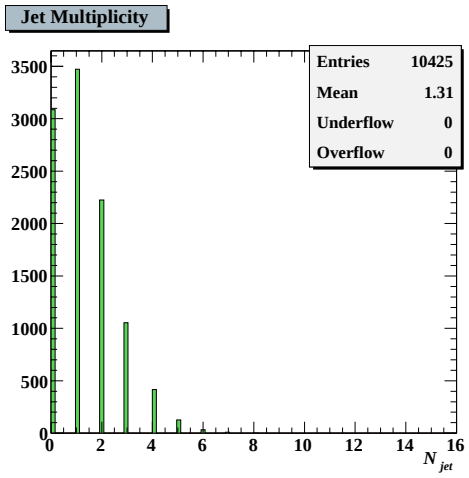

Figure 5.16: *The jet multiplicity (number of jet per event) for signal events.*

Figures 5.15 and 5.16 show the jets multiplicity for uncalibrated jets (as reconstructed by ATLFAST) in full rapidity range $|\eta| < 5$ and with $p_T^{jet} > 10\ GeV$ for SUSY background events and for signal events. Clearly jet multiplicity is much larger for SUSY events ($< N^{jet} >= 4.05$) than for signal ($< N^{jet} >= 1.31$). Also the jets are much harder for SUSY events ($< p_T^{jet} >= 342.2\ GeV$) than for signal ($< p_T^{jet} >= 59.8\ GeV$).

A variable sensitive to inclusive gluino and squarks decays is the effective mass M_{eff}, defined as the scalar sum of the p_T's of the four hardest jets and the missing transverse energy E_T^{miss}:

$$M_{eff} = p_T^1 + p_T^2 + p_T^3 + p_T^4 + E_T^{miss}. \tag{5.2}$$

where the jet p_T's have been ordered such that p_T^1 is the transverse momentum of the leading jet.

Therefore the inclusive variable M_{eff} is very useful to distinguish SUSY from SM events [9], [17]. Typically the effective mass distribution is dominated by Standard Model processes at low M_{eff}, in fact the SM backgrounds tend to have smaller E_T^{miss}, fewer jets and a lower jet multiplicity. While the effective mass distribution is dominated by SUSY processes, of a factor of 5-10 larger than SM prediction, for large M_{eff} values. Figures 5.17 - 5.19 show the

effective mass distribution for SUSY background events, 2 partons to 2 spartons processes, 2 partons to 2 gauginos processes and 2 partons to 2 sleptons processes respectively; only squark and gluino productions contribute for large M_{eff} values.

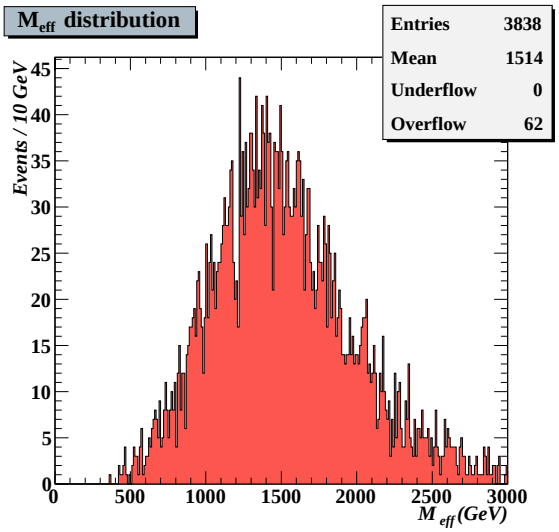

Figure 5.17: *2 partons to 2 spartons processes; squark and gluino production dominates the effective mass distribution at large M_{eff} values.*

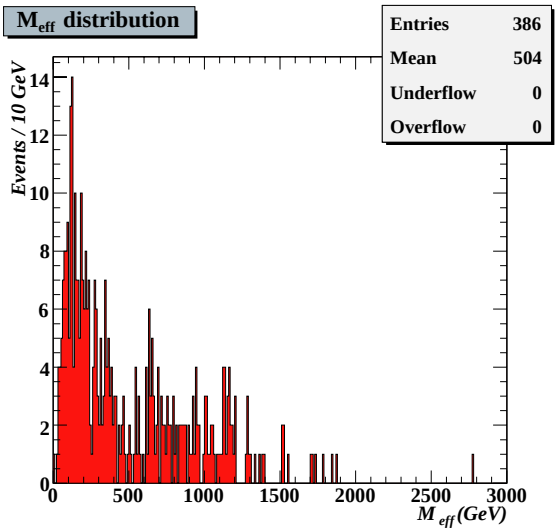

Figure 5.18: *2 partons to 2 gauginos processes; gaugino production dominates the effective mass distribution at low M_{eff} values.*

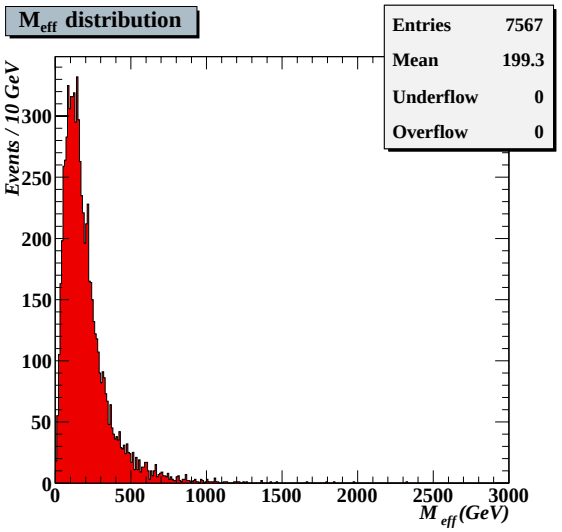

Figure 5.19: *2 partons to 2 sleptons processes; slepton production dominates the effective mass distribution at low M_{eff} values.*

Therefore M_{eff} inclusive variable was very useful to cut the squark and gluino SUSY

background events, requiring events with $M_{eff} < 200GeV$. The M_{eff} distributions for signal events, SUSY background and SM backgrounds are shown in figures 5.20 - 5.24.

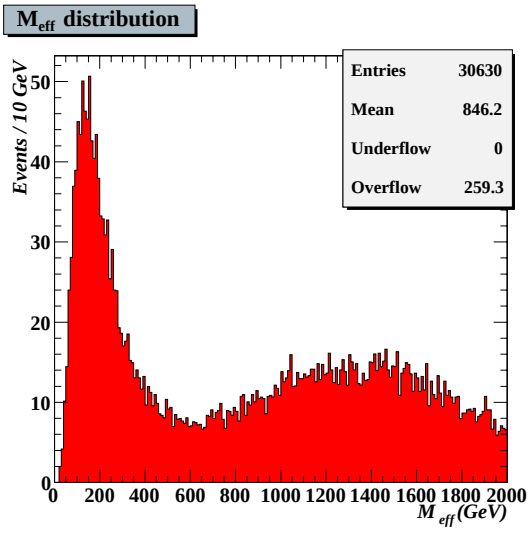

Figure 5.20: *The effective mass distribution for SUSY background events.*

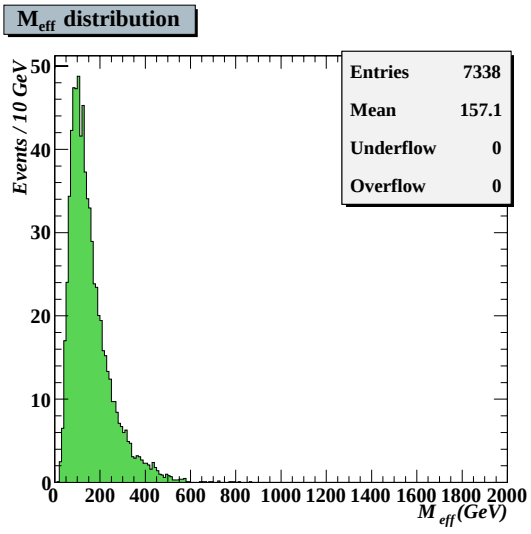

Figure 5.21: *The effective mass distribution for signal events.*

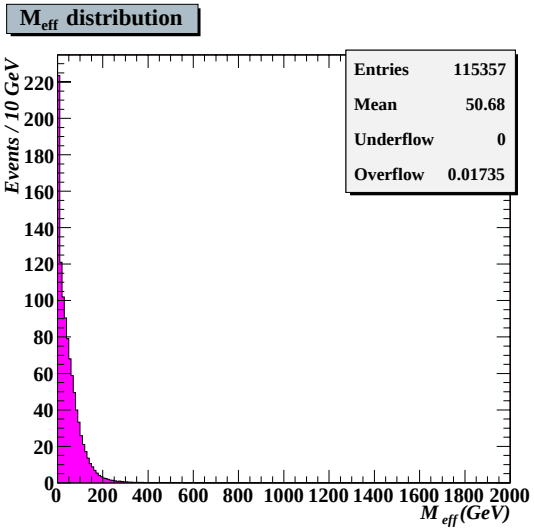

Figure 5.22: *The effective mass distribution for SM ZZ background events.*

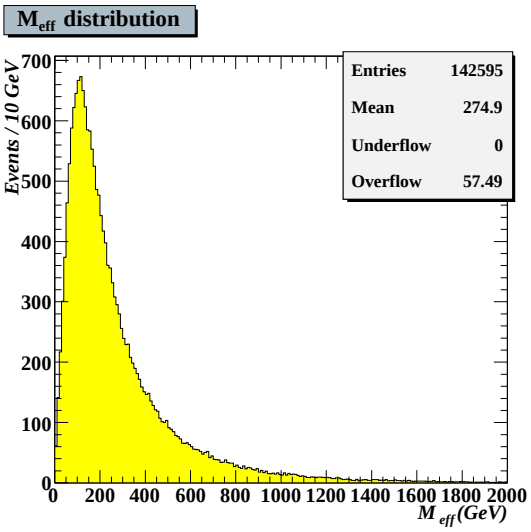

Figure 5.23: *The effective mass distribution for SM $Zb\bar{b}$ background events.*

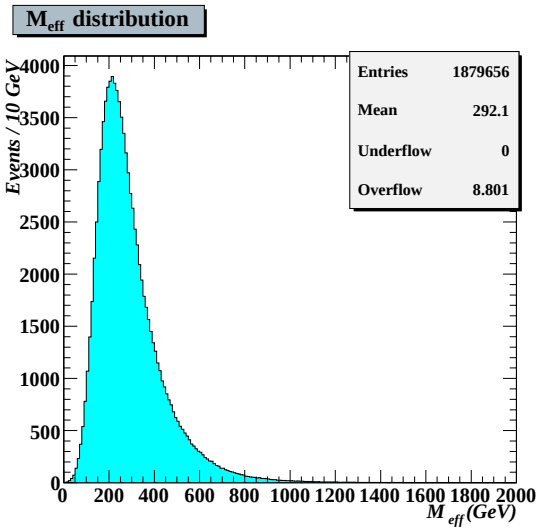

Figure 5.24: *The effective mass distribution for SM $t\bar{t}$ background events.*

5.4.3 SM Background

The most important SM background is the irreducible ZZ, $Z(Z^*/\gamma^*)$, $(Z^*/\gamma^*)(Z^*/\gamma^*)$ production leading to the four-leptons final state, with a $\sigma \times BR$ of 158.8 fb^{-1} (PYTHIA generator, τ-decay excluded). This background was almost completely reduced by the kinematical cut on the dilepton invariant mass edge and by the p_T^{miss} cut.

The SM backgrounds $Zb\bar{b}$ and $t\bar{t}$ are defined as 'reducible backgrounds' because in $Zb\bar{b}$ and $t\bar{t}$ processes the final state leptons tend to be not isolated, due to the presence of b-decay products in the neighbouring of the leptons.

The cross section of the $Zb\bar{b}$ production with the Z boson decaying in electron or muon pair is of 57.5 pb^{-1} (PYTHIA generator, τ-decay excluded). This process may contribute to the four-leptons events if the leptons from the b decay are identified as isolated ones. Again this background was almost completely reduced by the kinematical cut on the dilepton invariant mass edge, because the Z mass is higher than the dilepton kinematical edge (m_{ll}^{max}), and by the cut on p_T^{miss}.

The cross section of the $t\bar{t}$ production with both:

$$t \to W^+ b$$
$$\bar{t} \to W^- b$$

and with the W boson forced to decay in:

$$W^\pm \to l^\pm \nu \quad (l = e, \mu)$$

is of 22.94 pb^{-1} (PYTHIA generator, τ-decay excluded). This process may contribute to the four-leptons events if the leptons from the b decay are identified as isolated ones. The expected background from $t\bar{t}$ events is of $\sim 14.7{\cdot}10^6$ events with SF-OS lepton pairs for an integrated luminosity of 30 fb^{-1} if no isolation requirements are applied on the leptons. This number of events was reduced to $\sim$ 16000 events by the kinematical cuts on the dilepton mass, the p_T^{miss} and M_{eff}.

To reduce $t\bar{t}$ background it was decided to use the isolation criteria, and the results of the full simulation reported in [18] for $H \rightarrow ZZ^* \rightarrow 4l$ was taken into account. In the isolation criteria, tracker isolation, of this study a lepton was considered as isolated when there was no charged track above a given p_T-threshold p_T^{max} in a cone of radius $R = \sqrt{\delta\eta^2 + \delta\phi^2} = 0.2$ around its own track. Four isolated leptons are required. Other criteria, as the sum of the momentum in the cone or the total number of charged tracks in the neighbouring of the lepton have been investigated for the cited study, without any improvement with respect to the first one.

The rejection again $t\bar{t}$ and $Zb\bar{b}$, keeping the isolation efficiency on 90% level, achieved were $\mathcal{R} = 110 \pm 22$ and $\mathcal{R} = 30 \pm 10$ respectively. As shown in [18] a total rejection of 1200 $\pm$ 300 at low luminosity and 810 $\pm$ 200 at high luminosity is achievable for the signal efficiencies of 81% for muons and 58% for electrons for low luminosity performance and for the signal efficiencies of 57% for muons and 47% for electrons for high luminosity performance using a combination of isolation and impact parameter criteria.

The rejection of $\mathcal{R} = 110$ only against $t\bar{t}$ events would decrease this background to 145 expected events for an integrated luminosity of 30 fb^{-1}.

5.4.4 Expected Signal and Backgrounds Events after Kinematical Cuts

The expected number of four-leptons events for signal and background after applying the kinematical cuts described in thew previous paragraphs are reported in table 5.7, normalized to an integrated luminosity of 30 fb^{-1}.

	Higgs $\rightarrow \chi_2^0\chi_2^0 \rightarrow 4lep.\chi_1^0\chi_1^0$	SUSY bkg.	SM bkg: ZZ	SM bkg: $Zb\bar{b}$	SM bkg: $t\bar{t}$
Generated Events	1315	249000	4785	1469000	$14.742 \cdot 10^6$
`MultiLeptonFilter`	1042.4	3340.8	1003.6	16113.2	$2.132 \cdot 10^6$
p_T selection	369.5	607.6	535.7	1107.2	106607.3
$m_{ll} < 55GeV$	369.3	419.5	21.4	159.6	31678.3
$M_{eff} < 200GeV$	354.8	122.8	21.4	83.1	17419.4
$p_T^{miss} > 20GeV$	319.4	115.5	1.2	30.6	15946.3

Table 5.7: *Number of surviving signal and background events after successive selection cuts for an integrated luminosity of 30 fb^{-1}. In the last line the numbers of surviving $Zb\bar{b}$ and $t\bar{t}$ events after the application of the isolation criteria from [18] are reported.*

As reported in the last column of the table 5.7 the number of $t\bar{t}$ events that have passed the kinematical cut is high, because the leptons from b-decay are identified as isolated ones by ATLFAST. To reduce this background it was applied the rejection from [18] as discussed before. In this way the number of $t\bar{t}$ events are reduced to 145 events and the $Zb\bar{b}$ events to 1 event for an integrated luminosity of 30 fb^{-1}.

5.5 Dependence of the discovery on the m_A parameter

As a next step it was investigated the observability of the channel $A/H \to \chi_2^0\chi_2^0 \to 4l + E_T^{miss}$ varying the m_A free parameter from 300 GeV to 450 GeV. The expected number of signal events are reported in tables 5.8 and 5.9, normalized at 30 fb^{-1}.

30 fb^{-1} NORMALIZED	$m_{A^0} = 300$ GeV		$m_{A^0} = 350$ GeV	
	A^0	H^0	A^0	H^0
Generated Events	1072.26	119.37	956.07	352.22
After `MultiLeptonFilter`	847.08	93.75	756.44	277.36
After Analysis Cuts	245.4	26.57	233.15	83.64
$A + H$ events	271.97		316.79	

Table 5.8: *Number of surviving signal events after successive selection cuts (30 fb^{-1}) for different values of the m_A free parameter, $m_A = 300$ GeV and $m_A = 350$ GeV.*

30 fb^{-1} NORMALIZED	$m_{A^0} = 400$ GeV		$m_{A^0} = 450$ GeV	
	A^0	H^0	A^0	H^0
Generated Events	412.65	274.3	250.42	180.56
After `MultiLeptonFilter`	332.57	218.74	201.46	146.23
After Analysis Cuts	110.73	74.13	62.47	53.5
$A + H$ events	184.86		115.97	

Table 5.9: *Number of surviving signal events after successive selection cuts (30 fb^{-1}) for different values of the m_A free parameter, $m_A = 400$ GeV and $m_A = 450$ GeV.*

As a criterion for discovery it was required the significance $\sigma \geq 5$, with σ defined as $\sigma = \frac{S}{\sqrt{B}}$, where S and B are the number of signal and background events respectively.

	m_{A^0} (300 GeV)	m_{A^0} (350 GeV)	m_{A^0} (400 GeV)	m_{A^0} (450 GeV)
$\sigma = \frac{S}{\sqrt{B}}$	16.8	19.5	11.4	7.2

Table 5.10: *Significance, $\sigma = \frac{S}{\sqrt{B}}$, for the different values of m_A investigated.*

In table 5.10 the significance for the different values of m_A investigated are summarized.

5.6 Higgs Mass Reconstruction

The main assumption of this study is the previous discovery of supersymmetry and therefore this analysis strategy is performed assuming the masses of the two lighter neutralinos ($\tilde{\chi}_2^0$, $\tilde{\chi}_1^0$) and of the right handed slepton as known, and the corresponding errors were ignored.

After the events selection, to reconstruct the Higgs mass, the mass shell conditions of the particles involved in the decay chain were used:

$$m^2_{\tilde{\chi}_1^0} = p^2_{\tilde{\chi}_1^0}, \tag{5.3}$$

$$m^2_{\tilde{l}_R} = (p_{\tilde{\chi}_1^0} + p_{l_1})^2, \tag{5.4}$$

$$m^2_{\tilde{\chi}_2^0} = (p_{\tilde{\chi}_1^0} + p_{l_1} + p_{l_2})^2. \tag{5.5}$$

where the lepton indicated by l_2 is the one from the $\tilde{\chi}_2^0$ decay:

$$\tilde{\chi}_2^0 \rightarrow \tilde{l}_R l_2,$$

and the lepton indicated by l_1 is the one from the decay of the slepton:

$$\tilde{l}_R \rightarrow \tilde{\chi}_1^0 l_1.$$

Then the Higgs mass was reconstructed as the invariant mass of the two next-to-lightest neutralinos.

Figures 5.25 and 5.26 show the Higgs invariant mass for $e^+e^-\mu^+\mu^-$ and $l^+l^-l^+l^-$ events respectively, for an integrated luminosity of 300 fb^{-1}.

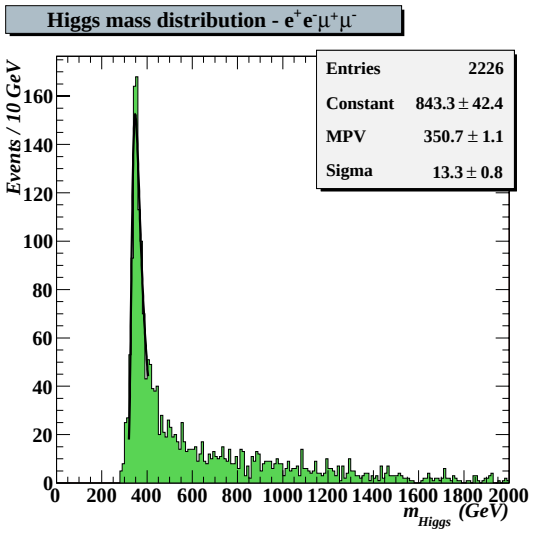

Figure 5.25: *The Higgs mass distribution for $e^+e^-\mu^+\mu^-$ events at 300 fb^{-1}.*

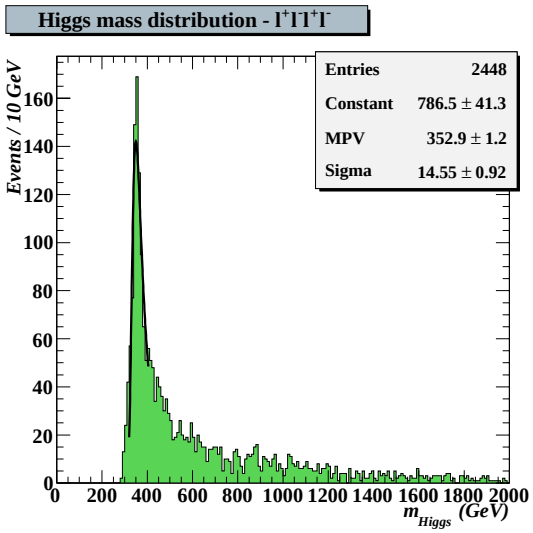

Figure 5.26: *The Higgs mass distribution for $l^+l^-l^+l^-$ events at 300 fb^{-1}.*

To increase statistic it was decided to take into account the $e^+e^-e^+e^-$ and $\mu^+\mu^-\mu^+\mu^-$ sample events; in fact the combinatorial background from the wrong choice of lepton pairs estimated from the $e^+e^-\mu^+\mu^-$-events contributes very few to the Higgs mass spectrum (Figure 5.27).

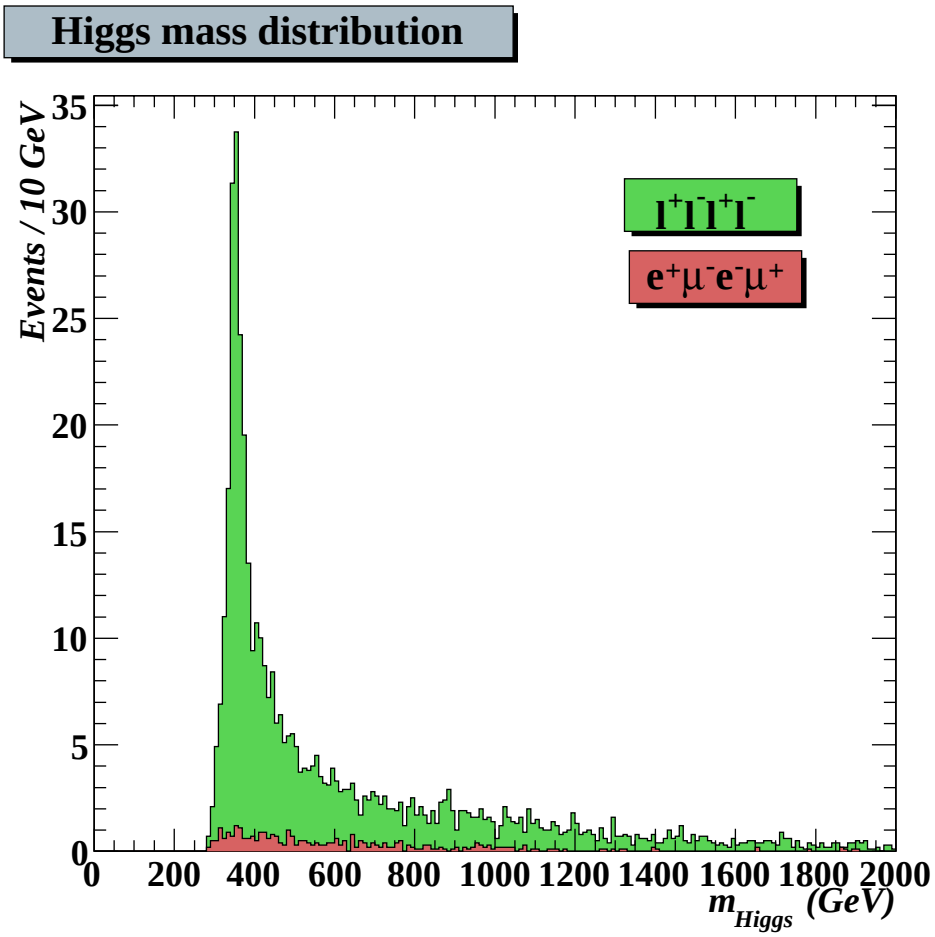

Figure 5.27: *The Higgs mass distribution for $e^+\mu^-\mu^+e^-$ and $l^+l^-l^+l^-$ events at 30 fb^{-1}.*

In figure 5.28 the Higgs invariant mass is shown as the distribution of $e^+e^-\mu^+\mu^-$ and $l^+l^-l^+l^-$ events signal events and for an integrated luminosity of 300 fb^{-1}. The peak was fitted with a landau function and the most probable value is (351.8 $\pm$ 0.8) GeV, a value compatible with the generated mass value (see Table 5.2).

Figure 5.29 shows the Higgs invariant mass distribution for signal events and the distribution of all the background samples superimposed to it, all normalized to 30 fb^{-1}.

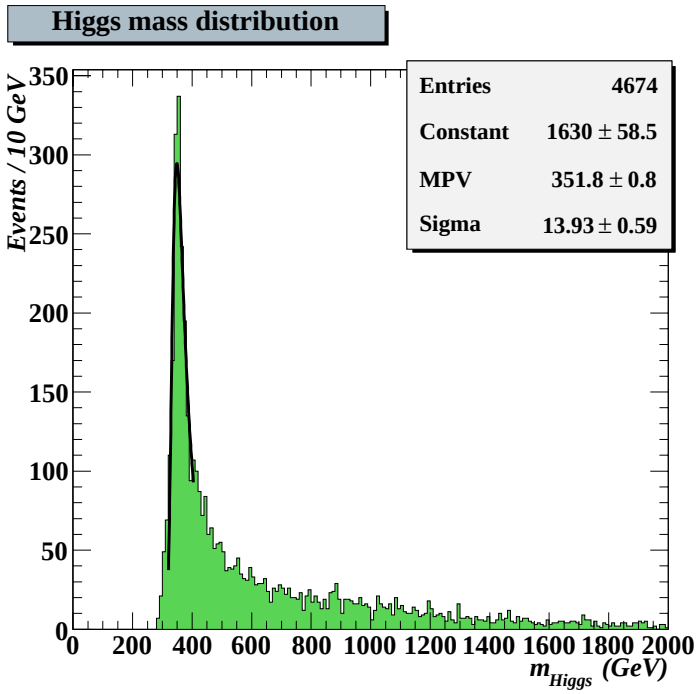

Figure 5.28: *The Higgs mass distribution for $e^+e^-\mu^+\mu^-$ and $l^+l^-l^+l^-$ events at 300 fb^{-1}.*

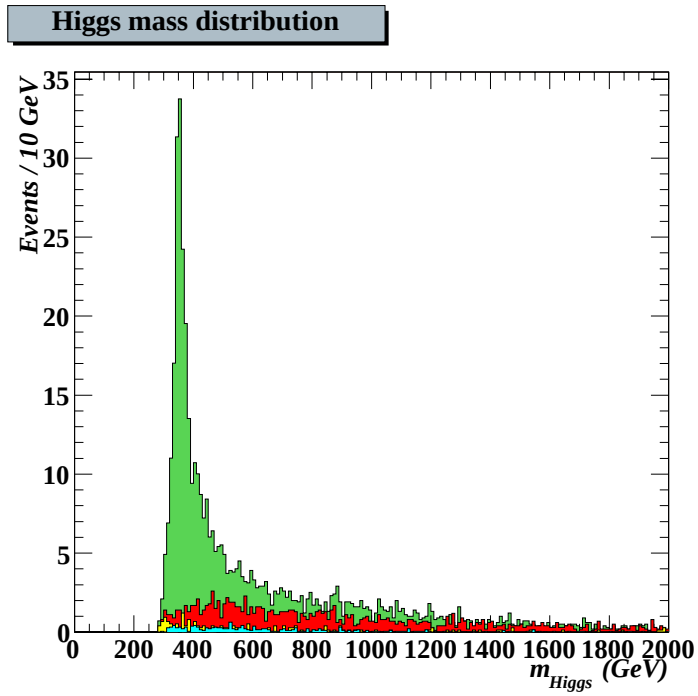

Figure 5.29: *The Higgs mass distribution of all the samples (signal and backgrounds) superimposed and normalized to 30 fb^{-1}.*

5.7 Summary and Conclusions

In this chapter the sparticle decay mode of the heavy neutral SUSY Higgs bosons has been investigated.

A fast analysis of the channel $A/H \to \tilde{\chi}_2^0\tilde{\chi}_2^0 \to 4l^{\pm} + X$ $(l = e, \mu)$ was performed. The SM ZZ, Zbb and tt processes were taken into account as backgrounds, because leading to a four-leptons final state signature like the Higgs decay under study. The main background was SUSY itself, which was investigated too.

The signal and SUSY background were generated using the HERWIG generator program, while the SM backgrounds were generated using the PYTHIA generator program. The ATLFAST fast Monte Carlo was used to simulate the detector response.

The analysis framework was the Minimal Supersymmetric Extension of the Standard Model (MSSM) with 12 free parameters, instead of 18, assuming that all the squark masses are equal and the masses of all the slepton generation are also equal.

For the chosen point of the MSSM parameter space, a clear signal can be observed selecting events with four isolated leptons in the final state.

The applied selection criteria sufficiently suppress ZZ, Zbb and SUSY backgrounds while the isolation criteria strongly suppress tt (and further Zbb) background, leading to good significance values.

Also a scan in m_{A^0} free parameter was done and the relative values of significance, reported in table 5.10, are shown in figure 5.30.

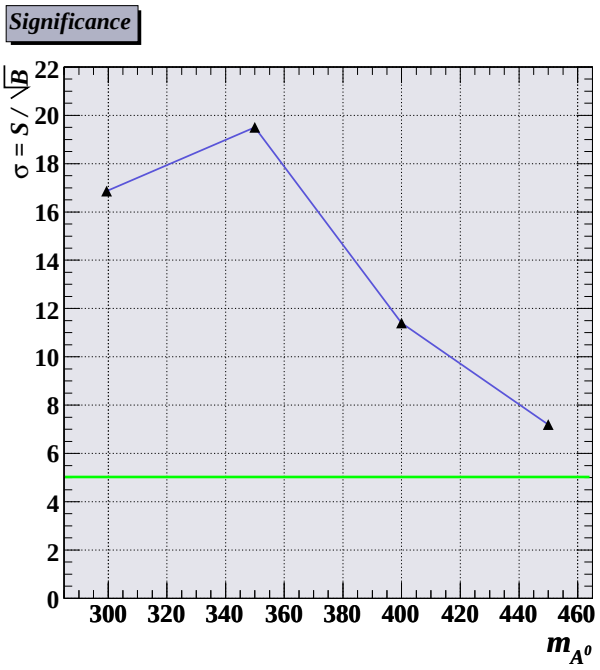

Figure 5.30: *The expected sensitivity to detect neutral SUSY Higgs bosons decaying into two next-to-lightest neutralinos for an integrated luminosity of 30 fb^{-1}.*

Bibliography

[1] *F. E. Paige*, ***Supersymmetry Signatures at CERN LHC***, BNL-HET-98/1, 1998.

[2] *ATLAS Collaboration*, ***ATLAS Detector and Physics Performance Technical Design Report***, CERN/LHCC 99-15, 1994.

[3] *J. Thomas*, ***Study of Heavy MSSM-Higgs Bosons A/H in hadronic τ-decays in ATLAS***, CERN/ATL-PHYS-2003-003, 2003.

[4] *D. Cavalli and G. Negri*, ***Extension of the Study of $A/H \to \tau\tau \to lepton - hadron$ in the high m_A region***, CERN/ATL-PHYS-2003-009, 2003.

[5] *H. Baer et al.*, ***Detecting Higgs Boson Decays to Neutralinos at Hadron Supercolliders***, Phys. Rev. D50, 316, 1994.

[6] *S. Zmushko et al.*, ***Search for the Heavy Higgs in SUGRA Point 3***, CERN/ATL-COM-PHYS-98-009, 1998.

[7] *S. Zmushko et al.*, ***The $A/H \to \tilde{\chi}\tilde{\chi} \to 4lX$ observability with ATLAS (Predictions within SUGRA Model)***, CERN/ATL-COM-PHYS-99-005, 1999.

[8] *D. N. Spergel et al.*, ***First Year Wilkinson Microwave Anisotropy Probe (WMAP) Observations: Determination of Cosmological Parameters***, astro-ph/0302209, 2003.

[9] *I. Hinchliffe, F. E. Paige, G. Polesello, E. Richter-Was*, ***Precision SUSY Measurements with ATLAS: Introduction and Inclusive Measurements***, CERN/ATL-PHYS-97-107, 1997.

[10] *G. Corcella et al.*, ***HERWIG 6: an Event Generator for Hadron Emission Reactions With Interfacing Gluons (Including Supersymmetric Processes)***, hep-ph/0011363, Journal of High Energy Physics 01, 010, 2001.

[11] *S. Moretti et al.*, ***Implementation of Supersymmetric Process in the HERWIG Event Generator***, hep-ph/0204123, 2002.

[12] *H. Baer et al.*, ***ISAJET 7.48: A Monte-Carlo Event Generator for pp, $p\bar{p}$ and e^+e^- reactions***, hep-ph/0001086, 2000.

[13] See: http://www.hep.phy.cam.ac.uk/ richardn/HERWIG/ISAWIG/.

[14] *T. Sjöstrand et al.*, ***PYTHIA 6.3 - Physics and Manual***, hep-ph/0308153, 2003.

[15] *E. Richter-Was et al.*, ***ATLFAST 2.0 - A Fast Simulation Package for ATLAS***, CERN/ATL-PHYS-98-131, 1998, and see also: http://www.hep.ucl.ac.uk/atlas/atlfast/.

[16] *W. Lavrijsen*, ***The Athena Startup Kit - A Gentle Dive into Atlas Offline Software***, http://wlav.home.cern.ch/wlav/athena/athask/, 2005.

[17] *I. Hinchliffe, F. E. Paige et al.*, ***Precision SUSY Measuments at CERN LHC***, Phys. Rev. D 55, 5520-5540, 1997.

[18] *O. Linossier and L. Poggioli*, $H^0 \rightarrow ZZ^* \rightarrow 4l$ ***Channel, in ATLAS - Signal Reconstruction and Reducible Backgrounds Rejection***, CERN/ATL-PHYS-97-101, 1997.

List of Figures

List of Tables

Aknoledgements

I am grateful to many people for their help and support during the doctoral period.

First of all I would like to thank my Professor Giancarlo Susinno, who gave me the opportunity to start working in the ATLAS Muon collaboration. Also many thanks to all the INFN Cosenza group.

A big thank to all my collegues involved in the X5/GIF ageing test, Manuela Cirilli, Alessandro Di Girolamo, Antonio Di Domenico, Sandro Palestini, Marco Schioppa, Paolo Valente and Stephanie Zimmermann, they all are very great physicists and persons! I would also like to thank William Andreazza for his invaluable help in the preparation and handling of the experimental setup and for designing the chamber support. And I gratefully acknowledge the technical support brought by Elio Buccheri and Silvano Di Marco from INFN Roma and Vittorio Romano from Calabria University.

Finally I would like to thank Giacomo Polesello for guiding me through the difficul way of the Supersymmetry in searching the Higgs bosons!